TABLE OF CONTENTS

Page

LIST OF TABLES

Page

LIST OF FIGURES

XVIII

LIST OF ABBREVIATIONS

Blisks	Blade Integrated Disks
CNC	Computer Numerical Control
DDB	Deformable / Deformable Bodies
DOF	Degree of Freedom
DRB	Deformable / Rigid Bodies
DRX	Dynamic Recrystallization
FEM	Finite Element Modeling
HAZ	Heat Affected Zone
HTA	Heat Transfer Analysis
JMAK	Johnson, Mehl, Avrami, Kolmogorov
LFW	Linear Friction Welding
LVDT	Linear Variable Differential Transformer
OM	Oscillation Model
PAZ	Plastically Affected Zone
Phases II-III	Friction Phase
Phase I	Initial Phase
Phase II	Transition Phase
Phase III	Equilibrium Phase
Phase IV	Post-Processing phase

SB	Single Body
SEM	Scanning Electron Microscopy
SFW	Stir Friction Welding
TM	Thermal Model
TMA	Thermo-Mechanical Analysis
TMAZ	Thermo-Mechanical Affected Zone
WCZ	Weld Center Zone

LIST OF SYMBOLS AND UNITS OF MEASUREMENTS

α, κ	Thermal diffusivity [m^2·s^{-1}]
δ	Sticking State Variable [1]
η	Mechanical Efficiency [1]
λ	Thermal conductivity [W·m^{-1}·K^{-1}]
μ	Friction coefficient [1]
ρ	Density [kg·m^{-3}]
σ_y	Yield Stress [MPa]
τ	Shear Stress [MPa]
φ	Heat distribution factor [1]
a	Oscillation amplitude [mm]
cp	Specific heat capacity [J·kg^{-1}·K^{-1}]
E_x	Total energy inputted to the weld [W·s]
f	Oscillation frequency [Hz]
F_{int}	Interface force [N]
HI	Heat input [W·m^{-2}]
q	Heat flow [W·m^{-2}]
Q_{total}	Total heat power input [W]
s	Axial shortening [mm]
s_{III}	Axial shortening during Phase III [mm]

s_{II}	Axial shortening during Phase II [mm]
s_{max}	Axial shortening at the end of Phase III [mm]
T	Temperature [°C]
t	Time [s]
t_{max}	Process duration [s]
v	Axial shortening rate during Phase III [mm·s^{-1}]
w_{PAZ}	Width of the Plastically Affected Zone (PAZ) [mm]
x_{HAZ}	Heat Affected Zone (HAZ) limit [mm]

INTRODUCTION

In a context of digitalization, industries are investing in process numerical twins. This allows the industries to model the complete manufacturing cycle of a product before it is born, reducing the operational cost and the time to market. As an example, the aeronautical industry has numerical aircraft which are used in the certification process. To do so, assembly processes such as the Linear Friction Welding (LFW) have to be modeled in order to be integrated in the final numerical product.

The LFW process is a high-added-value process used for high quality assembly manufactured in the aeronautical industry. It is a complex thermo-mechanical solid state joining process with significant microstructural transformation, costly to study by experiments. Therefore, numerical modeling of this process allows identifying optimal parameters for experimental validation. This study aims to provide an efficient numerical model to simulate the LFW process with specific output such as the microstructural changes. In addition, Ti-6Al-4V alloy is used as a case study in this research.

The first chapter of this thesis is a literature review of the LFW process. It begins with a thermo-mechanical analysis of the process, establishing the relationship between the heat generation and the process parameters. The challenges faced for modeling the friction in LFW is illustrated with various approaches. Then, the fundamental equations and the boundary conditions are examined. Experimental and numerical publications have been studied to extract the main characteristics of the LFW process, particularly, the influence of each characteristic and their relationships. Finally, based on the literature review, the process is discretized into different phases for numerical implementation and analysis. On the basis of the gaps identified in the literature review, the following research objectives were identified: phase transition definition, numerical model efficiency, and microstructure evolution simulation.

The second chapter details the hypothesis and methodology used to establish the chained

numerical model. The Ti-6Al-4V mechanical and microstructural properties are examined and properties of interest for the LFW are identified. The process phases separation and identification is an important topic of this study. Thermo-mechanical and mathematical analyses are made on the transition between one phase to the next to identify and separate each phase for numerical implementation. Then, the details of chained numerical modeling is described. Three numerical models are proposed: Two models to simulate the first phase of the LFW process with two different approaches to identify the most efficient model. Then, the third model simulates the last two phases of the process. A subroutine was implemented in the first model to account for the heat generated by the oscillations as the workpieces are modeled stationary. Another subroutine was developed for the second model to implement the microstructure evolution model based on the JMAK equation.

The third chapter applies the chained numerical on a Ti-6Al-4V alloy. First, end phase criteria made to identify and separate each phase were tested and analyzed. The axial shortening rate impact on the material extrusion was studied. The temperature history predicted by Oscillation Model (OM) and Thermal Model (TM) were compared with published thermocouple measurements to report their accuracy. A comparison between the OM and TM using the temperature field was made to support their equivalence. Also, an efficiency analysis was made between the two models to point out the gain in efficiency. The temperature history and distribution are also reviewed. A flash morphology analysis is made to examine the impact of the process parameters on the material extrusion. Finally, the predicted microstructure evolution is described and compared with experimental results.

CHAPTER 1

LITERATURE REVIEW

1.1 The Linear Friction Welding Process

The LFW is a solid-state joining process for complex component assemblies such as Blade Integrated Disks (Blisks) (Figure 1.1) in gas turbines or aircraft engines. The two workpieces are brought together and jointed thanks to their reciprocal motion and compression pressure applied on the sample to ensure the contact between the workpieces. It is a solid state joining technique in contrast to the conventional welding where the two faces to-be-welded are melted.

The aeronautic industry is using this technology for the manufacturing and the repair of the Blisks. Bladed disks are assembled with mechanical junctions such as dovetail which are prone to erosion, cracking and fatigue. Blisks limit these issues as the blades and the disks make only one piece. They can be made by casting or Computer Numerical Control (CNC) milling which is highly expensive and complex to manufacture. However, those production methods may not allow the repair of damaged pieces. LFW can be used to joint the blade to the disk, avoiding complex casting and precision machining to create the mechanical junction. It also provides the ability to repair the damage blades during a maintenance check up by removing the faulty ones and linearly friction weld new ones.

The main characteristic of the LFW joining process is that it never reaches the melting point of the material. It reduces the interactions with atmospheric gas, making an excellent method to weld titanium alloys. These latter are highly reactive with the atmospheric oxygen at high temperature which requires the use of shielding gas like argon to prevent oxidation during the weld. The oscillating motion removes the oxide layers present at the welding surface and the pressure applied to the workpiece bring new metallic atoms together and creates the bond. So, no filler material is required in LFW compared to a TIG or MIG techniques.

LFW reduces the manufacturing cost as it does not require any consumable and, furthermore, it

reduces the component weight as less material is needed to join the blade to the disk compared to a mechanical assembly. As it is a high-added-value process, it is used on costly and critical assemblies (ex: aircraft turbines) that numerical simulations allow designers to test various process configurations and optimize the assembly before its production.

Figure 1.1   LFW blisks assembly made by The Welding Institute
(TWI (2018))

1.1.1   Thermo-Mechanical Analysis

The process is composed of two workpieces and dies holding the workpieces in position. This study has chosen a vertical mounting (Figure 1.2) as a case study as it is commonly reported in the literature: Vairis & Frost (2000); Wanjara & Jahazi (2005); Dalgaard (2011); Yang *et al.* (2015); McAndrew *et al.* (2017). Usually, the lower workpiece oscillates (Equation 1.1) with (a) the oscillation amplitude and (f) the frequency.

$$u(t) = a\sin\left(2\pi ft\right) \tag{1.1}$$

A contact force (F) is applied on top of the upper workpiece to insure the contact and generate friction between the two workpieces. The amplitude (a), the frequency (f), and the contact force (F_c) or its equivalent pressure (p_c) are the process parameters of the LFW.
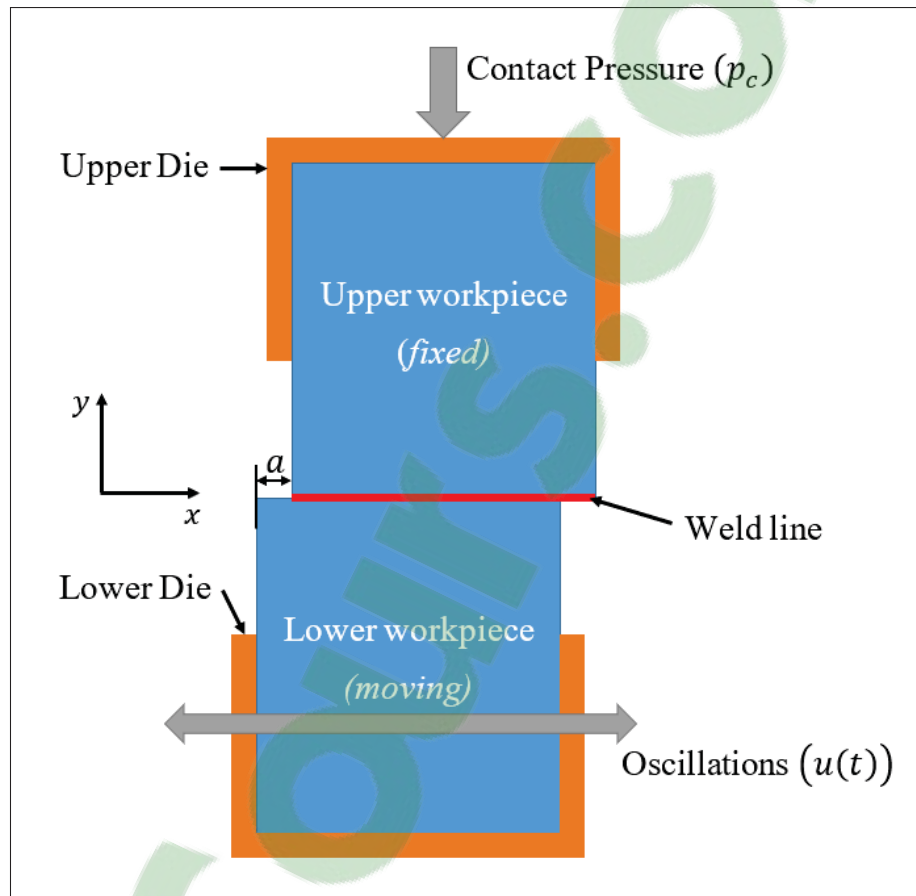
Figure 1.2   Vertical mounting setup of the linear friction welding

While the workpieces are rubbing against each other, the thermal energy (E_x) is released into the weld line as: (Vairis & Frost (2000); McAndrew *et al.* (2014))

$$E_x = \vartheta \int_0^t F_{int} \dot{u}(t) dt \tag{1.2}$$

with (ϑ) the heat conversion ratio, (F_{int}) the interface force of the workpieces, and $(\dot{u}(t))$ the instantaneous displacement velocity.

Usually (ϑ) is between 0.9 and 1 and most commonly considered equal to 1 (Li *et al.* (2014); Yang *et al.* (2015); Buffa & Fratini (2017)). So, under these assumptions, the total thermal power (Q_{total}) at the weld line is equal to:

$$Q_{total} = F_{int}\dot{u}(t) \tag{1.3}$$

A penalty method is used (Vairis & Frost (2000); Vairis & Christakis (2007); Bikmeyev *et al.* (2013); Jedrasiak *et al.* (2018); Grujicic *et al.* (2012); McAndrew *et al.* (2014); Schröder *et al.* (2015)) to describe the relationship between the interface force (F_{int}) and the normal force (F_n) at the weld line with a friction coefficient (μ). Such coefficient may depend on the temperature, the contact pressure at the weld line, and the surface roughness (Figure 1.3).

$$F_{int} = \mu F_n \tag{1.4}$$

So, according to Equations 1.1, 1.3, and 1.4, the total thermal power input is :

$$Q_{total} = 2\pi\mu F_n af|\cos(2\pi ft)| \tag{1.5}$$

It highlights the direct correlation between the input parameters - amplitude (a) and frequency (f) - and the total thermal power released at the weld line. However, it is shared between the upper and lower welding surfaces: $Q_{total} = Q_{upper} + Q_{lower}$. A heat distribution factor (φ) defines the power input that each surface receives, depending on their material thermal properties (Sorina-Müller *et al.* (2010)):

$$\varphi = \frac{Q_{upper}}{Q_{lower}} = \sqrt{\frac{\lambda_{upper}\rho_{upper}cp_{upper}}{\lambda_{lower}\rho_{lower}cp_{lower}}} \tag{1.6}$$

with (λ) the thermal conductivity, (ρ) the material density, and (cp) the specific heat capacity of

the upper and lower workpieces respectively. Thus, the thermal power input that each surface receives is equal to:

$$
\begin{cases}
Q_{upper} = \frac{\varphi}{1+\varphi} Q_{total} \\
Q_{lower} = \frac{1}{1+\varphi} Q_{total}
\end{cases}
\tag{1.7}
$$

One can notice that for similar material on both workpieces, the heat distribution factor (φ) is equal to 1 . Therefore, the heat power received by both surfaces is noted (Q) and is equal to :
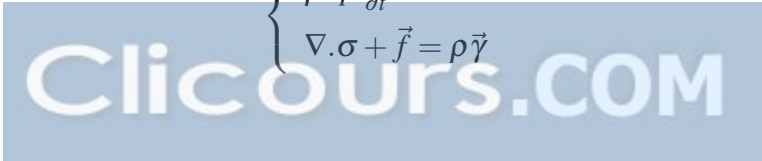
$$
Q = \pi\mu F_n a f |\cos(2\pi f t)|
\tag{1.8}
$$

From the above equation, the average thermal power input over one oscillation can be defined and characterizes welds under a unique parameter as follows (Vairis & Frost (2000); Schroeder *et al.* (2012); McAndrew *et al.* (2014)):

$$
\bar{Q}_{total} = \frac{4}{T} \int_0^{\frac{T}{4}} Q_{total} \, dt = 4\mu F_n a f = \mu F_n v_r
\tag{1.9}
$$

with ($v_r = 4af$) the rubbing velocity as defined by McAndrew *et al.* (2014). It separates and highlights the contribution of the friction (μF_n), on the one hand, and the oscillations ($4af$), on the other hand. This distinction is used in optimization studies, both experimental and numerical, to provide smaller design of experiments by aggregating parameters according to their influence on the process.

The thermo-mechanical system to solve is :

$$
\begin{cases}
\rho c p \frac{\partial T}{\partial t} - \lambda \Delta T = S \\
\nabla.\sigma + \vec{f} = \rho \vec{\gamma}
\end{cases}
\tag{1.10}
$$

with (T) the temperature, (S) the heat production per unit volume, (σ) the stress tensor, ($\vec{f}$) the force per unit volume, and (γ) the acceleration per unit volume. It can be noted that there is no heat production per unit volume nor force per unit volume during the LFW process. In addition, the boundary conditions are :

$$
\begin{cases}
(-\lambda \nabla T).\vec{n}_{ws} = \frac{Q}{A} & \text{Heat flux through the welding surface (ws)} \\
(-\lambda \nabla T).\vec{n}_{dies} = q_{dies} & \text{Heat flux lost to the dies} \\
(-\lambda \nabla T).\vec{n}_{air} = q_{air} & \text{Heat flux lost to the environment} \\
T(x,y,z,t=0) = T_{room} & \text{Workpiece temperature at the beginning of the weld} \\
\vec{u}_{lower}(t).\vec{x} = u(t) & \text{Lower workpiece displacement} \\
\vec{u}_{upper}(t).\vec{y} = 0 & \text{Upper workpiece constraint} \\
\vec{n}_{top}.\sigma.\vec{n}_{top} = F_c & \text{Applied force}
\end{cases}
\tag{1.11}
$$

with ($\vec{n}$) normal of the surfaces, ($\vec{u}_{lower}, \vec{u}_{upper}$) workpieces displacement vectors, (q_{dies}, q_{air}) heat flux lost to the dies and lost to the environment, respectively.

The friction plays a fundamental purpose in the LFW and one can argue that a penalty method such as Coulomb's law (Li *et al.* (2014); Vairis & Frost (2000); Bertrand *et al.* (2018); Maio *et al.* (2016); Potet *et al.* (2017)) may not represent accurately the contact interaction during the process. For example, the Coulomb's law is relevant at low temperature whereas the temperature range encountered during the process is from 25 °C to above 1000 °C.

In addition, the nature of the friction changes during the process, starting with a dry friction to stick-slip contact and viscous friction (Vairis & Christakis (2007)). To cope with this issue, some approaches have been published in the literature. On the one hand, various studies have used a penalty method as it is convenient for numerical implementations. Maio *et al.* (2016) modified the Coulomb's friction coefficient at high temperature to account for the change of friction (Figure 1.3a). Vairis & Frost (2000) used an effective friction coefficient from experiments (Figure 1.3b) depending on the rubbing velocity. Schröder *et al.* (2015) based

their approach on the thermal power input and defined an equation based friction coefficient, approaching all cases from low to high thermal power input. All three approaches are using a penalty method, however, divergences are worth noticing:

- Maio *et al.* (2016) considered a friction coefficient independent from the process parameters.

- Vairis & Frost (2000) and Schröder *et al.* (2015) defined their friction coefficient based on process parameters: rubbing velocity and thermal power input, respectively.

- Vairis & Frost (2000) and Maio *et al.* (2016) have similar values at low and mid temperature but diverge at high temperature: Maio *et al.* (2016) friction coefficient decreases to 0 at high temperature whereas the Vairis & Frost (2000) friction coefficient increases to 1 at high temperature.

- Schröder *et al.* (2015) assumes a friction coefficient equal to 0 at $0\,°C$ and increases to 0.5 at high temperature ($1200\,°C$) following a log law : $\mu(T) = 0.15\ln(T) - 0.625$.

On the other hand, few studies (Vairis & Christakis (2007); Maalekian *et al.* (2008); Sorina-Müller *et al.* (2010); Geng *et al.* (2019b)) have applied other interaction methods. Maalekian *et al.* (2008) considered a combined approach with a penalty method at low temperature and a stick-slip model at high temperature (Figure 1.3d, Equation 1.12):

$$Q_{total} = [(1-\delta)\mu F_n v] + (\delta \eta \tau_y, v) \qquad (1.12)$$

where (η) is the mechanical efficiency, i.e. the amount of mechanical energy converted to heat energy, and (δ) is a state variable, which denotes the extent of sticking.
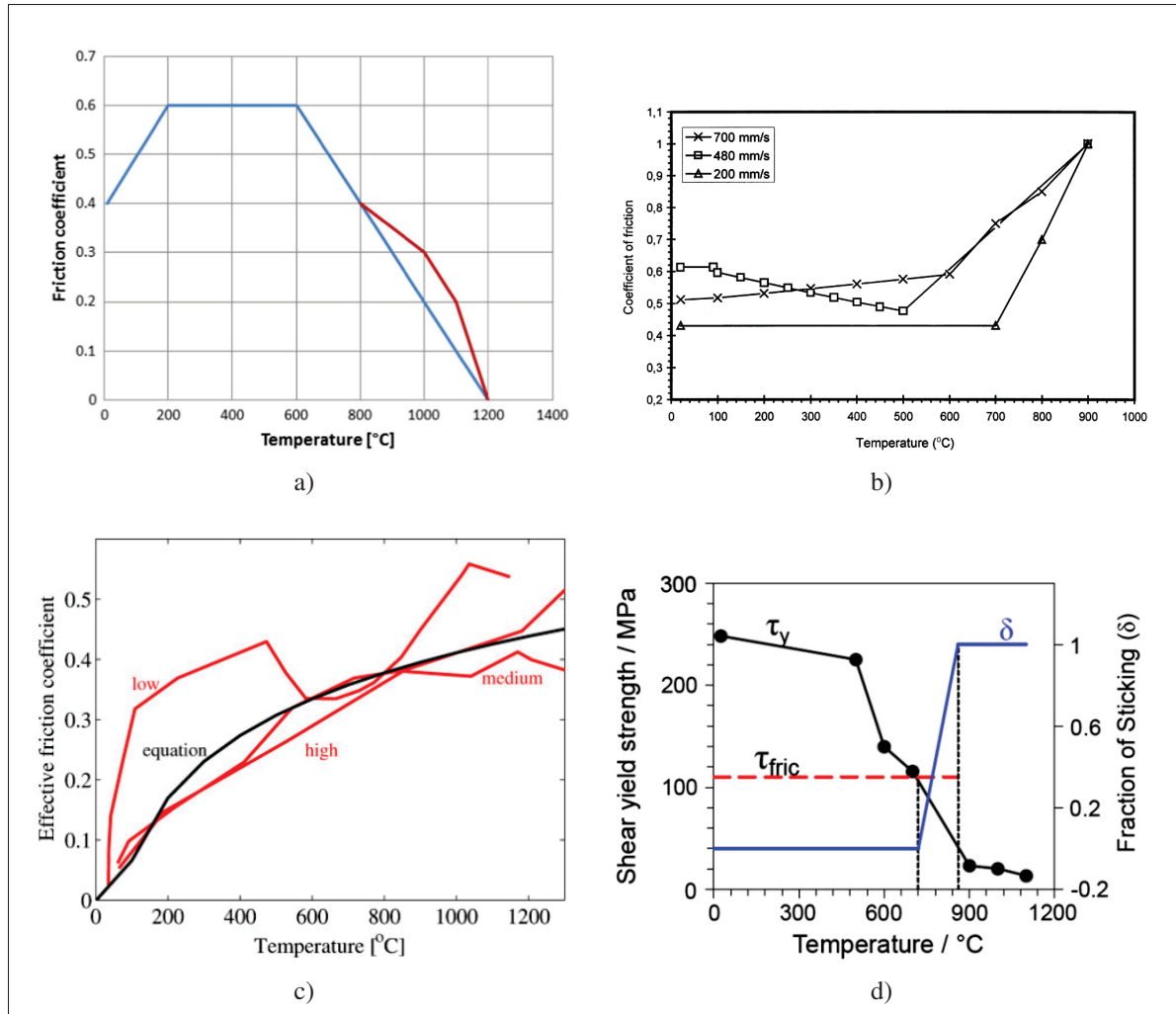
Figure 1.3   Friction coefficient models: a) modified Coulomb's coefficient (Original in blue by Li *et al.* (2010) and modified by Maio *et al.* (2016) in red), b) Friction coefficient used by Vairis & Frost (2000), c) effective friction coefficient under different energy input rates (red) and mathematical fit (black) by Schröder *et al.* (2015), d) stick-slip friction model by Maalekian *et al.* (2008)

1.1.2   Process Characteristics

The LFW is a self-regulating process (Dalgaard (2011); McAndrew *et al.* (2017)). Once, sufficient heat has been provided to soften the weld line, the viscoplastic layer formed at the latter is flowing due to the process loading - the applied force, the high temperature, and the oscillations - and behaves like a fluid. The weld line cannot sustain the constraints it is subjected to, and so, collapses and flows. Therefore, the friction between the two workpieces

is less than it used to be, as a result, the temperature at the weld line decreases. While the viscoplastic layer is being expelled, new matter is brought to the weld line due to the axial shortening. Since the weld line is colder, it hardens itself and the friction between the two workpieces increases. As a consequence, the heat power input increases and soften the new matter which will collapse when the mechanical threshold is reached. Thus, multiple mechanisms are involved in establishing and keeping that cycle.
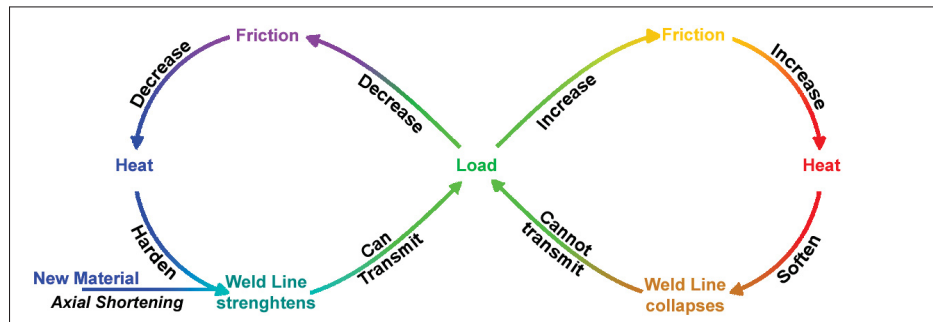
Figure 1.4   Linear Friction Welding (LFW) self-regulating cycle

1.1.2.1   Axial Shortening

Axial shortening is the consequence of the weld line collapsing under the process loading: shearing and compression stresses. As it can be seen in Figure 1.5, the axial shortening, or upset, is hardly noticeable at the beginning of the LFW, less than a $0.1\,\mathrm{mm}$. It measures only the elastic deformation of the workpieces due to the contact force applied on top of the workpiece. Then, when the weld line starts to collapse (around $1\,\mathrm{s}$) it becomes noticeable and increases up to its targeted value. Schröder *et al.* (2015) defined a conditioning period when the upset is minimal and starts to increase, then, an equilibrium period during which the upset rate remains almost constant (Figure 1.5).

12
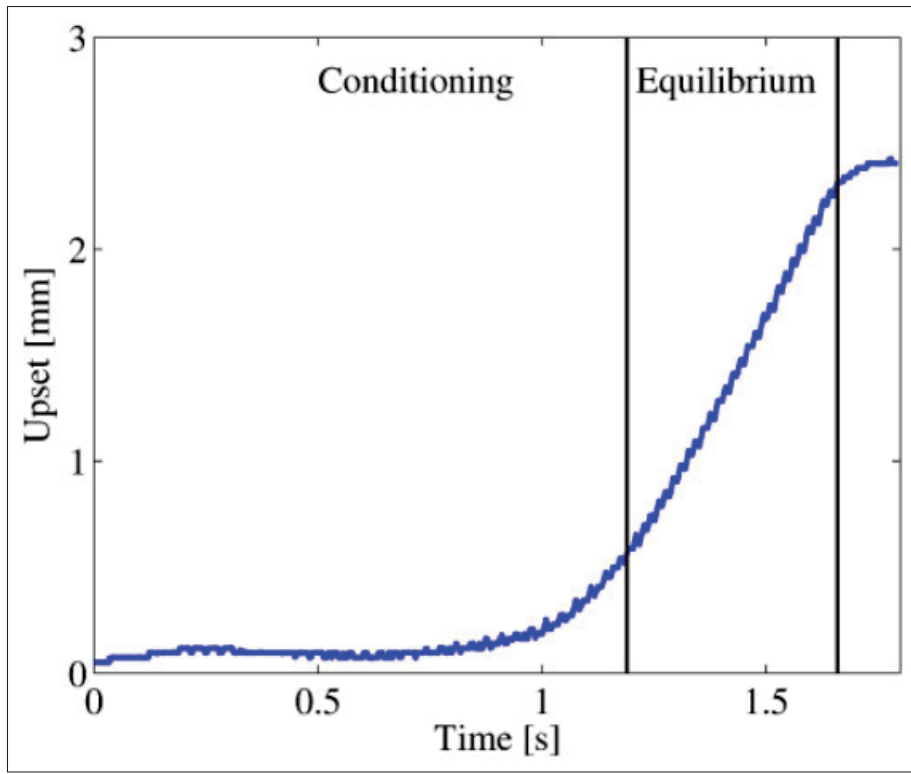
Figure 1.5   Axial shortening during the Linear Friction Welding
(LFW) separated by phase (Schröder *et al.* (2015))

The axial shortening is a control and a design parameter at the same time. So, as soon as it is reached, the weld can be considered completed and the post-processing phases may start (Section 1.2.2.4). During the equilibrium period, process and physical parameters such as axial-shortening rate or temperature, have little variations (Vairis & Frost (1998); McAndrew *et al.* (2014, 2015a,b, 2016, 2017); Ceretti *et al.* (2010); Schroeder *et al.* (2012); Fratini *et al.* (2012); Li *et al.* (2008); Grujicic *et al.* (2012)). During the self-regulating cycle (Figure 1.4), the axial shortening brings new matter to the weld line and contributes to form a sound-joint. Figure 1.6a shows that the axial shortening is influenced by the thermal power input. For an identical upset value of 1.5 mm, Schroeder *et al.* (2012) showed that less time is required to reach the target value with a high thermal power input than with a lower one. According to Equation 1.8, a high thermal power input implicates at least one high value of the process parameters: both amplitude and the frequency affect the ability of the oscillations to move and expel the material at the weld line, and the contact force extrudes it. In addition, as reported in

Figure 1.5, the evolution of the axial shortening seems linear according to time at some point in the process. McAndrew *et al.* (2015b) conducted statistical analysis, giving an average of the axial shortening rate according to the process parameter. Turner *et al.* (2011) have shown experimentally that the axial shortening rate (*v*) is directly linked to the process parameters through the thermal power input (Figure 1.6b), and that relationship is linear. These findings can be used to approximate other process parameters such as the temperature during the period when the axial shortening rate is constant.
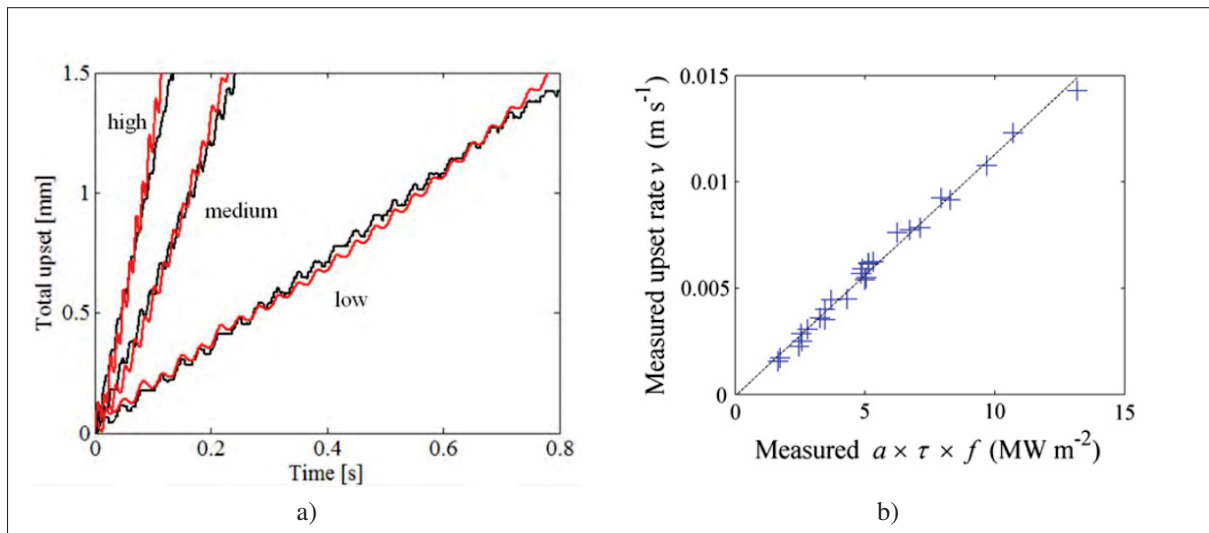
Figure 1.6   Axial shortening evolution and thermal power input influence: a) Influence of the thermal power input on the axial shortening: modeled (red), experiments (black) (Schroeder *et al.* (2012)), b) Variation of the measured upset rate during LFW with the product of the amplitude *a*, frequency *f* and the resultant mean shear stress arising (τ) (Turner *et al.* (2011))

1.1.2.2   Temperature Distribution

The heat equation (Equations 1.10) can be solved independently of its deformation counterpart. Vairis & Frost (2000) simplified the heat equation to a unidirectional problem based on the "*heat flux being applied to a solid bounded by two parallel planes*" approach, described by Carslaw & Jaeger (1959). They suggested an analytical solution (Equation 1.13) of the

temperature (T) at any distance from the interface (x) during the initial phase of the process (Paragraph 1.2.2.1) assuming that:

- The contact area increased linearly during that phase.
- There is not heat loss to the dies and the environment.
- The friction coefficient increased from 0.25 to 0.5.
- No reciprocal motion was considered.

$$T = \frac{2^{m+1} q_0 \kappa^{\frac{1}{2}} t^{\frac{m+1}{2}} \Gamma\left(\frac{1}{2}m+1\right)}{\kappa}$$
$$\sum_{n=0}^{\infty} \left\{ i^{m+1}\text{erfc}\left(\frac{(2n+1)L_0 - x}{2(\kappa t)^{\frac{1}{2}}}\right) + i^{m+1}\text{erfc}\left(\frac{(2n+1)L_0 + x}{2(\kappa t)^{\frac{1}{2}}}\right) \right\} \quad (1.13)$$

with ($\kappa = \frac{\lambda}{\rho c_p}$) the thermal diffusivity, (Γ) the Euler gamma function, (t) the time, (L_0) the workpiece length. Vairis & Frost (2000) established two thermal models: one with constant material properties and the second with thermo-dependent material properties. However, the first model (with constant material properties) deviates from the thermocouple measurements whereas the second model (with thermo-dependent material properties) tends to agree with experimental temperature measurements (Figure 1.7). Turner *et al.* (2011) put forward an analytical solution of the temperature distribution when the axial shortening rate is constant. Using the characteristic that the process is in a steady state period, Turner *et al.* (2011) defined a steady moving frame to solve the heat equation (Equations 1.10) and they obtained:

$$T = T_0 + \left(T_{flash} - T_0\right)\exp\left(-\frac{vx}{\alpha}\right) \quad (1.14)$$

with (α) the thermal diffusivity, assumed to be temperature independent. However, this approach may be used for the very first stages of the LFW to obtain the temperature distribution.

But Vairis & Frost (2000) highlighted the need to consider temperature-dependent properties to model the process.
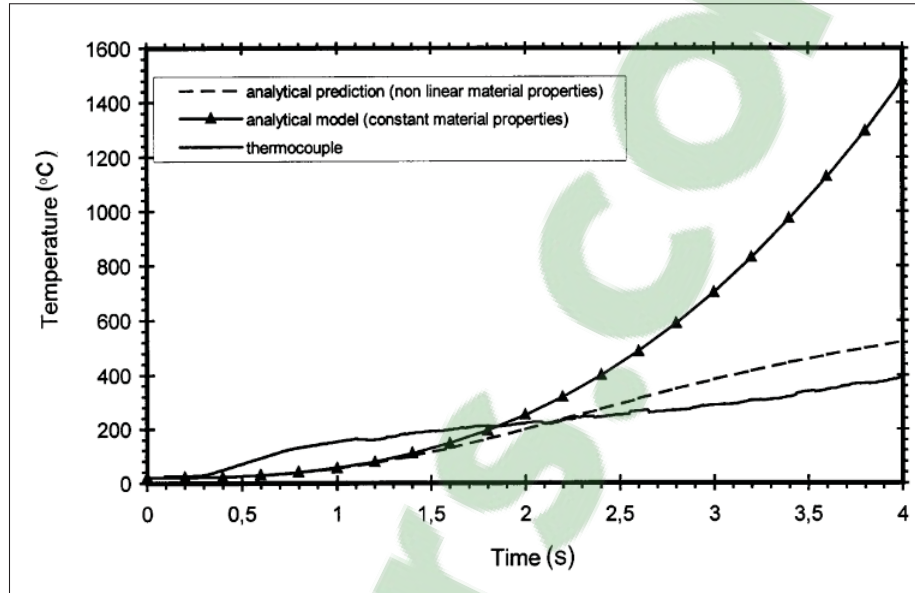
Figure 1.7   Comparison between experimental and analytical
model temperature data for the Initial Phase (Phase I) from
Vairis & Frost (2000)

For experimental studies, thermocouples are embedded into the workpiece to measure the temperature at various distances from the weld line (Figure 1.8a). Positioning thermocouples inside a workpiece has been a long-standing issue. They are usually positioned in the upper workpiece and because of the severe deformation and the axial shortening, the thermocouple may be crushed during the process (Dalgaard (2011)). Therefore, no thermocouple can be placed directly at the weld line and their position may change during the process. Figure 1.8b reports the temperature measured at those thermocouples, indicating the process phases (Section 1.2.2). It is segmented into four phases from one to four, representing the Initial, Transition, Equilibrium and Deceleration phases respectively according to Vairis & Frost (1998) definition. The figure depicts a rapid temperature increase near the weld line for the thermocouple at 0.3 mm whereas the temperature farther away, at 4.5 mm, seems to be delayed at the beginning and almost proportional in regards to the process duration. During phase 3 in Figure 1.8b, the temperature

suddenly drops for the thermocouples near the weld line (0.3 mm and 1 mm). One can argue that the thermocouples were damaged during the process due to the severe deformation that the weld line undergoes and the axial shortening brought the thermocouples to the weld line. However, the temperature recording during the first period can be considered reliable as no axial shortening is occurring. Due to the self-regulating characteristic of the LFW, the temperature is expected to reach a quasi-steady state with few variations (Figure 1.9b). McAndrew *et al.* (2015b) model also depicts steady state during phase 3 (Figure 1.8b) and shows good agreement with the thermocouples especially away from the weld line (4.5 mm) where the axial shortening will have no impact i.e. the thermocouple will move through the process but will not reach the deformed zone.
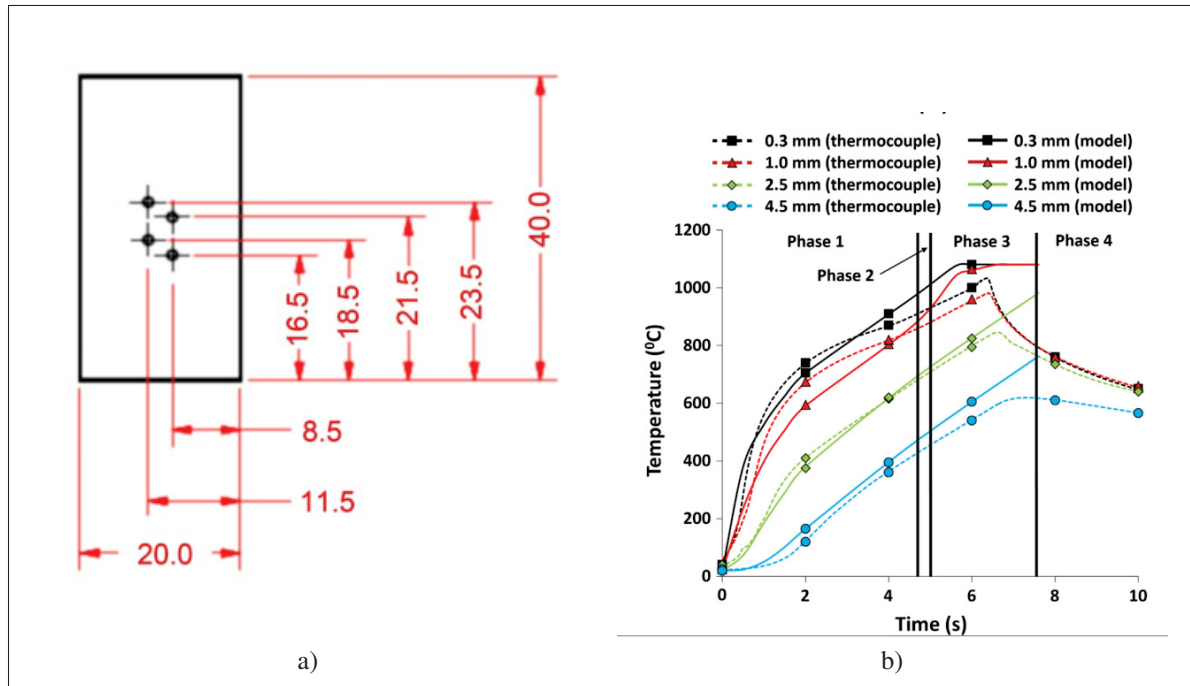
Figure 1.8   Thermocouples positions inside a workpiece to monitor the temperature evolution during the weld: a) Thermocouple's positions (0.3 mm, 1 mm, 2.5 mm, and 4.5 mm from the weld interface) used by McAndrew *et al.* (2015b), b) The thermal histories between a model and an experiment on Ti-6Al-4V ($a = 1.5$ mm, $f = 20$ Hz, $F_c = 100$ kN, $s_{target} = 3$ mm) (McAndrew *et al.* (2015b)) at different depths from the weld line

Even though Vairis & Frost (2000) provided an analytical solution of temperature distribution, the assumptions made to solve the problem, do not reflect the reality of the process. Numerical approaches can solve the process complexity (Li *et al.* (2010); Turner *et al.* (2011, 2012); Grujicic *et al.* (2012); McAndrew *et al.* (2014, 2015b)): workpieces motion, friction interaction, temperature dependent properties, and predict the temperature distribution (Figure 1.9). Such approaches allow to study the process parameters influence on the temperature evolution throughout the process and optimize them.
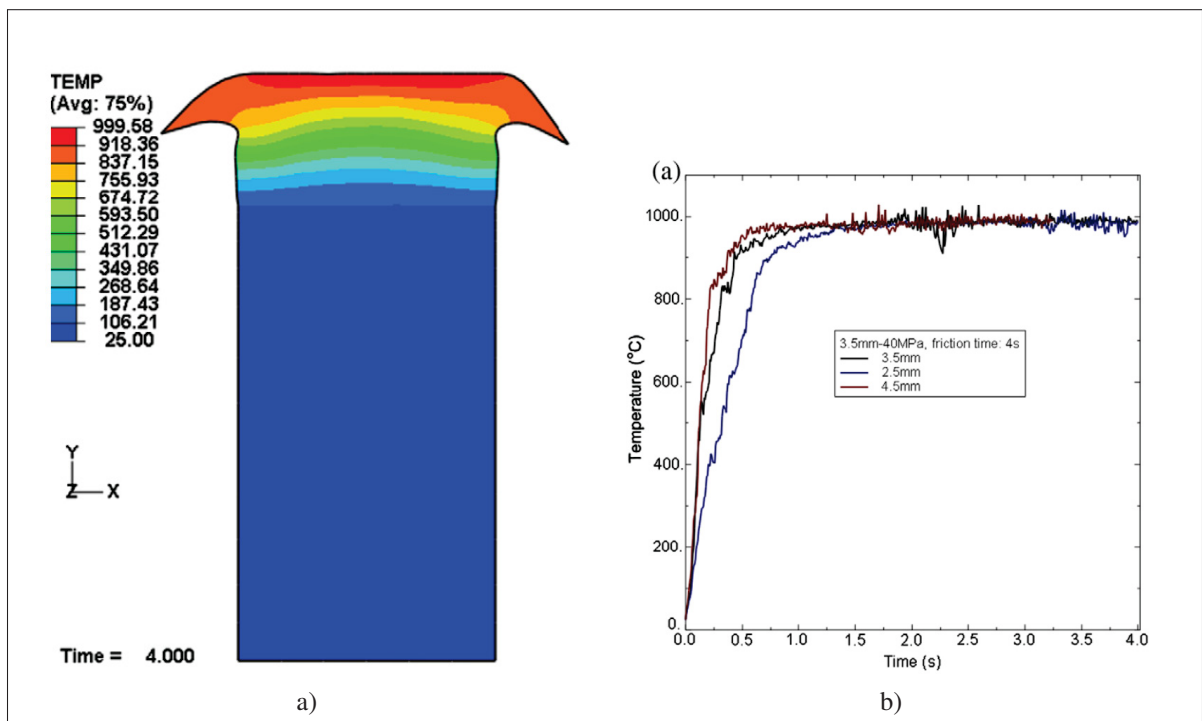
Figure 1.9   a) Temperature distribution in the specimens obtained under $a = 2.5\,\text{mm}$ and a friction time of 4s (Li *et al.* (2010)), b) temperature evolution of the central element at the interface and unilateral axial shortening (Li *et al.* (2010))

1.1.2.3   Heat Affected and Thermo-Mechanical Affected Zones

A consequence of the temperature increase and the severe deformation at the weld line is the formation of a Heat Affected Zone (HAZ) and a Thermo-Mechanical Affected Zone (TMAZ). First, the Heat Affected Zone (HAZ) is due to the temperature increase which alters the material

properties such as the Young's modulus and the phase transformations (e.g. α to β phase for titanium alloys). The literature barely provides a value when the HAZ starts, however, it is usually taken when the changes in the material properties become important: for titanium alloy, it can be assumed that the HAZ temperature is before the β transus temperature. The HAZ expands at the beginning of the process due to the heat diffusion and reaches a limit (x_{HAZ}). A competition is happening between the heat diffusion inside the workpiece that increases the HAZ size and the axial shortening that bring new cool matter to the weld line which reduces the HAZ. Schroeder *et al.* (2012) considered Turner's equation (Equation 1.14) to deduce the HAZ extend for a Ti-6Al-4Valloy during the steady state, assuming that the HAZ temperature is 900 °C:

$$x_{HAZ} = \alpha \rho A \log \left(\frac{T_{flash} - T_0}{T_{HAZ} - T_0} \right) H \left(T_{flash} \right) \tag{1.15}$$

with α the thermal diffusivity, A the joint-interface area, and $H(T_{flash})$ the flash specific enthalpy. Despite the fact that the thermal diffusivity was considered to be temperature-independent, resulting in an elevated T_{HAZ}, Schroeder *et al.* (2012) obtained good agreement between their analytical model and experimental measurements for a heat input higher than 5 kW.
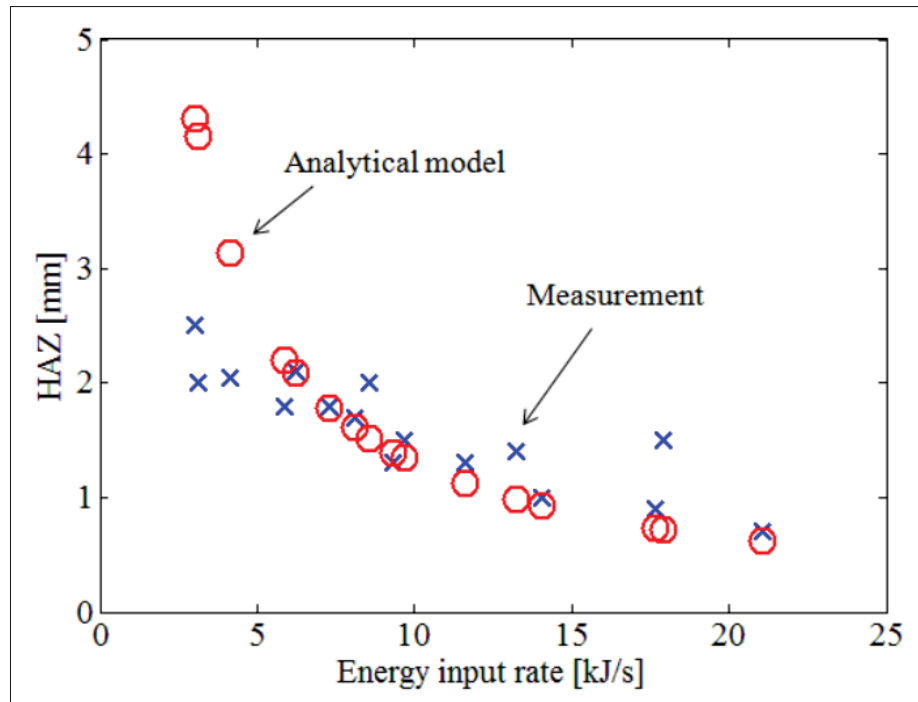
Figure 1.10   The width of HAZ decreases with increasing energy
input rates (Schroeder *et al.* (2012))

Second, the Thermo-Mechanical Affected Zone (TMAZ) is due to the severe deformation occurring at the weld line. Figure 1.11 depicts different zones among the TMAZ. It can be seen that microstructural changes such as grain refinement occurs at the weld line. In Figure 1.11a, the TMAZ is between the Weld Center Zone (WCZ) and the parent material. The latter is almost unchanged: a small portion near the TMAZ is hosting the HAZ. The WCZ is the core of the weld line, it is heavily sheared and it is expelled by the oscillations, forming the bond between the two initial workpieces. At the edge of the sample, a funnel shape can be seen on the metallography (Figure 1.11b). It is the junction between the flash and the workpiece. As the viscoplastic matter is no longer constrained, it flows in every direction.

20
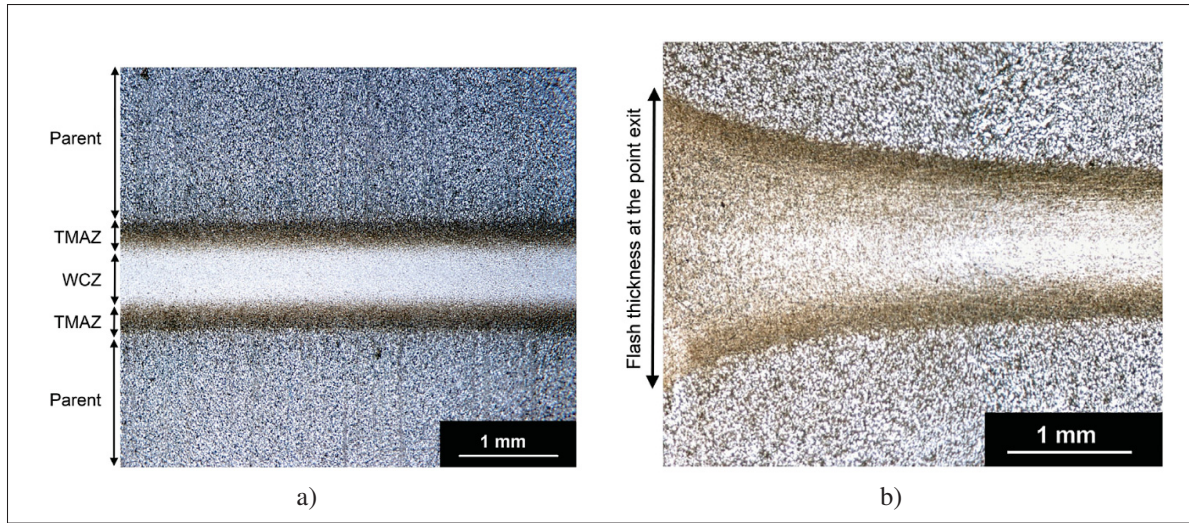
Figure 1.11   Weld line metallographic observations (McAndrew *et al.* (2015b)): a) a metallographic specimen showing the weld center zone (WCZ), Thermo-Mechanical Affected Zone (TMAZ), parent material (parent) and the TMAZ thickness, b) Flash thickness at the point of exit

1.1.2.4   Microstructural Changes

Figure 1.12 present microstructural changes at both the TMAZ and the WCZ. After etching and under an optical microscope, the LFW joint has a recognizable pattern: in figure 1.12, a little gray line with almost indistinguishable texture separate both parent material (upper and lower workpieces). Wanjara & Jahazi (2005); Dalgaard (2011); Grujicic *et al.* (2012) have studied the impact of the LFW on the microstructure and have pointed out the present of Dynamic Recrystallization (DRX) and grain refinement in both TMAZ and WCZ.
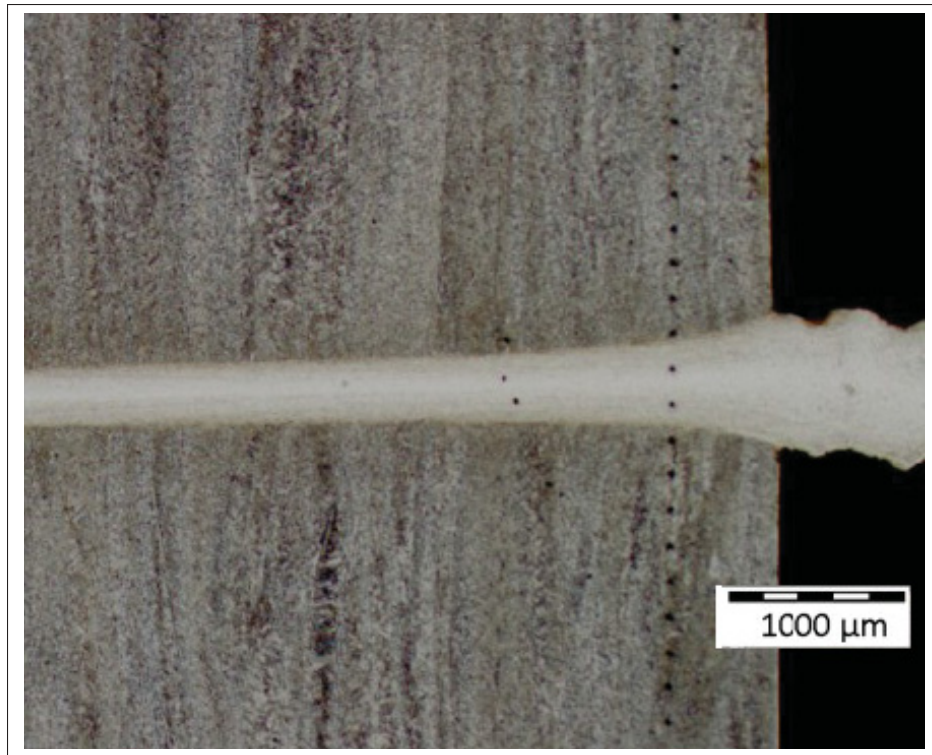
Figure 1.12   Metallography of the weld line from Dalgaard
(2011) experiments (Weld#4-17)

The figure 1.13a depicts an LFW sample under an optical microscope after etching to reveal the grains. The weld line is 0.170 mm wide and present almost no grain boundaries under optical observations compared to the visible grains in the TMAZ and parent material. In the TMAZ near the parent material, the grains are almost unchanged, then they elongate, shrink and orient themselves in the oscillations direction, to finally become imperceptible. Figure 1.13b illustrates the Scanning Electron Microscopy (SEM) metallography of the TMAZ and WCZ of a Ti-6Al-4V alloy LFWed. It reveals the titanium phases (α in dark gray and β in lite gray) and the texture of the WCZ. According to Wanjara & Jahazi (2005) and based on the temperature predicted at the weld line, only titanium β phase should be present at the weld line. Figure 1.13b shows less α phase in the WCZ than in the TMAZ, supporting that conjecture. In addition, the reorganization of the microstructure and texture that can be seen as the α and β zones are shrunk and oriented toward the oscillations direction.
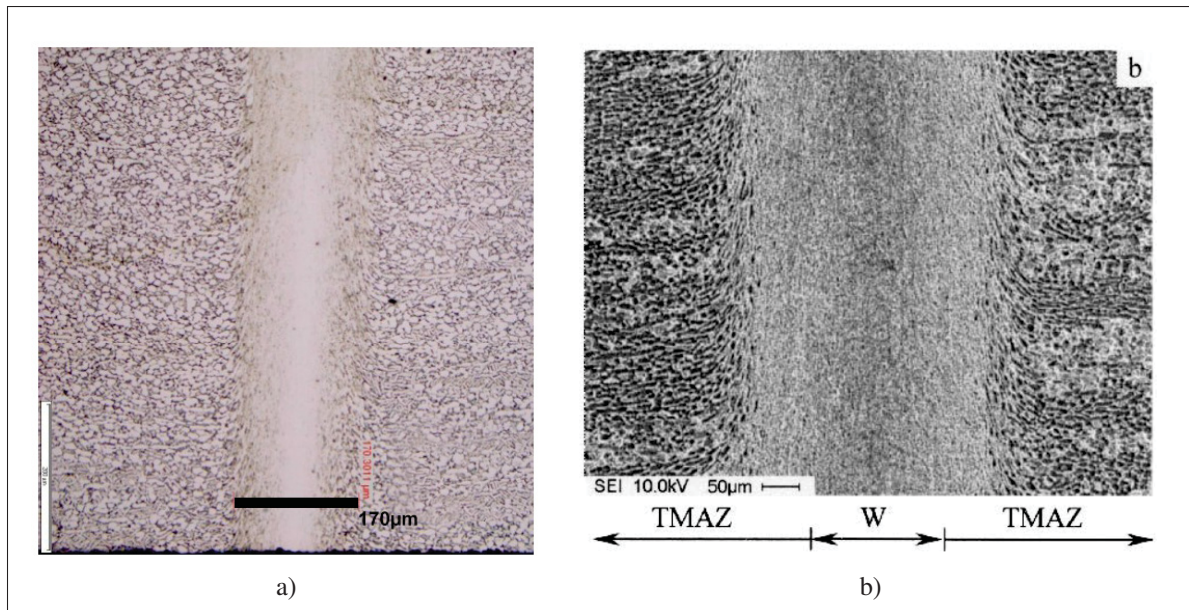
Figure 1.13   Close up on the weld line observations: a) Metallography of the weld line
from Dalgaard (2011) experiments (Weld#4-21), b) Scanning electron microscope
images of a typical weld zone in a Ti-6Al-4Vlinear friction welded sample
Wanjara & Jahazi (2005)

Karadge *et al.* (2007) have studied the texture of Ti-6Al-4V alloy both in laboratory and after
LFW and found two different textures. They show that the weld line texture is aligned with the
reciprocating motion as it can be seen in Figure 1.13b. But farther away from the weld line in
the TMAZ, the texture is misaligned with the oscillations directions, forming bands converging
on the weld line, as it is seen in Figure 1.13 in the TMAZ near the weld line. According to
Karadge *et al.* (2007) and McAndrew *et al.* (2017), the impact of the LFW on the texture is not
yet understood.
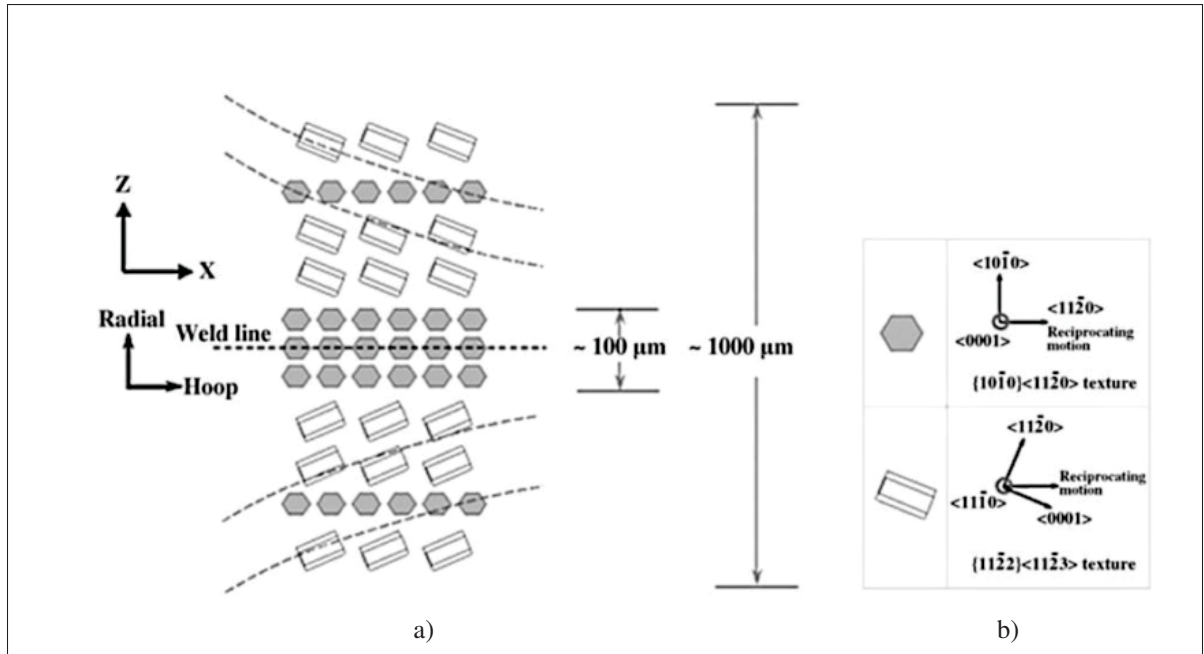
Figure 1.14   Crystallite orientation and Texture type in an LFW specimen (Karadge *et al.* (2007)): a) Crystallite orientation in the Plastically Affected Zone (PAZ) in a full-scale specimen, b) Texture type

1.1.2.5   Flash Morphology

The extruded material, called flash, is a result of axial shortening. Schröder *et al.* (2015) reported that the matter is expelled in all directions but mainly in the oscillating direction, and then, in the transverse direction (Figure 1.15a). Flashes can be described as having a smooth (Figure 1.16a) or rippling (Figure 1.16b) morphology. Schröder *et al.* (2015) have put forward a criterion ς (Equation 1.16) to predict the formation of a smooth morphology ($\varsigma > 1$) or a ripple morphology ($\varsigma < 1$) (Figure 1.15b) That criterion compares, w_{PAZ}, the width of the Plastically Affected Zone (PAZ) in the in-plane (welding) direction to a, the oscillations' amplitude. If the oscillations' amplitude is greater than the width of the PAZ the flash is separated from the workpiece, and so, forms a ripple when the workpiece comes back.

$$\varsigma = \frac{w_{PAZ}}{a} \tag{1.16}$$
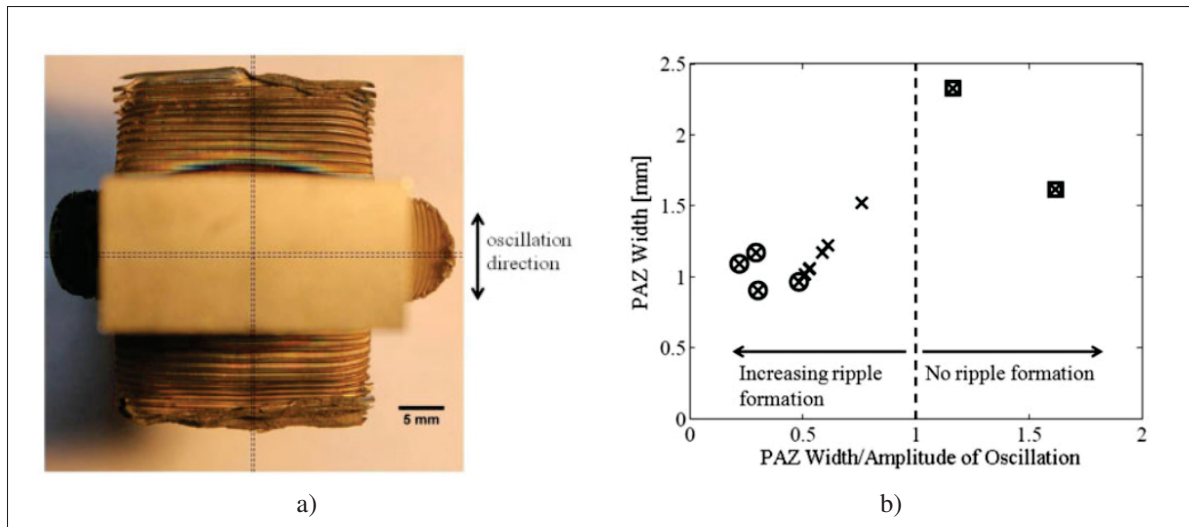
Figure 1.15   Flash morphology (Schröder *et al.* (2015)): a) Top view of a sample at the end of the LFW process with ripply flashes, b) Plot illustrating conditions for which rippled morphology of flash is observed. Squares indicate no ripple formation, circles indicate large ripple formation and crosses represent small ripples only
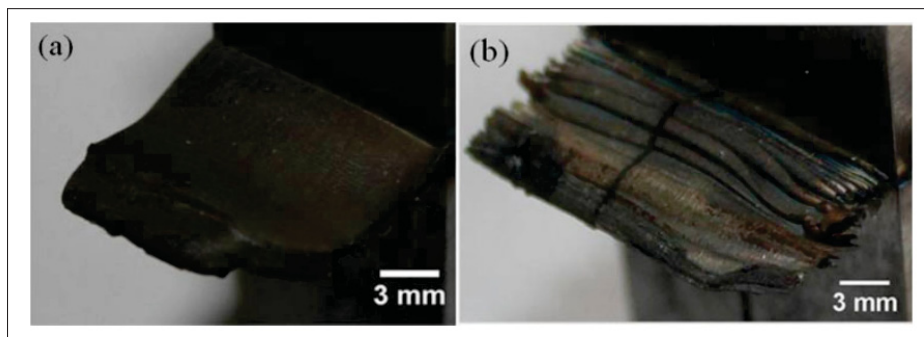
Figure 1.16   Flash morphologies for LFW welds (Schröder *et al.* (2015)): a) low amplitudes give a smooth extrusion with, b) high amplitudes form a rippling flash

Schröder *et al.* (2015) also investigated the correlation between the process parameters and the flash morphology (Figure 1.17), and reported that each parameter has a visible influence on the flash morphology:

- A low frequency will create a compact flash whereas a high frequency will produce a long and wavy flash.

- A low amplitude will give a long and thick flash whereas a high amplitude will end with a chaotic flash shape.
- A low pressure will form a short and wavy flash whereas a high pressure will generate a straight and long flash.

The purpose of qualifying flash morphology is to determine visual criteria that characterize a sound-joint.
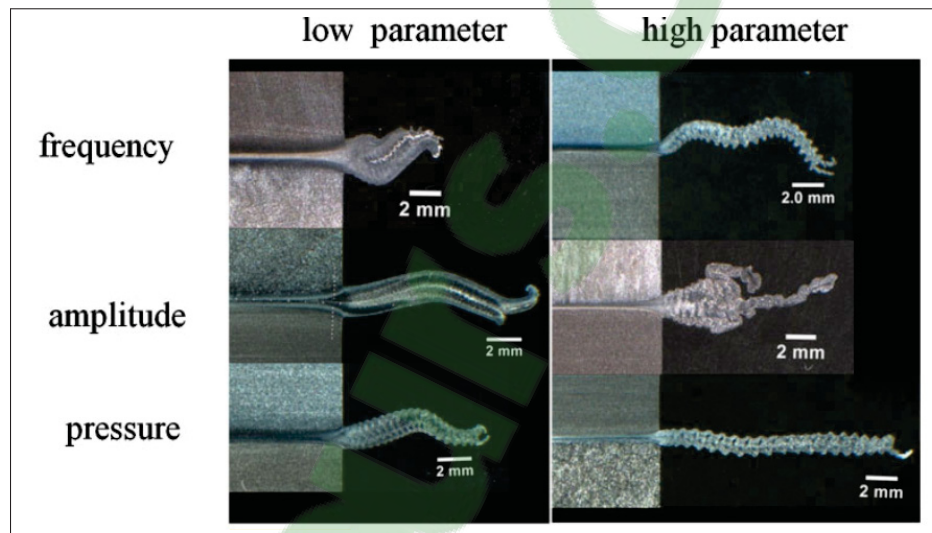
Figure 1.17   Flash morphologies according to the process
parameters. Schröder *et al.* (2015)

1.2   Numerical Model Representations

The numerical modeling of the LFW process has improved its understanding and made more affordable process parameters optimizations. In the recent years, the numerical simulations have become more advanced and efficient allowing fully coupled 3D simulations. Figure 1.18 summarizes the different approaches and boundary conditions used for modeling the LFW:

1. The Thermo-Mechanical Analysis (TMA) approach considers both displacements and temperature Degree of Freedom (DOF). It includes the oscillations in the simulations, and so, one workpiece is constrained in displacement as follows:

$$u_x = u_{wp} = a \sin\left(2\pi f t\right) \tag{1.17}$$

with (u_{wp}) the lower die imposed displacement. It is the traditional approach to model the workpiece's oscillations. Different boundary conditions can be used with this approach such as:

- Deformable / Deformable Bodies (DDB) (Fratini *et al.* (2012); Geng *et al.* (2019a))
- Deformable / Rigid Bodies (DRB) (Vairis & Frost (2000); Li *et al.* (2010))
- Single Body (SB) (Turner *et al.* (2011); Fratini & La Spisa (2011))

The numerical models following this approach are considered as oscillatory models.

2. The Heat Transfer Analysis (HTA) approach considers only the temperature DOF. As there is no displacement, it is assumed that the workpieces are stationary:

$$u_{wp} = 0 \tag{1.18}$$

As a consequence, a surface heat flow is added at the welding surfaces to account for the heat input generated by the oscillations ($\bar{Q}_{total} = 4\mu F_n a f$ - Equation 1.9). It is a recent approach and it has shown significant time reduction to run as the oscillations are not rendered. The same boundary conditions have been used as for the TMA approach:

- DDB (McAndrew *et al.* (2014, 2015a,b, 2016); Jedrasiak *et al.* (2018))
- DRB (Bühr *et al.* (2017))
- SB (*no publication has used this approach in the literature, yet*)

Such models are referred as thermal models.
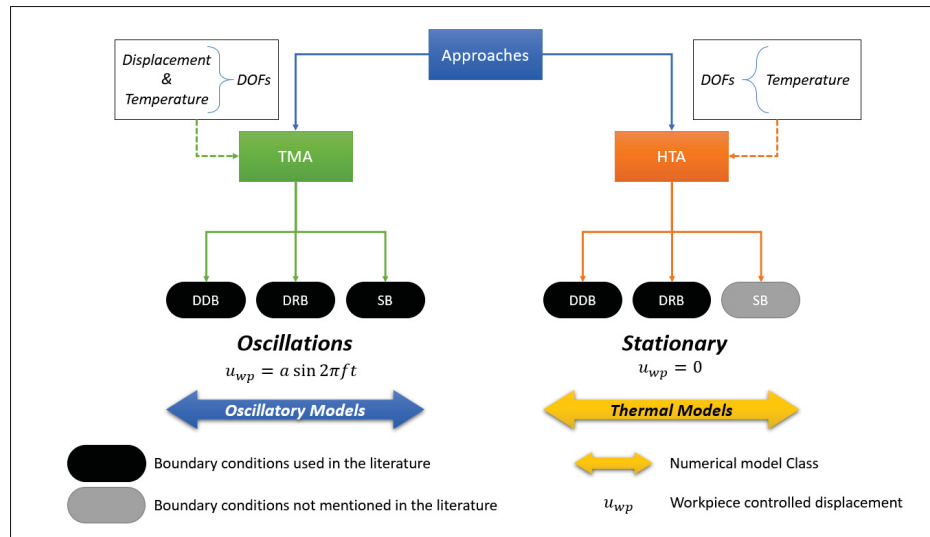
Figure 1.18   LFW numerical approaches and representations

1.2.1   Boundary Conditions and Meshing

1.2.1.1   Deformable - Deformable Bodies

Under a TMA approach, both workpieces are modeled and considered deformable. Figure 1.19a depicts the oscillating workpiece at the bottom and the stationary one on top. The contact pressure is applied on the top of the workpiece and perpendicular displacement to the oscillations direction is allowed to account for the axial shortening. The bottom surface of the oscillating workpiece is constrained in the parallel direction of the oscillations to replicate the lower die. A contact interface is defined according to the friction model used (Figure 1.3) which defines the friction heat generation in the numerical model. The dies are usually considered as heat sink, so, a high thermal transfer coefficient (1×10^4 W·m^{-2}·K^{-1} - Turner *et al.* (2011)) between the dies and the workpieces is usually implemented. A convection coefficient is set for the surfaces in contact with the environment (surfaces that are not in contact with the dies). The direction of the convection is normal to the surface and the coefficient of convection is between 10 W·m^{-2}·K^{-1} (Turner *et al.* (2011)) and 100 W·m^{-2}·K^{-1} (Vairis & Frost (2000)).

The numerical challenges encountered with this approach are the computational resources

required to run the simulations and the workpieces numerical joining. Such simulation requires significant computational resources due to the elevated number of DOF and the refine mesh near the weld line (Figure 1.19a). The time required to run a simulation varies between few hours for 2D simulations and few days for 3D simulations. Without any additional subroutine, standard Finite Element Modeling (FEM) solvers are not able to predict the weld line joining by merging the meshes. As a result, the flash morphology obtained by this approach: separated flash for each workpiece, do not match those obtained experimentally for Ti-6Al-4V (Section 1.1.2.5). However, such subroutines are complex to implement and other numerical models can simulate the flash extrusion accurately such as a Single Body (SB) model.

Under a HTA approach, both workpieces are partially modeled and no motion nor contact pressure is introduced as there is no displacement DOF. The oscillations are replaced by their equivalent heat input:

$$\bar{q}_{total} = 4\mu p_n a f \tag{1.19}$$

with (p_n) the contact pressure. Bühr *et al.* (2017) have used both surface heat flux and heat per unit volume to account for the friction heat released in the workpieces at the joint. A perfect contact between the two parts is assumed and the interfaces with the environment are isolated. This approach requires a deep knowledge of the heat generation mechanism during the process, and therefore, relies on the friction model used (Figure 1.3). The main convenience of this approach is that it requires little computational resources as the total of DOF are reduced and does not require the parent material zone to be clamped by the dies (Figure 1.2). As a result, the time needed to run such models are reduced to minutes for the same process conditions. However, the main inconvenience is that no displacement is rendered so no flash prediction and the axial shortening may be obtained by mesh removal thanks to extensive subroutines and remeshing (Bühr *et al.* (2017)).
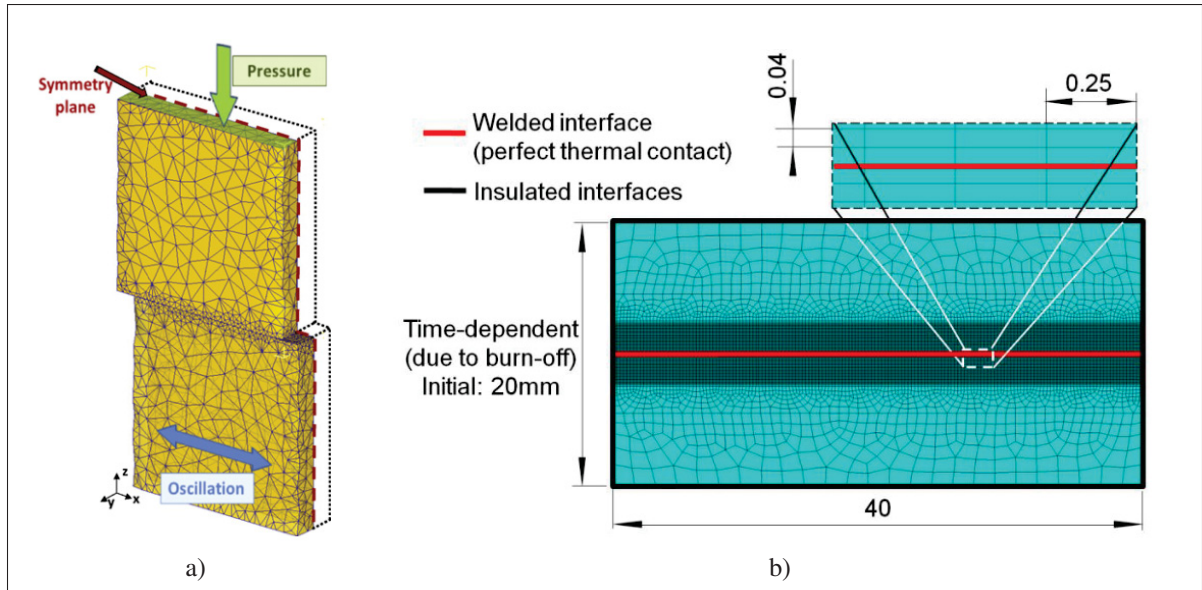
Figure 1.19   Deformable / Deformable Bodies (DDB) boundary conditions: a) for
Thermo-Mechanical Analysis (TMA) approach (Fratini *et al.* (2012)), b) for Heat
Transfer Analysis (HTA) approach (Jedrasiak *et al.* (2018))

1.2.1.2   Deformable - Rigid Bodies

The Deformable / Rigid Bodies (DRB) boundary conditions are a subset of the DDB ones. Only half of the DDB model is simulated, reducing the computational cost. Figure 1.20a shows the boundary condition under a TMA approach. The oscillating workpiece is replaced by a rigid oscillating surface but the other boundary conditions are identical (flipped upside-down in Figure 1.20a compared to Figure 1.19a). Under a HTA approach (Figure 1.20b), a fourth (in 2D) or an eighth (in 3D) of the actual setup is represented using the symmetry of the problem to reduce the number of DOF. Then, it is proceeded as a regular HTA DDB model with adapted equations.

Despite, the run time reduction, the principal issue is that they do not model the interaction between the upper and the lower workpieces. Under a HTA approach, the problem symmetry can be used to extrapolate a full-size model. But with a TMA approach the second workpiece cannot be extrapolated as there is no direct symmetry in the problem. In addition, those boundary conditions do not allow an accurate flash prediction and workpieces merging. This

approach may be used when little computational resources are available or for a first numerical approach.
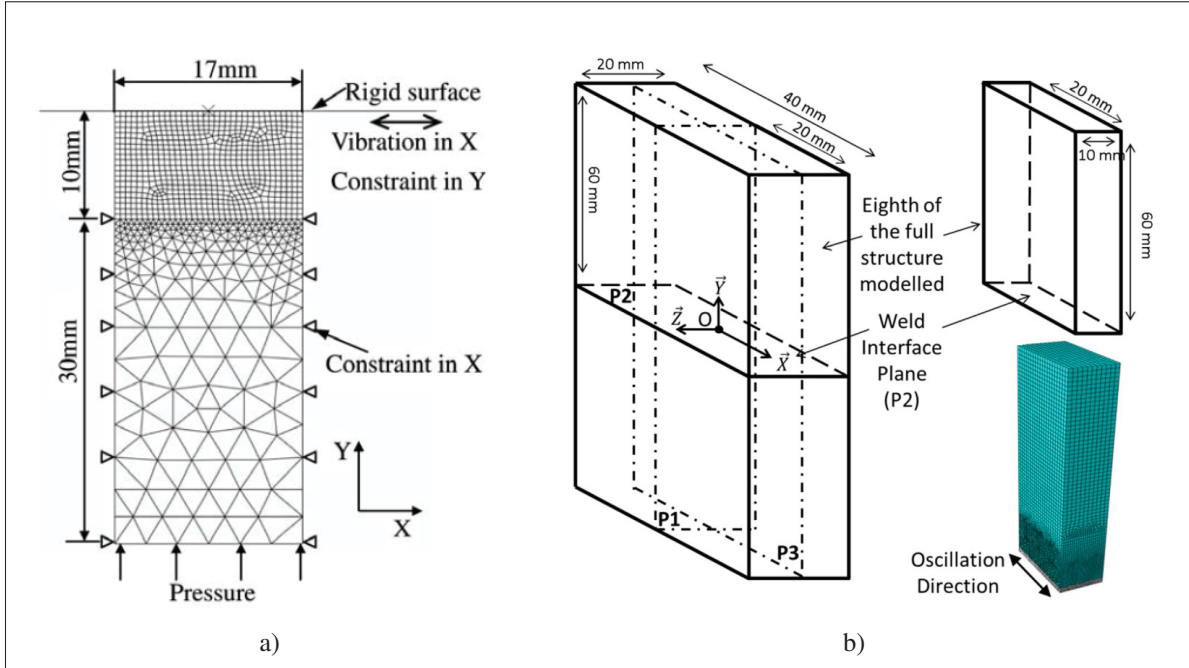
Figure 1.20   Deformable / Rigid Bodies (DRB) boundary conditions: a) for Thermo-Mechanical Analysis (TMA) approach (Li *et al.* (2010)), b) for Heat Transfer Analysis (HTA) approach (Bühr *et al.* (2017))

1.2.1.3 Single Body Model

The Single Body (SB) boundary conditions are based on the hypothesis that the two workpieces have merged virtually. Grujicic *et al.* (2012) have shown that the deformation occurring at the beginning of the process is negligible until the two workpieces merge. As a consequence, it requires the temperature distribution when the workpieces have merged. The latter is not well defined in the literature and subject to interpretation: Turner *et al.* (2011) assumed multiple temperature distribution, or McAndrew *et al.* (2015b) assumed an arbitrary temperature distribution (Figure 1.21b). An oscillating die is modeled at the bottom of the workpiece (Figure 1.21) and a top die applies the contact pressure. As there is no interface between the workpieces, no friction model is required and the heat generated is due to the mechanical

deformation. However, it requires robust material constitutive data to model accurately the plastic deformation occurring during the flash extrusion (Turner *et al.* (2014)). The workpiece is not constrained in any direction as only the HAZ zone is represented to reduce the simulation run time. So far, SB boundary conditions are only used under a TMA approach, but , according to Bühr *et al.* (2017) recent publication, such boundary conditions could be used under a HTA approach, considering heat per unit volume generation in the WCZ.
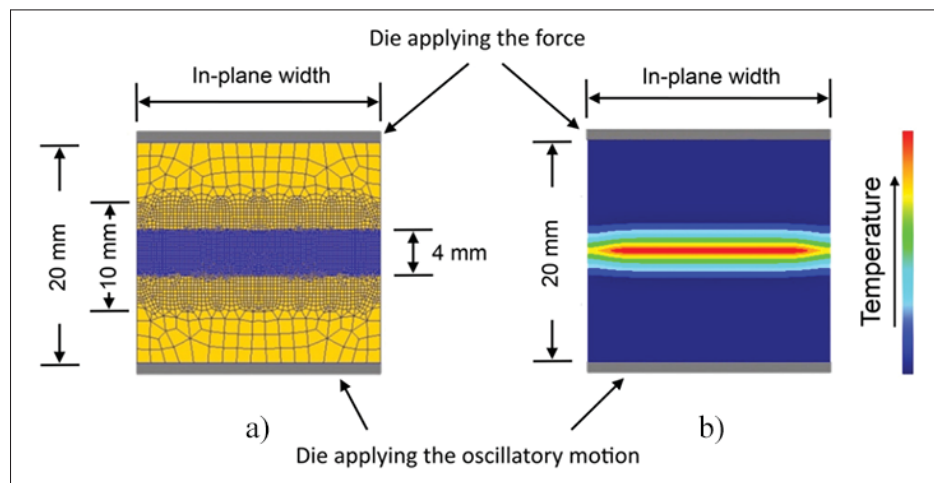
Figure 1.21   Single Body (SB) boundary conditions (McAndrew
et al. (2015a)): a) boundary conditions with the mesh, b)
temperature distribution used as initial conditions

1.2.1.4   Meshing

All the previous models have been conducted in both 2D or 3D. 3D models are mainly used for flash morphology and to study the flash extrusion directions. However, they are expensive to run from a computational point of view as they require at least 24h to compute on multi-core servers. On the other hand, 2D models require less computation time to run than 3D models and are used for parametric study (McAndrew *et al.* (2017)). Turner *et al.* (2011) have carry-out a mesh sensitivity analysis for parameters converge. They reported that the temperature, the plastic strain, the strain rate and the Von Mises stress converge for a smaller mesh size of 0.25 mm.

Figure 1.22a depicts the converge of the normalized parameter defined by:

$$\hat{P} = \frac{(P - \bar{P})}{\sigma_P} \tag{1.20}$$

with $\hat{P}$ the normalized parameter, P the parameter value, $\bar{P}$ the parameter average value and σ_P the standard deviation for the parameter range. Figure 1.22b shows that the run time increases exponentially as the mesh size diminishes because the number of nodes and elements are greater. The 2D assumption made is not always mentioned in the different publication excepted for plain strain assumptions (Maio *et al.* (2016); Yang *et al.* (2015)).
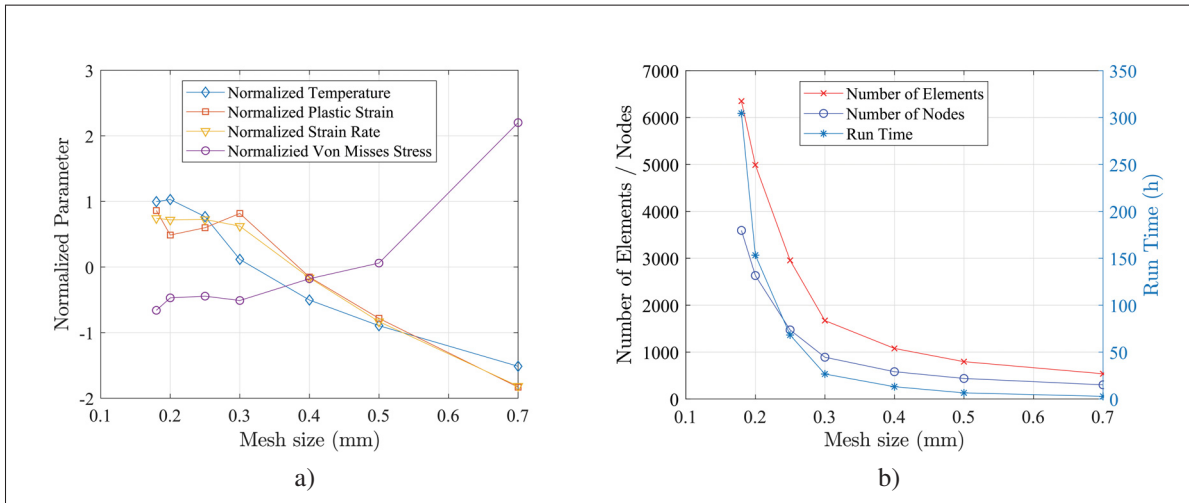
Figure 1.22 Mesh sensitivity study by Turner *et al.* (2011): a) Time needed to run the simulation according to the number of elements, nodes and mesh size for a 2D simulation, b) normalized parameter sensitivity

1.2.2 Process Phases Breakdown and Numerical Model Applicability

As it has been seen, multiple mechanisms occur during the LFW at different times of the process. Vairis & Frost (1998) have decomposed it into four phases: Initial Phase (Phase I), Transition Phase (Phase II), Equilibrium Phase (Phase III) and Post-Processing phase (Phase IV) including the Deceleration phase (Figure 1.23). Each phase is consecutive to its predecessor in

a manner that, if its purpose is not fulfilled, the process will result in a poor quality join. Many studies: Vairis & Frost (2000); Wanjara & Jahazi (2005); Ceretti *et al.* (2010); Sorina-Müller *et al.* (2010); Li *et al.* (2010); Fratini & La Spisa (2011); Bhamji *et al.* (2011); Turner *et al.* (2011); Zhao *et al.* (2014); Fratini *et al.* (2012); Grujicic *et al.* (2012); Schroeder *et al.* (2012); McAndrew *et al.* (2014, 2017); Buffa & Fratini (2017), including this study, rely on Vairis's definition to describe the LFW phases.
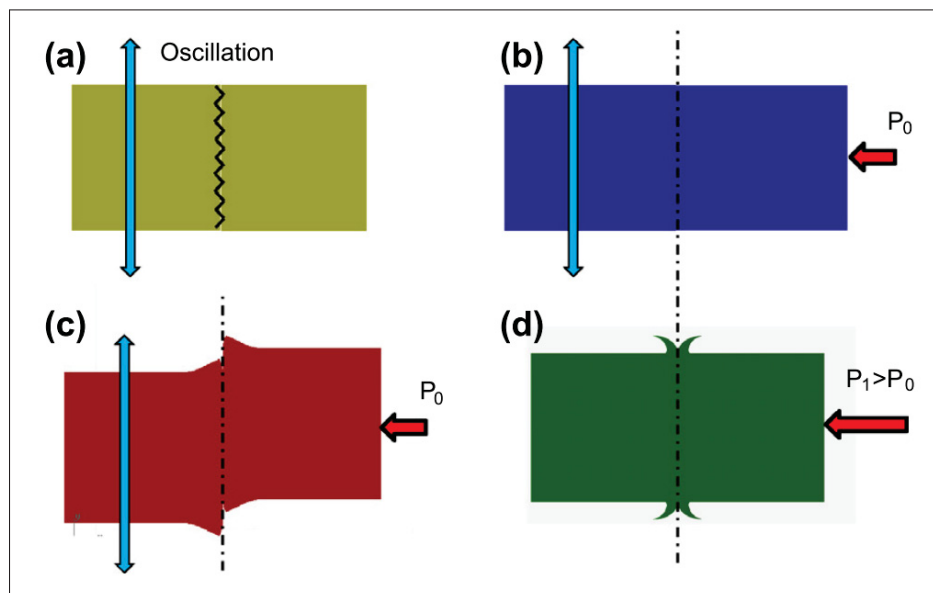
Figure 1.23   The LFW four phases: (a) Initial (b) Transition, (c) Equilibrium and (d) Deceleration phase (Fratini *et al.* (2012))

Meanwhile, some papers have broken down the process with a specific point of view. Bhamji *et al.* (2011) have divided the process from the machine point of view: the Conditioning, the Friction and the Forging phases. The authors linked the latter to Vairis's phase definition as the Conditioning phase begins the Phase I. The friction phase is overlapping Phases I to III (Figure 1.24). In the same manner, Schröder *et al.* (2015) defined two phases: the Conditioning phase and the Equilibrium phase. In contrast to Bhamji *et al.* (2011), the Conditioning phase spreads over the Phases I-II as defined by Vairis's and the Equilibrium Phase (Phase III) is identical for both. Then, the Forging phase is an additional phase usually used for titanium alloys to secure the joint, including a deceleration phase. Figure 1.24 shows the overlap

between different point of view to describe the process : Bhamji *et al.* (2011) for the machine actions, Vairis & Frost (1998) physical description, and Schröder *et al.* (2015) combining the two. Ergo, it is necessary to define specific transition criteria from one phase to another to obtain accurate numerical models for process parameters optimization.
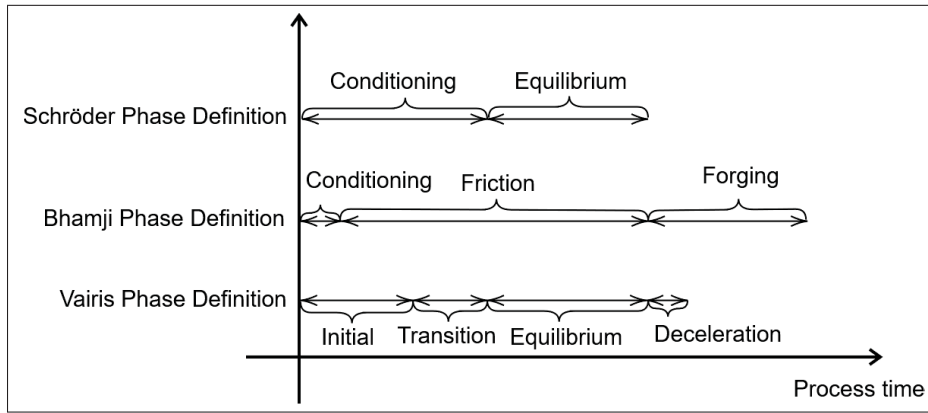
Figure 1.24   Linear Friction Welding (LFW) phase timeline
according to Vairis & Frost (1998); Bhamji *et al.* (2011) and
Schröder *et al.* (2015) definition

1.2.2.1   Initial Phase (Phase I)

The Initial Phase (Phase I) shall provide sufficient heat to transform the initial material at the weld line into a malleable layer. The oscillating motion (Equation 1.1) provides the thermal energy to soften the weld line, and produces a viscoplastic layer. This is the phase characteristic defined by Vairis & Frost (1998) and followed by many studies (Vairis & Frost (2000); Wanjara & Jahazi (2005); Ceretti *et al.* (2010); Sorina-Müller *et al.* (2010); Li *et al.* (2010); Fratini & La Spisa (2011); Bhamji *et al.* (2011); Turner *et al.* (2011); Zhao *et al.* (2014); Fratini *et al.* (2012); Grujicic *et al.* (2012); Schroeder *et al.* (2012); McAndrew *et al.* (2014, 2017); Buffa & Fratini (2017); Bertrand *et al.* (2018)). Furthermore, Vairis & Frost (1998, 2000) assumed that no penetration occurs during Phase I. This assumption was corroborated by Grujicic *et al.* (2012) as deformation occurring during this phase can be neglected when compared to the overall deformation induced by the flash extrusion. Therefore, the workpieces

keep their integrity during Phase I i.e. two distinguishable interfaces sticking with each other. Meanwhile, the reciprocal motion levels the contact surfaces by removing asperities which results in an increase of the contact surface and breaks down the contaminant layer, providing an oxide free surface and a near perfect joining area.

If insufficient heat is provided to the weld line, the literature agrees that the process will not move to the next phases and will produce a poor quality joint. For Ti-6Al-4V alloy, McAndrew *et al.* (2014) have determined an average temperature of 1000 °C across the weld line as the required temperature to satisfy Phase I completion criterion. This allows to use thermal models (Bühr *et al.* (2017)), to simulate Phase I which is more efficient than end-to-end models such as DDB (Fratini *et al.* (2012)) or DRB (Li *et al.* (2010)). In addition, the above thermal models could be used in actual industrial process for identifying the start and end of each phase allowing for phase-based process optimization.

However, it must be noted that in their analysis McAndrew *et al.* (2014) consider only an average condition across the weld line, making difficult to implement in a numerical simulation. This is an issue for phase-based chained simulations as there is no precise phase transition defined between Phases I and III.

1.2.2.2 Equilibrium Phase (Phase III)

The LFW process reaches its self-regulating state during Phase III (Vairis & Frost (1998); Dalgaard (2011)). The literature agrees that the workpiece experiences most of its axial short-ening until it reaches its targeted value. As soon as the wanted shortening is reached, the weld can be considered as completed and the post-processing phases (i.e. the deceleration, forging, cooling phase) start (Paragraph 1.2.2.4). During this phase, the axial-shortening rate and the temperature remain nearly constant Vairis & Frost (1998); Li *et al.* (2008); Ceretti *et al.* (2010); Schroeder *et al.* (2012); Fratini *et al.* (2012); Grujicic *et al.* (2012); McAndrew *et al.* (2014, 2015a,b, 2016, 2017).

Although, Phase III has been clearly identified in the literature, however, two distinct ap-

proaches are proposed regarding the conditions for its initiation. McAndrew *et al.* (2015a) and Fratini *et al.* (2012) propose Phase III starts when the axial shortening rate becomes constant, while, Vairis & Frost (1998); Ceretti *et al.* (2010), and Grujicic *et al.* (2012) consider that Phase III starts when the axial shortening becomes measurable by a Linear Variable Differential Transformer (LVDT) during the process. This approach is function of the equipment, and therefore difficult to implement into a numerical simulation. In addition, the first approach complies with the phase description and a clear separation between the self-regulating state from the rest of the process can help to better optimize the process through numerical simulation.

1.2.2.3 Transition Phase (Phase II)

Its purpose is to bring the weld line from its viscoplastic state at the end of Phase I to the continuous material extrusion state of Phase III. As the LFW process is continuous, the start and the end conditions of Transition Phase (Phase II) must match those of its predecessor and successor respectively. So, Phase II shall begin when sufficient heat has been provided during Phase I, as reported by Vairis & Frost (1998); Ceretti *et al.* (2010); Fratini & La Spisa (2011). Two approaches have been proposed in the literature: The first approach considers the absence of axial shortening proposed by Vairis & Frost (1998); Ceretti *et al.* (2010); Grujicic *et al.* (2012), despite the softening of the material and the axial loading. The second approach considers the mechanical solicitation of the interface and has concluded that the material starts to flow from the weld line, leading to the flash formation (Fratini & La Spisa (2011); Schroeder *et al.* (2012); Fratini *et al.* (2012); McAndrew *et al.* (2014, 2015a,b, 2017)). Figure 1.25 depicts both the In-Plane Force (in red) and the Axial shortening (in blue). Schroeder *et al.* (2012) have identified each phase and Phase II is located where the axial shortening starts to increase.

There is no consensus in the literature regarding that transition from one phase to another and the consequences related to numerical implementations. On the one hand, the first approach assumes no penetration of the workpieces and therefore the workpiece contact interface is still distinguishable, and so, one cannot assume that the workpieces have completely bonded. As a consequence, an accurate numerical representation to be used would be either DDB or DRB.

SB models cannot be used based on its assumption as the bonding is not complete. On the other hand, the second approach assumes a complete bonding of the workpiece as an initial condition for the Transition phase, and so, a SB model could be used for simulation. As far as chained simulation is concerned, the approach used to define each phase is not critical as long as the transition between the phases is clear and the numerical model used to comply with the assumptions.
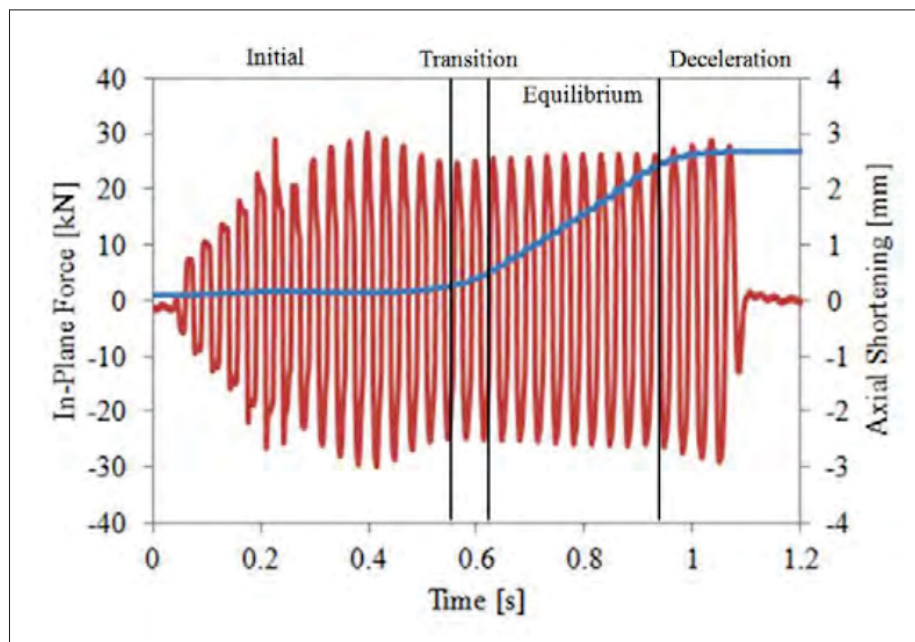
Figure 1.25   In-plane force (red) and upset (blue) for a weld at
medium energy input rate with indicated process phases
Schroeder *et al.* (2012)

1.2.2.4   Post-Processing Phase

Once, the targeted axial shortening has been reached, the weld can be considered as completed and the process enters into its last phase. The post-processing phase has few sub-phases or steps, whose purpose is to align the workpieces and consolidate the weld. First, during the deceleration step, the oscillations stop and the workpieces are quickly aligned (less than 0.1s) to ensure high-quality alignment (Vairis & Frost (1998, 2000); Ceretti *et al.* (2010)). Then,

depending on the material to be welded and the assembly itself, the axial load can either be kept on while the workpiece is cooling down (the cooling step), or the axial load is increased to forge the weld (the forging step). The post-processing phases (forging, heat treatment, etc.) depend on the material and the assembly itself, and so, they are not addressed in this study.

1.2.2.5 Phase Characteristics and Numerical Model Applicability

Figure 1.26 summarizes the applicability of the numerical models on the process phases. Both DDB and DRB can be used to simulate all the process phase either be with a TMA or a HTA approach. Those models can be considered as end-to-end models as they are able to simulate the whole LFW process. However, SB model under a TMA approach cannot be used for Phase I as it assumes that the workpieces have jointed at the end of Phase I. The applicability of the SB model under a HTA approach is still unknown as it has not been mentioned in the literature, yet. The LFW process is characterized by:

- The frictional heat generation and the rapid increase of temperature for Ti-6Al-4V in Phase I. A HTA approach would be more suitable than a TMA approach for computational efficiency.

- The beginning of the material flow in Phase II. A TMA approach may be privileged to simulate this phase.

- The constant axial shortening and a quasi-constant temperature in Phase III. A TMA approach may also be privileged to simulate this phase.
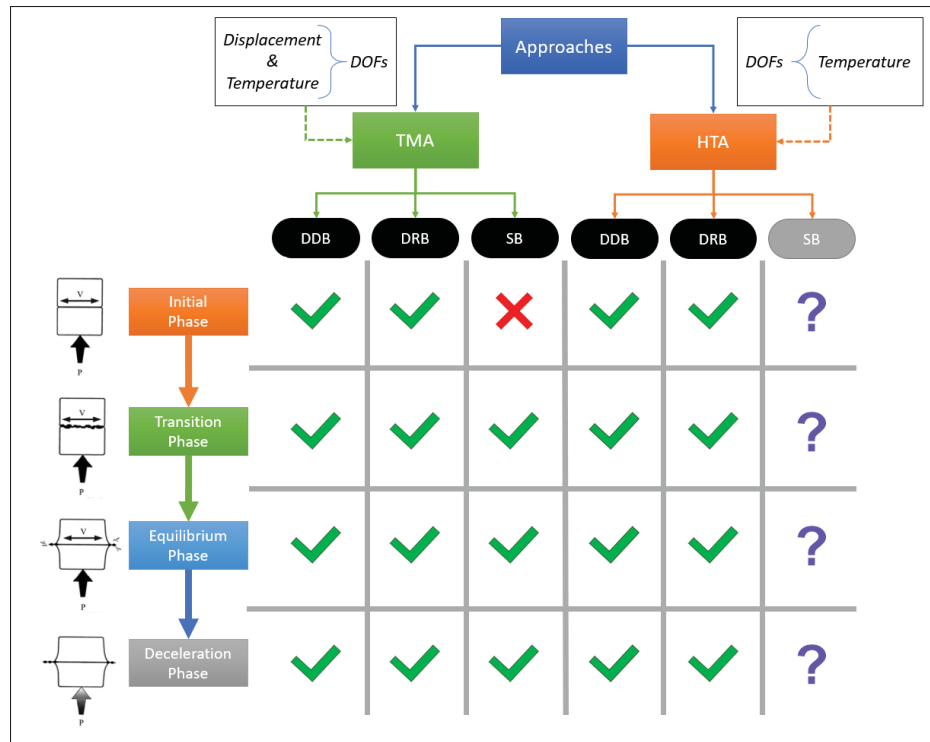
Figure 1.26   Numerical model applicability on the LFW phases

1.3   Research Project

On the basis of the gaps identified in the literature review, this study will focus on:

- The phase transition definition. The latter is not accurately defined in the literature and it makes difficult to discretize accurately each phase for a numerical implementation. Without clear end phase criteria, the simulations may overlap or create a gap in the process simulation. An objective of this study is to define accurately each phase transition based on thermodynamic and mathematical analyses to guarantee a continuous simulation.

- Establishing a chained numerical model to simulate the LFW process. Once the end phase criterion has been defined accurately for each phase, numerical models may be tailored to simulate specific output. In addition, the recent publications have reported efficient approach to simulate the LFW. Therefore, a chained numerical model will combine optimal models to simulate the joining process.

- A first approach to model the microstructure evolution during the LFW. The microstructure transformation during the joint creation will influence the mechanical and fatigue properties of the joint. Therefore, it is crucial from a designer's point of view to predict the microstructure evolution and define the optimal parameters for a given assembly. This study will investigate an approach to simulate the microstructure evolution during the LFW process.

CHAPTER 2

CHAINED NUMERICAL MODEL

In this study, a new numerical approach is developed to study microstructure evolution during the LFW process. This approach follows the phase discretization introduced by Vairis & Frost (1998) and defines end-phase criteria for each phase to guaranty the properties continuity in numerical simulations. Recent published work (Bühr *et al.* (2017)) have shown that specific models such as thermal models are more efficient than oscillatory models. They use the phases main characteristics in the simulation, thereby reducing the model complexity as well as computational cost. Hence, by analyzing each phase according to its governing characteristics, an efficient numerical model could be tailored to it. Under these conditions, each model is computed sequentially, forming a chained simulation. The aggregation of the numerical models will form a chained numerical model that will simulate the entire LFW process from start to end.

The phase discretization approach introduced by Vairis & Frost (1998) provides a clear description of the main characteristics of each phase; however, it is still ambiguous when it comes to transition from one phase to the next. While LFW is a continuous process, for efficient and accurate numerical simulations clear mathematical and physical transition criteria are required for each phase. Once, optimum numerical models are defined, the chained numerical model can be used to study complex aspects such as grain size evolution, or phase transformation during the process. Only pre-and post LFW microstructures are discussed in the literature and the mechanisms influencing microstructure evolution during LFW are not taken into consideration and their impact not quantified. In the present work, the proposed chained numerical model will be used to analyze the LFW of titanium alloy Ti-6Al-4V as extensive experimental data on LFW of this alloy is available in the literature allowing a better validation of the model predictions.

2.1   Material Characteristics

Ti-6Al-4V can be considered as the work horse alloy in the aerospace industry with widespread applications in the turbine engines. The alloy has been one of the first ones used for the manufacturing of Blisks using the LFW technology. For the purpose of the numerical simulation, the material was considered homogeneous, isotropic, and both thermal and mechanical properties were considered temperature-dependent to account for the material softening. Other properties such as the density, the Young's modulus, the Poisson coefficient, the specific heat (Figure 2.1a), the thermal conductivity (Figure 2.1b) and the maximum yield stress (Figure 2.3) were obtained from the literature (Basak *et al.* (2003); Boivineau *et al.* (2006)) and Transvalor Forge® NxT 1.1 (Forge software) library.
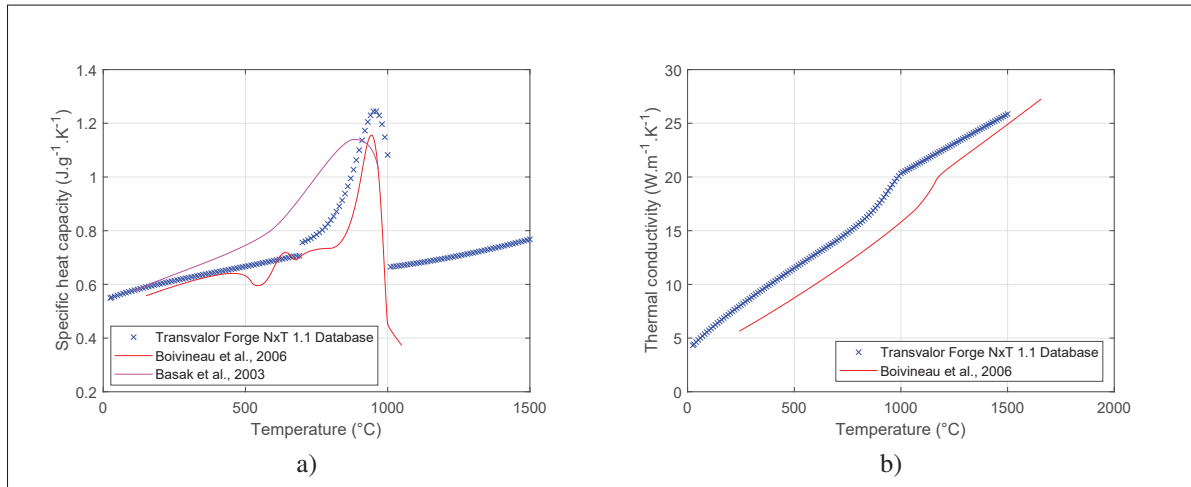
Figure 2.1   Ti-6Al-4V thermal properties as a function of the temperature: a) Specific heat capacity with Boivineau *et al.* (2006) in red, Basak *et al.* (2003) in magenta, and Forge software databases Transvalor (2016) in blue, b) the Thermal conductivity with Boivineau *et al.* (2006) in red and Forge software databases Transvalor (2016) in blue

2.1.1   Microstructural Properties

Ti-6Al-4V is an α-rich, $\alpha + \beta$ alloy (Figure 2.2). The Aluminum stabilizes the close-packed hexagonal α phase, providing strength to the alloy, whereas the Vanadium introduces body centered cubic β-phase into the α matrix, providing ductility to the alloy. $\alpha + \beta$ titanium

alloys are known for their mechanical strength at moderate temperatures (up to 600 °C) thanks to the close-packed hexagonal α phase. As the temperature rises, the α phase is transformed into the β phase and all the α phase is transformed passed the β transus temperature of 980 °C (Wanjara & Jahazi (2005); Dalgaard (2011); Grujicic *et al.* (2012)). The β phase has a body centered cubic lattice which is easier to deform than the close-packed-hexagonal lattice of the α phase, therefore, most of the deformation processing of $\alpha + \beta$ titanium alloys is generally conducted in the β phase or near the β transus.
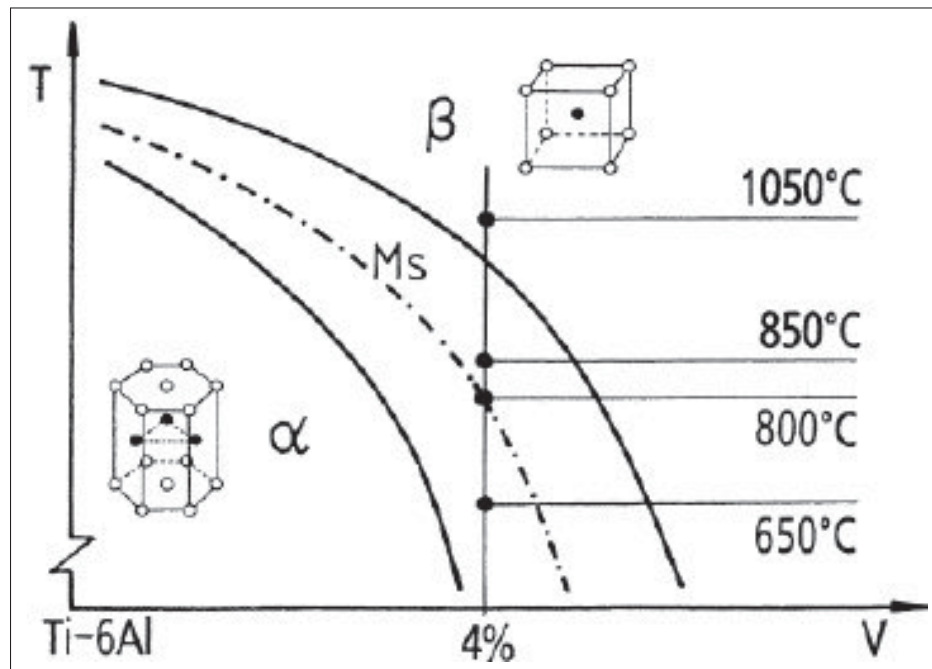
Figure 2.2   Ti-6Al-4Vphase diagram (Ducato *et al.* (2013))

Experimental studies on microstructure evolution during the LFW process are based on comparing samples before and after welding where major microstructural changes have been observed (McAndrew *et al.* (2017); Wanjara & Jahazi (2005); Dalgaard (2011)). However, very little or no data is available on the impact of deformation parameters (strain, strain rate, and temperature) on the microstructure (McAndrew *et al.* (2017)). In the present work, it is assumed that there is no dynamic recrystallization and hence, no grain refinement occurs during Phase I. This assumption is based on the estimated temperature and strain rate during

this phase: both parameters are too low to produce DRX (Wanjara & Jahazi (2005)). Therefore, no DRXed grains are expected to be present at the start of the Friction phase. Furthermore, based on the β transus temperature, it is assumed that the weld line is only composed of β phase at the beginning of the Friction phase (Wanjara & Jahazi (2005); Grujicic *et al.* (2012)).

2.1.2 Mechanical Properties

Figure 2.3 depicts the maximum yield stress according to the temperature and the strain rate from the Forge software database (Transvalor (2016)). At room temperature, the maximum yield stress is between 1350 MPa and 1650 MPa, with respect to the strain rate. Then, as the temperature increases, the Ti-6Al-4V mechanical strength decreases to 950 MPa at 750 °C. At that point, the Ti-6Al-4V microstructure begins to change from the α phase to the β phase which is softer than the α phase as mentioned earlier (Wanjara & Jahazi (2005); Dalgaard (2011)). Then, above 1000 °C, the Ti-6Al-4V has a lower maximum yield stress (under 200 MPa) due to the dominance of the β phase.

The LFW can be considered as a hot-forming process as it brings the weld line to a working temperature above the β transus temperature. The visco-plastic layer formed at the weld line is more ductile than the parent material, and so, it can undergo larger deformation before necking. The residual pores between the upper and lower workpieces are closed if the amount of axial shortening is greater than 1.5 mm (Wanjara & Jahazi (2005)). In addition, the working temperature is higher than the recrystallization temperature, so restoration processes occur during the workpieces bonding (Wanjara & Jahazi (2005)). The WCZ shows a transformed microstructure at the end of the process and the mechanical properties altered that the fracture usually happens in the parent material (Dalgaard (2011); McAndrew *et al.* (2017)). Finally, the rubbing motion removes the surface contaminant and combines the workpieces by extruding the visco-plastic layer thanks to its high ductility and the axial pressure.
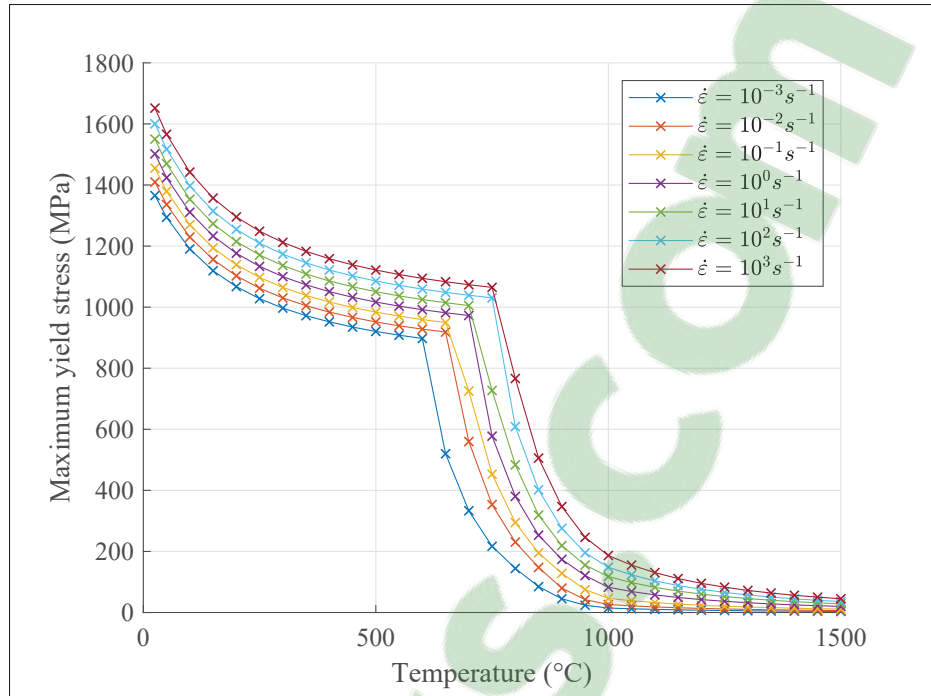
Figure 2.3   Ti-6Al-4V Maximum yield stress as a function of the
temperature and the strain rate from the Forge software database
Transvalor (2016)

2.2   Process Discretization for Numerical Implementation

LFW process is complex to apprehend and to model as it is a fully coupled thermo-mechanical process. Vairis & Frost (1998) have broken down the process into four phases and identified their characteristics. The latter can be used to define specific models which may be more accurate than a general one. In addition, it reduces the simulation complexity as only a specific physic is applied on targeted zones whereas a general model may require more computational resources. Dividing to model allows to approach each phase by their impact on the process and allows process-phase optimization.

This study is focusing on the LFW from Phase I start to Phase III end. Phases I to III correspond to characteristic periods of the process (Vairis & Frost (1998)) but they are difficult to separate as the LFW is a continuous process. For this reason, there is no consensus in the literature regarding the phase transitions as it is easier to describe characteristic periods than to identify

their transition criteria. However, numerical simulations require to dissociate each phase to provide an accurate numerical model.

2.2.1 Thermo-mechanical and Thermal Thresholds

According to the literature (Paragraph 1.2.2.1), Phase I can be considered completed once the weld line has become visco-plastic. At that time, the material at the weld line starts to flow, leading to the flash formation and the beginning of the axial shortening. According to the temperature measurements and simulations done by McAndrew *et al.* (2014, 2015b,a, 2016), the edges are cooler than the weld line's center. Thus, it can be expected that the weld line center reaches first the visco-plastic state followed by the edge zones (Figure 2.3) resulting in the formation of the flash. The transition between Phases I and II can, therefore, be defined when the equivalent stress is equal to the maximum yield stress at the edges ($\pm \frac{W}{2}$) of the workpieces. Henceforth, the criterion for the end of Phase I can be formulated as:

$$\sigma_{eq}\left(\pm \frac{W}{2}, T_{th} \right) = \sigma_y \left(T_{th}, \bar{\varepsilon}, \dot{\bar{\varepsilon}} \right) \tag{2.1}$$

with ($\sigma_y \left(T_{th}, \bar{\varepsilon}, \dot{\bar{\varepsilon}} \right)$) the yield stress and ($\sigma_{eq} \left(\pm \frac{W}{2}, T_{th} \right)$) the equivalent Von Mises stress at the workpiece edges for the threshold temperature (T_{th}). The latter has softened significantly the weld line material that has become visco-plastic and behaves like a viscous fluid. Henceforth, as a viscous fluid which can no longer sustain its loading, it flows, extruding the material from the welding line and initiating the axial shortening. Therefore, the yield stress can be used as a thermo-mechanical threshold, according to the strain ($\bar{\varepsilon}$), strain rate ($\dot{\bar{\varepsilon}}$) and the temperature (T) experienced at the weld line edges to define the end of Phase I.

Based on the above definition, a TMA approach could be used to model Phase I and stop when the equivalent Von Mises stress reaches the yield stress. Such approach has to compute the thermo-mechanical threshold at each iteration and determine the time when the simulation shall stop. However, this requires significant computational resources and long-run time.

Recent publications (Bühr *et al.* (2017)), have shown that HTA approach is quicker and more efficient to compute Phase I. But, no equivalence has been established between TMA and HTA approaches, and so, no end-phase criterion has been provided.

In the present work, in order to optimize the chained numerical model, Phase I will be described by a HTA approach, and a thermal end-phase criterion will be established allowing for the transition between TMA and HTA approaches. McAndrew *et al.* (2014) reported that for their study the temperature at the end of Phase I was $1000\,°C$ in average across the weld line. According to Figure 2.3, it can be expected that:

$$\forall (T,\dot{\varepsilon}) \in [1000\,°C, 1500\,°C] \times [10^{-3}\,s^{-1}, 10^{3}\,s^{-1}], \sigma_y(T,\dot{\varepsilon}) \leq 200\,MPa \qquad (2.2)$$

The range of process parameters for the contact pressure is between $40\,MPa$ and $125\,MPa$. The shearing stress, influenced by the oscillation amplitude, increases from the beginning of Phase I as the contact condition between the two workpieces evolves from a dry to a stick-slip contact. It reaches a maximum and then decreases as the weld line is becoming a visco-plastic fluid and cannot transmit any tangential loading. Thus, the equivalent stress can rapidly reach the $200\,MPa$ limit, so a conjecture in HTA approach would be:

$$\forall T\left(\pm\frac{W}{2}\right) \geq 1000\,°C \Rightarrow \sigma_{eq}\left(\pm\frac{W}{2}, T\right) = \sigma_y\left(T, \bar{\varepsilon}, \dot{\bar{\varepsilon}}\right) \qquad (2.3)$$

Therefore, the end-phase criterion for the HTA approach is:

$$T\left(\pm\frac{W}{2}\right) = T_{th} = 1000\,°C \qquad (2.4)$$

2.2.2 Friction Phase

To guarantee the process continuity, Phase II and III are grouped into the Friction phase. Both phases will be identified in the simulation post-processing analysis. Two approaches can be followed to separate Phase II from Phase III:

1. Despite the lack of criterion provided in their studies, Vairis & Frost (2000) and Ceretti *et al.* (2010) have considered that Phase III begins when the axial shortening becomes recordable by a LVDT. Henceforth, Phase II can be seen as an intermediate step between Phase I and Phase III.

2. Phase III begins when the axial shortening rate becomes constant. Therefore, Phase III is the steady state of the axial shortening and Phase II is the transient state.

According to the phase definition Vairis & Frost (1998), Phase III is the self-regulating state of the process. In the present work, the second approach is used because it allows to dissociate the transient state and the steady state of the axial shortening. So, each phase can be simulated, studied, and numerically optimized based on its main characteristics.

Therefore the condition to differentiate Phase III from Phase II is given by:

$$\ddot{s}(t_r) = 0 \tag{2.5}$$

with (t_r) the time when the transition occurs and $(s(t))$ the axial shortening.

The most important characteristic of Phase III is the constant axial shortening rate (v). On this basis, the axial shortening evolution during this phase is given by:

$$\forall t \in \text{Phase III}, s_{III}(t) = v\left(t - t_{eq}\right) + s_{max} \tag{2.6}$$

with (s_{III}) the axial shortening during Phase III, (t_{eq}, s_{max}) the time and the axial shortening at the end of this phase, respectively.

The Phase II is characterized by the initiation of the axial shortening (i.e increases from 0 to a constant rate v). In addition, the axial shortening is continuously changing with time. Thus, the axial shortening has the following constraints during Phase II

$$s_{II}(0) = s(0) \tag{2.7a}$$

$$s_{II}(t_r) = s_{II}(t_r) \tag{2.7b}$$

$$\dot{s}_{II}(0) = 0 \tag{2.7c}$$

$$\dot{s}_{II}(t_r) = v \tag{2.7d}$$

with (t_r) the transition time between Phases II and III, (s_{II}) the axial shortening during Phase II and (s) the axial shortening during all the process. The smallest order of a polynomial function which can satisfy these constraints is a 3rd degree polynomial function:

$$\forall t \in \text{Phase II}, s_{II}(t) = at^3 + bt^2 + ct + d \tag{2.8}$$

So, to characterize Phases II and III, the linear system composed of Equations 2.8 and 2.6 and constrained by Equations 2.7 and 2.5 must be solved and can be resumed to the following equation:

$$4t_r \left(s(t_r) - s_{max}\right) - 6 \left(s(t_r) - s(0)\right) \left(t_r - t_{eq}\right) = 0 \mid t_r \in]0, t_{eq}[\tag{2.9}$$

The latter can be solved by dichotomy to find the phase change t_r, identifying Phases II-III, and then, the axial shortening rate. The dichotomy method may not be the fastest zero-finding method but Equation 2.9 requires to know the real axial shortening function. Geng *et al.* (2019a) have shown the complexity of this function: continuous and oscillating. It makes

faster methods such as Newton Raphson method, difficult to use in this case as the derivative of the real function induces strong variation due to the oscillations.

2.3   Chained Numerical Model Description

The chained numerical model is composed of two thermo-mechanical models:

1. A DDB model following a stationary TMA approach (Figure 2.4) for Phase I simulation.
2. A SB model to simulate the flash formation accurately during the Friction phase.

This proposed chained numerical approach focuses on the phase characteristics and uses tailored numerical models for each phase. End-phase criteria (Equations 2.1 & 2.5) have been introduced to sequentially run the simulation and provide a Phase I-to-III optimized simulation of the LFW.

2.3.1   Initial Phase Models

The Initial phase is simulated with ABAQUS/STANDARD 6.13 (ABAQUS software). As discussed above, one of the goals of this study is to establish an end-phase criterion for HTA approach, to allow the use of thermal models in chained simulation. So, to study the conjecture made in Equation 2.3, two approaches are considered using the same DDB model:

1. A TMA approach is used to establish the end-phase criteria (Equation 2.1) for the oscillatory DDB models. This model is referred as the Oscillation Model (OM) in this study (Figure 2.4).
2. A stationary TMA approach, combining the general TMA's DOF and the stationary assumption made in the Heat Transfer Analysis (HTA) approach, is used to establish the equivalence with the first one. This model is referred as the Thermal Model (TM) in this study (Figure 2.4).
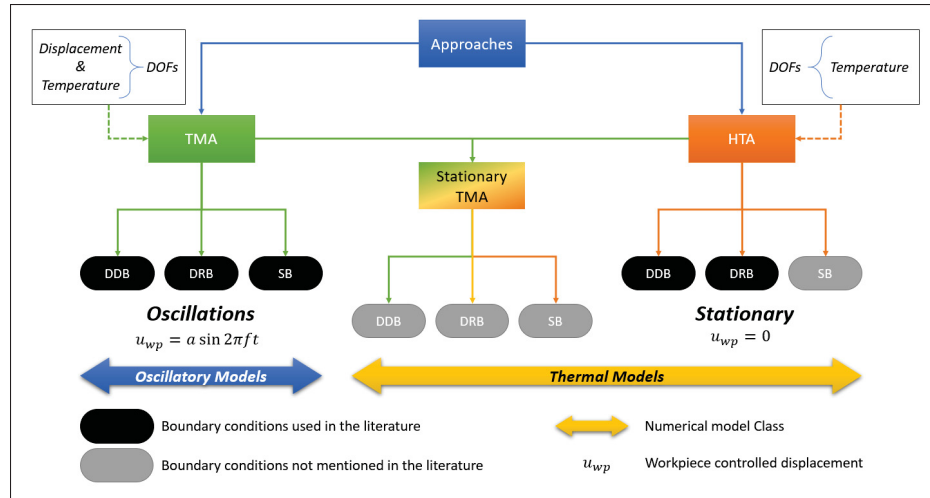
Figure 2.4   Combine approach to simulate LFW

2.3.1.1   Boundary Conditions and Meshing

Figure 2.5 shows the model geometry and meshing base line for both approaches. It is a 2D model under plain strain assumption to comply with Forge software conditions. It is composed of two deformable workpieces of 26 mm width, 26 mm height and 1 mm thickness. The HAZ spreads up to 8 mm on either side of the weld line (McAndrew *et al.* (2014)) then reach the parent material where no plastic deformation occurs throughout the LFW process. A single bias mesh size from 0.2 mm at the weld line to 0.5 mm at the HAZ edge is used in agreement with Turner *et al.* (2011) mesh sensitivity study (Figure 1.22). The parent material was meshed with a single bias mesh size from 0.5 mm at the HAZ edge to 2.5 mm at the far end of the sample.

Simulations are set as a transient coupled time displacement, fully coupled thermomechanical analysis. The latter needs the use of elements with both temperature and displacement DOF. Thus, in this work, CPE8RT (8-node biquadratic displacement, bilinear temperature, reduced integration) quad elements are employed from the ABAQUS software library. In this way, the 2D model in-plane-stress condition represents a slice of the sample. Each part has 3945 nodes and 1352 elements. The initial temperature for both parts is predefined in ABAQUS at 27 °C representing room temperature.
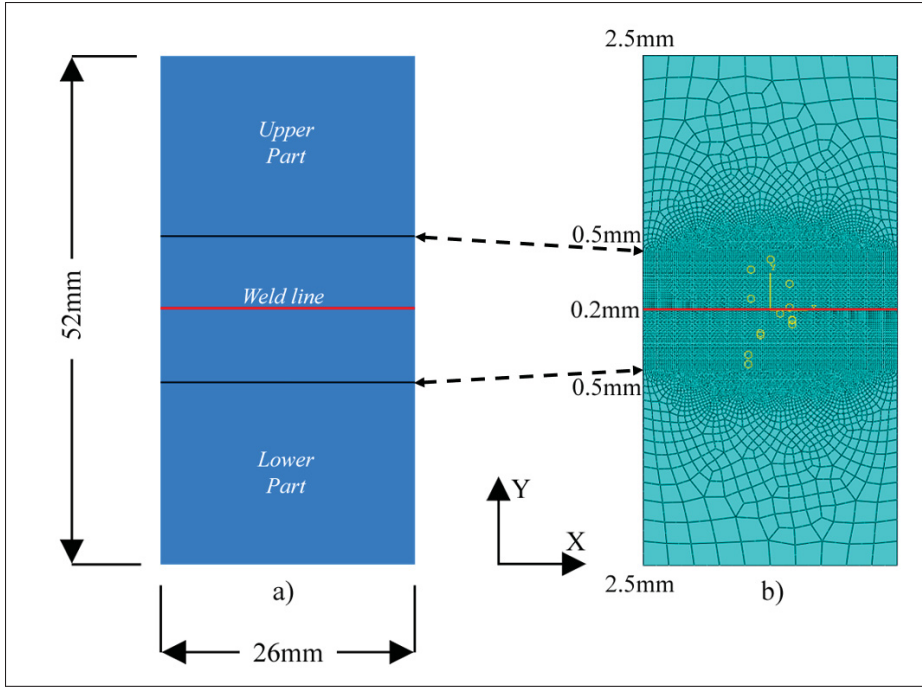
Figure 2.5   Model geometry and mesh size: a) model dimension
and b) mesh size in different zones

Figure 2.6 shows the boundary conditions set for both models. The upper workpiece is constrained in x-displacement along the side faces of the parent material. In addition, the contact pressure is applied at the top of this part, and the gravity is not considered in both models. Moreover, the heat flux coefficient at the edges of the HAZ is set to $-10\,\text{W}\cdot\text{m}^{-2}$ as proposed by McAndrew *et al.* (2014, 2016). The negative sign of the heat flux value represents the heat loss by the heat exchange between the HAZ and the ambient atmosphere. The thermal conductivity between the dies was set to $2\,\text{kW}\cdot\text{m}^{-2}\cdot\text{K}^{-1}$ considering them as heat sinks.

For the OM model, a time-dependent displacement is defined as a sinusoidal function ($u\,(x) = a\sin\,(2\pi\text{ft})$ - Equation 1.1) on the lower part along the two side faces of the parent material in the x-direction. Whereas, the lower part is fixed in the TM model and a surface heat flow is added at the contact line between both parts to account for the energy released by the oscillations.
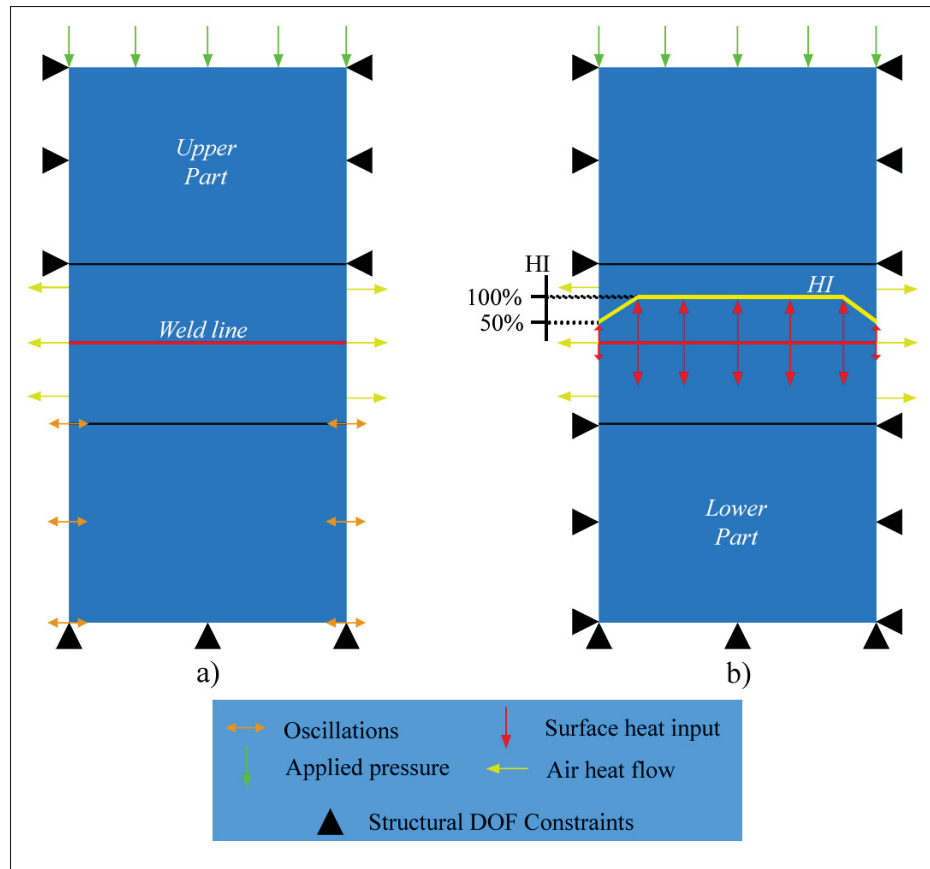
Figure 2.6   Numerical model boundary conditions: a) oscillation
model, b) thermal model.

2.3.1.2   Contact Condition

As the OM model reproduces the oscillations, it requires the contact condition between the
two workpieces which can be implemented by various models, according to the literature
(Figure 1.3). The friction coefficient is a function of several factors such as interface temper-
ature, contact pressure, surface topology, etc. But, in this study, the friction coefficient is only
considered temperature dependent as more complex model are not available and will increase
the computational time. A penalty method based on Grujicic *et al.* (2012) study (Figure 2.7) is
used and modified to account for the viscoplastic friction at high temperature (above 600 °C)
as reported by Maio *et al.* (2016) and Vairis & Christakis (2007). Regarding numerical imple-
mentation, "Inelastic Heat Fraction" for the material and "Gap Heat Generation" are defined:

54

considering that 90 % of the friction energy (McAndrew *et al.* (2015b)) is converted to heat and used as a heat source, then, 50 % of the frictional heat is assigned to each deformable part (i.e. equal heat distribution).
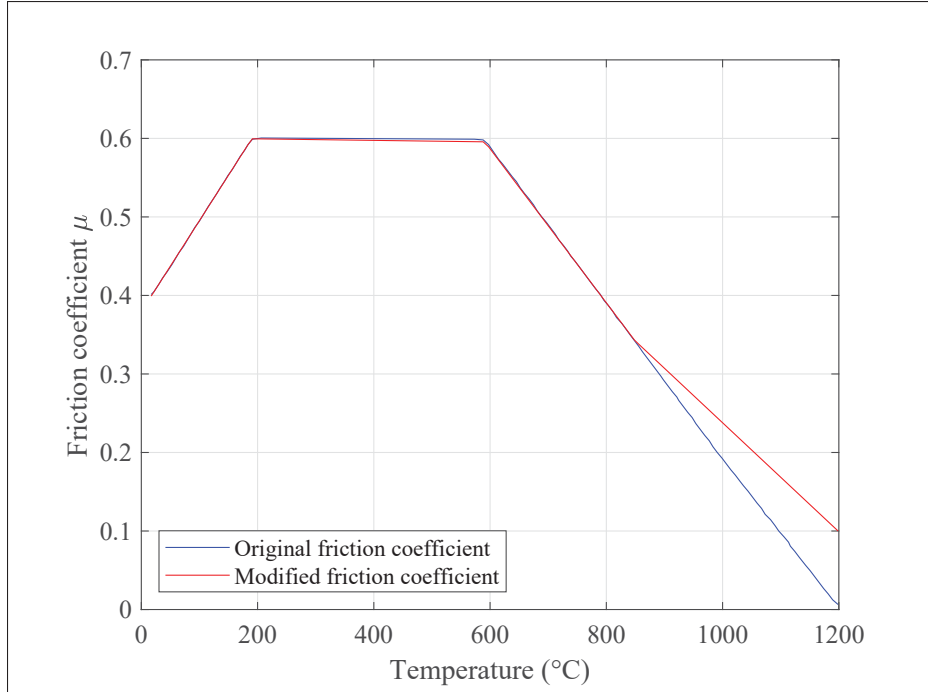
Figure 2.7   Temperature-dependent friction coefficient, $\mu\left(T\right)$, for Ti-6Al-4V (Grujicic *et al.* (2012)) in blue, modified friction coefficient in red

2.3.1.3   Subroutine

For the TM model, the oscillations are replaced by their equivalent average heat input ($\bar{Q}_{total} = 4\mu F_n a f$ - Equation 1.9) and the lower part is then fixed in both directions. The contact between the two workpieces is considered to be completely established even though the literature suggested that the contact gradually increased during Phase I up to a near complete contact at the end of Phase I. However, since there is no publication concerning the surface roughness and thus the initial contact area. The end phase is not defined prior to the calculation but by

the thermo-mechanical threshold, therefore, it is not yet possible to establish the contact area evolution as the initial area and the end phase are unknown.

A user-defined ABAQUS/DEFLUX subroutine computes the heat flow at the interface considering the same friction coefficient previously defined for the OM model (Figure 2.7). A non-uniform heat flux is applied along the weld interface to compensate reciprocation movement of the lower part relative to the upper one in the thermal model. Indeed, the oscillating motion causes a portion of the lower and upper part (over an amplitude length at both ends) to experience more heat transfer towards the environment thereby resulting locally in a slight decrease in temperature (McAndrew *et al.* (2014, 2015b, 2016)). Therefore, the heat flux distribution is linearly reduced from 100 % to 50 % (Jedrasiak *et al.* (2018)) along the weld interface over a length a (the amplitude) from each side of the lower and upper parts, as shown in Figures 2.6 and 2.8

$$\Xi(x) = \begin{cases} 1 & \forall |x| \in [0, \frac{w}{2} - a] \\ \frac{1}{2a} \left(\frac{w}{2} - a - |x| \right) + 1 & \forall |x| \in [\frac{w}{2} - a, \frac{w}{2}] \end{cases} \tag{2.10}$$

So the surface heat flow computed by the subroutine is:

$$HI(x) = 4\mu a f p_n \Xi(x) \tag{2.11}$$

where (μ) is the Coulomb's friction coefficient, (a), (f) and (p_n) are respectively the amplitude, oscillation frequency and contact pressure.

56
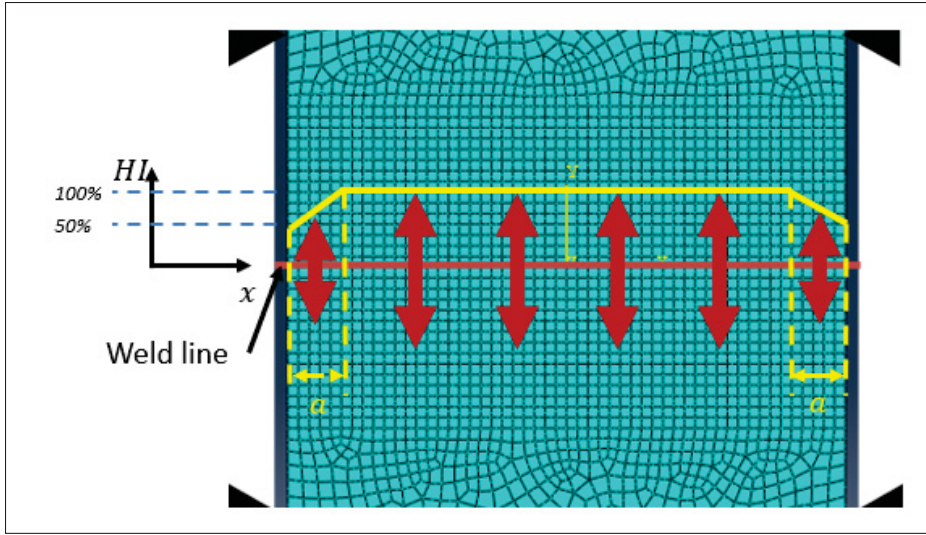
Figure 2.8   Surface heat flow according to Equation 2.11

2.3.2   Friction Phase Model

The purpose of this model is to provide a first numerical approach to study the microstructural changes during the flash extrusion. It is simulated by a SB model with Transvalor Forge® NxT 1.1 (Forge software) for its ability to simulate forging process and large deformation. Once Phase I is completed, the simulation switches from a DDB model to a SB model, assuming that the two workpieces have virtually jointed.

2.3.2.1   Boundary Conditions and Meshing

As previously established for Phase I models, the Friction phase model is a 2D model under plain strain assumption but composed of one deformable workpiece of 52 mm width, 26 mm height and 1 mm thickness (Figure 2.9a). As the workpiece undergoes severe deformation at the weld line, a finer mesh of 0.2 mm mesh size over 3.25 mm on either side of it. Then, the mesh size increases to 0.35 mm and to 0.5 mm at the end if the HAZ, 8 mm on either side of the weld line. Finally, the parent material is meshed with a 1 mm mesh size since no change is occurring in this zone (Figure 2.9b). The model is composed of 7293 nodes and 14179 elements each with 4 nodes and both temperature and displacement DOF. The temperature

distribution at the end of Phase I is mapped on the new single workpiece mesh as the initial temperature distribution (see Appendix I).

The SB model used the same boundary conditions as established for the OM and TM models, at the difference that, the dies are present as a Forge software characteristic (Figure 2.9a). Therefore, the lower dies, holding the workpiece's lower part (i.e, bilateral sticking condition), provide the oscillating motion as per Equation 1.1 and the upper dies, blocking the workpiece's upper part in the x-direction (i.e, $u_x = 0$), are fixed and allow displacement in the y-direction to account for the axial shortening.
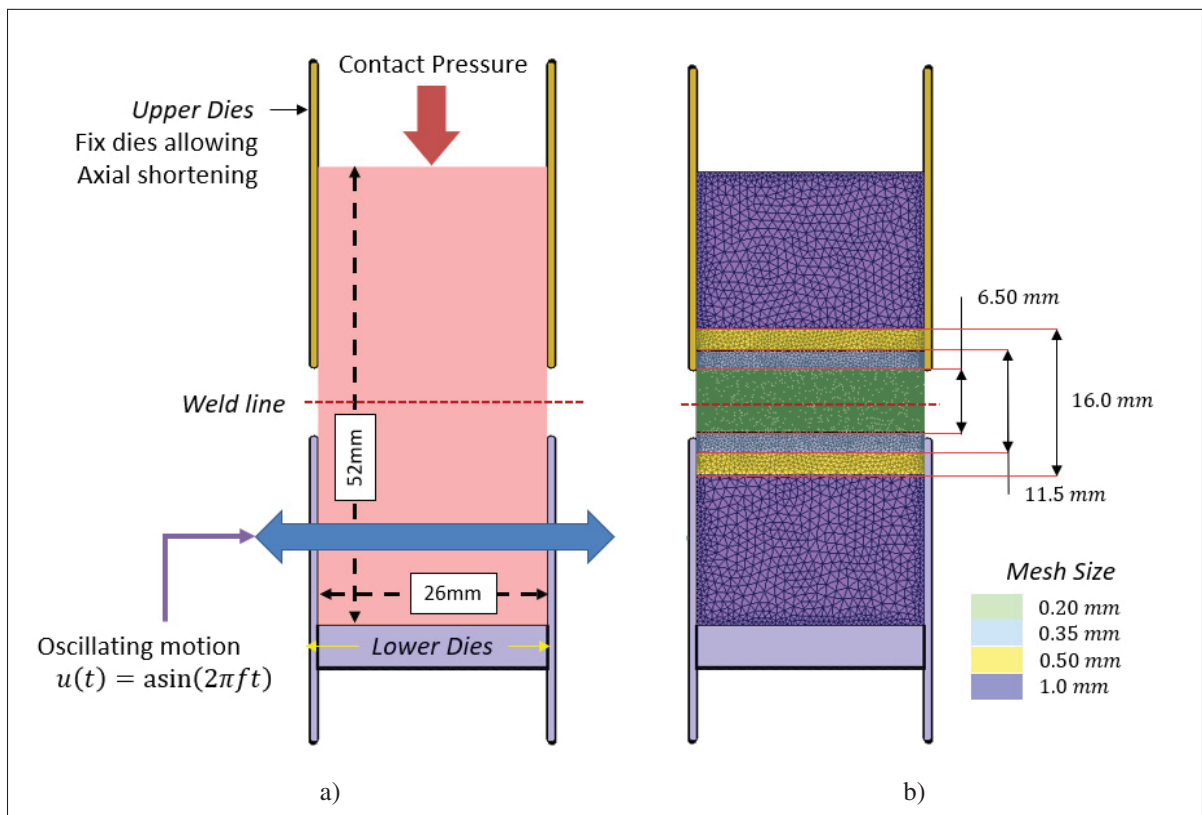
Figure 2.9 Friction phase Single Body (SB) model: a) boundary conditions, b) mesh

2.3.2.2 Microstructure Evolution Model

The microstructure examinations of linear friction welded samples have shown the occurrence of significant grain refinement, mainly due to DRX at the weld interface (Wanjara & Jahazi (2005); Dalgaard (2011)). This grain refinement impacts significantly the joint mechanical properties McAndrew *et al.* (2017). Thus, it is crucial to predict the evolution of the microstructure during the LFW process, and especially dynamic recrystallization from a mechanical design point of view. The recrystallization kinetics being dependent on temperature and deformation, both of which are related to the LFW process parameters such as frequency, amplitude, and applied pressure (Montheillet & Jonas (2009)); therefore, the kinetics of dynamic recrystallization need to be determined. The application of the Johnson, Mehl, Avrami, Kolmogorov (JMAK) equation provides a first approximation of the evaluation of the recrystallization kinetics during LFW and the obtained results could be correlated with the grain size.

Many authors have used JMAK to model DRX during hot compression (Tamirisakandala *et al.* (2003); Honarmandi & Aghaie-Khafri (2013)). However, the strain and strain rates encountered during LFW (McAndrew *et al.* (2015a)) are expected to be much higher than those in hot compression and therefore it could be expected that the kinetics of microstructure evolution would be different. However, considering the lack of numerical models on deformation parameters during LFW, using JMAK approach could be a starting step. The JMAK equation is defined as:

$$X_{\text{drx}} = 1 - \exp\left(-\kappa\left(\frac{\bar{\varepsilon} - \varepsilon_c}{\varepsilon_{.5}}\right)^{\beta}\right) \tag{2.12}$$

In the above equation X_{drx} represents the recrystallized volume fraction, $\bar{\varepsilon}, \varepsilon_c, \varepsilon_{.5}$ respectively the equivalent, critical, and half-recrystallized strain, and κ and β dimensionless parameters. Due to the phenomenological nature of the JMAK equation, it is highly material dependent. Furthermore, the values of the variables depend on the testing temperature and strain rate

ranges. In the present work, the data reported by Quan on hot compression of Ti-6Al-4V (Quan *et al.* (2015)) are used in Equation 2.12. The latter can be further studied in terms of grain size (Montheillet & Jonas (2009)).

Besides the constraints and the applicability of the JMAK equation, the latter informs on the state of the microstructure: where microstructural changes occur and in which extent it affects the microstructure. So, an indicator can count how many time a region undergoes a complete dynamic recrystallization set by:

$$X_{DRX} \geq 0.99 \tag{2.13}$$

Indeed, once the recrystallized volume fraction has reached that threshold, the material is considered in an annealed state and the X_{drx} is reset to 0, thereby creating a cycle. That indicator would inform on the likelihood of microstructural changes by dynamic recrystallization. A new subroutine called DRX cycles is developed to implement it in Forge software FEM code.

CHAPTER 3

LFW CHAINED SIMULATION APPLIED TO A TI-6AL-4V ALLOY

The established LFW model is applied on Ti-6Al-4V alloy with the following objectives:

- Establish numerical transitions from one phase to the next by providing end phase criteria for both TMA and HTA approaches.
- Improve the computational efficiency with a new stationary TMA approach to simulate Phase I for the chained simulation.
- Study the microstructure evolution during Phases II-III of the process

In addition to those objectives, the temperature evolution and distribution results will be examined to estimate the accuracy of the chained simulation model.

3.1   End Phase Criteria for Thermo-Mechanical and Heat Transfer Analysis Approaches

This study has established end phase criteria to accurately discretize the LFW process for numerical simulations. First, a thermo-mechanical threshold was defined (Equation 2.1) as a stop condition for Phase I for a TMA approach. However, to improve the computational efficiency of the chained numerical model, a stationary TMA approach was chosen to render Phase I. Henceforth, a conjecture was made for a thermal threshold (Equation 2.4) as an equivalent to the thermo-mechanical threshold. Second, both Phase II and Phase III were simulated together under Phases II-III to guaranty process properties continuity. The phases were identified during the results analysis according to their main characteristics (Equations 2.6& 2.8). It allowed identifying the transient and steady state of the axial shortening correctly.

3.1.1   Thermo-Mechanical and Thermal Thresholds of the Initial Phase

The process parameter set chosen for this study was: $a = 2.7\,\text{mm}, f = 50\,\text{Hz}, p = 90\,\text{MPa}$ (Bühr *et al.* (2017)). First, Figure 3.1 shows that the thermo-mechanical thresholds at the center and the edges drop rapidly as the temperature increases. The equivalent stress increases linearly

at the beginning as the pieces are brought together gradually. Then, it reaches a quasi-steady state as the process parameters are constant during the phase. As expected, the weld line center reaches first its mechanical threshold at 0.27 s with a temperature of 911.3 °C (Figure 3.1a). The center has become visco-plastic and is ready to be expelled as it can no longer sustain the process loading. However, at that time, the edges did not reach their thermo-mechanical threshold yet, therefore, they sustain the process loading and retain the viscous center material.

So far in the process, the strain rate computed by simulation at the weld line, is between $0.015\,\mathrm{s}^{-1}$ at the weld line center and $0.5\,\mathrm{s}^{-1}$ at the edges. Vairis & Frost (1998) have published an analytic strain rate based on the process parameters:

$$\dot{\varepsilon} = \frac{af}{l} \tag{3.1}$$

with (a) the oscillations amplitude, (f) the ossification frequency, and (l) the length of the specimen. In this case, the analytic strain rate predicted by Vairis's formula is $\dot{\varepsilon} = 5.19\,\mathrm{s}^{-1}$. The computed strain rate is below Vairis's prediction, but Vairis model does not take into account the weld line state: the edges are experiencing stick-slip friction (Vairis & Christakis (2007)) and undergo large deformation. Whereas, the center experiences a visco-plastic deformation, constrained by the edges which are still supporting the process loading and preventing the weld line to collapse and flow. McAndrew *et al.* (2017) have reported strain rates up to $2500\,\mathrm{s}^{-1}$ during Phase III which can be related to the material stirring and extrusion by the oscillations and the axial pressure. It explains the low strain rate prediction at this time of the process compared to the strain rate reported in the literature.
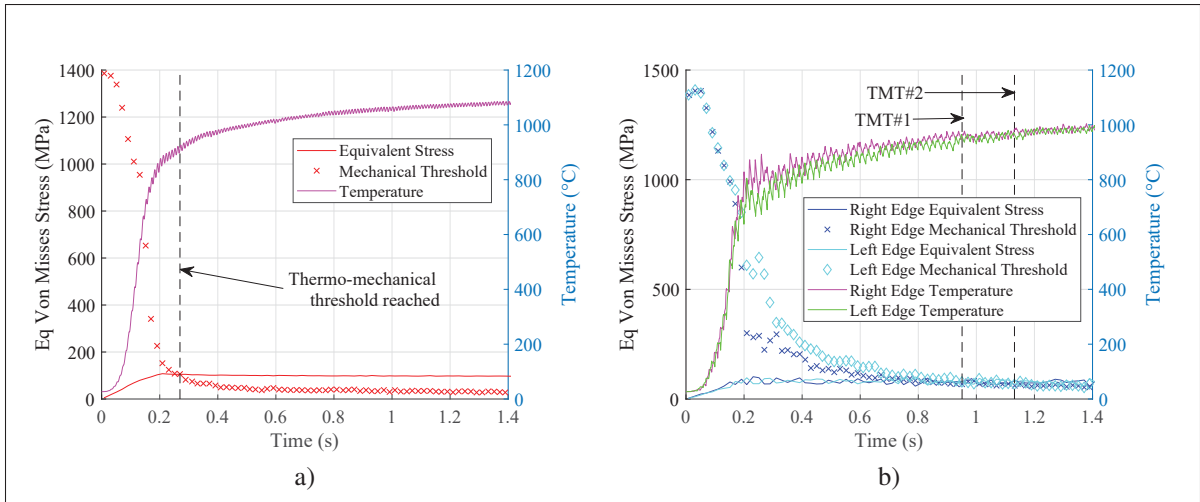
Figure 3.1   Thermo-Mechanical Threshold (TMT) evolution through the Phase I with the following process parameters $a = 2.7\,\text{mm}, f = 50\,\text{Hz}, p = 90\,\text{MPa}$: a) Weld line center, b) Left and right edges

As the temperature spreads out to the edges (Figure 3.1b), the latter soften and reach their thermo-mechanical threshold. At 0.95 s, the edges have both reached once their threshold (TMT#1), but due to the oscillations and the loss to the environment, they regain strength as they cool down temporally. But the temperature keeps increasing despite the losses and the equivalent stress at the edges becomes equal to the thermo-mechanical threshold. At 1.13 s, the equivalent stress is equal to the thermo-mechanical threshold for both edges (TMT#2). Therefore, the edges can no longer support the process loading and the visco-plastic layer is able to flow, ending Phase I and beginning Phase II.

At that time the edges are at 975 °C and the weld line center at 1069 °C. This result agrees with McAndrew *et al.* (2014) study, reporting an average temperature of 1000 °C at the weld line near the end of the initial phase for a Ti-6Al-4V alloy. These results agree with the thermal model assumption that Phase I can be modeled only by thermal analysis and the end criterion for this model is the edge's temperature reaching 975 °C.

3.1.2 Friction Phase Characteristics

Figure 3.2 shows the evolution of the axial shortening from the beginning of Phase II until it reaches its target. According to Equation 2.9, Phase II ends at 0.22 s. At that time, the axial shortening acceleration is 4.18×10^{-07} m·s^{-2}. It validates Equation 2.5 ($\ddot{s}(t_r) = 0$) with a negligible error and supports that the axial shortening has reached its steady state and its constant velocity is 5.93 m·s^{-1}. The polynomial fit suggested (Equation 2.8) for the axial shortening evolution, showed a good agreement with the predicted results ($R^2 = 0.9944$).

After 0.22 s, the process enters in Phase III. The linear axial shortening evolution agrees with the numerical prediction (Equation 2.6) with a determination coefficient of $R^2 = 0.9993$. Over-all, the piece-wise function used to approach the axial shortening shows substantial agreement with the numerical results during the Friction Phase (Phases II-III).
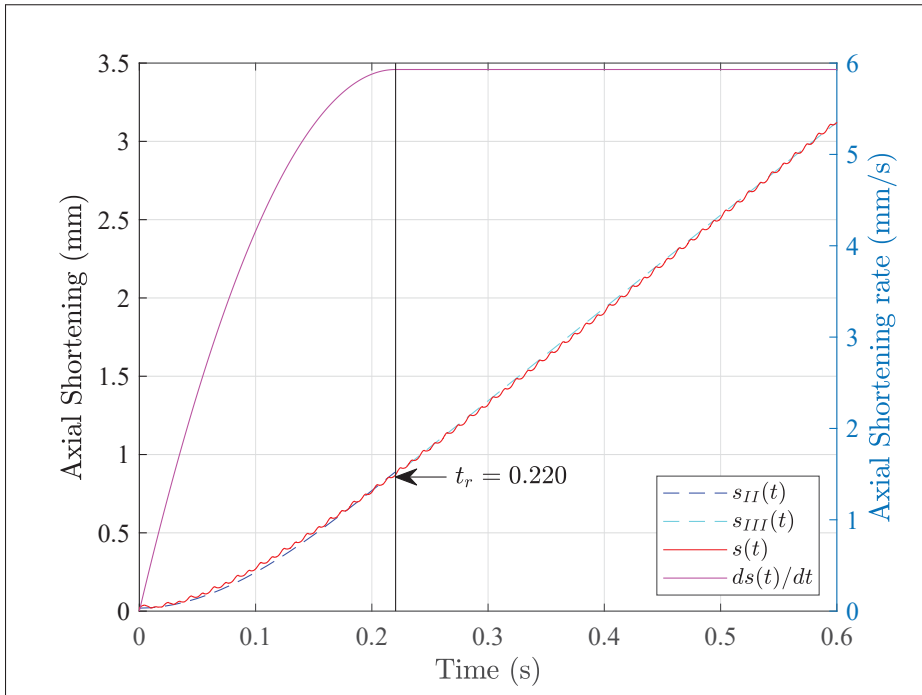
Figure 3.2   Axial shortening analysis during the Friction phase
with accurate transition between Phases II and III: s_{II} and s_{III}
linear regression fit of Phases II and III respectively and s the
predicted axial shortening

The axial shortening rate (v) obtained by Equation 2.6 is between $2.15\,\text{mm·s}^{-1}$ and $5.93\,\text{mm·s}^{-1}$ for the simulations #26 and #27, respectively (Table 3.1). No direct correlation can be made between the process parameters and the axial shortening rate, except that, the simulation #26 has a lower rubbing velocity ($120\,\text{mm·s}^{-1}$) than the simulation #27 ($540\,\text{mm·s}^{-1}$). A stronger rubbing motion is more favorable to material removal as it pushes the material out from the workpiece. However, for an identical rubbing velocity ($540\,\text{mm·s}^{-1}$), the axial pressure influences the axial shortening rate e.g simulation #27 ($5.93\,\text{mm·s}^{-1}$) and #29 ($4.39\,\text{mm·s}^{-1}$). A higher axial pressure ($125\,\text{MPa} \geq 40.0\,\text{MPa}$) adds more constraints to squeeze the visco-plastic layer and helps the oscillations to remove it.

Table 3.1 Axial shortening rate v according to the
process parameters ordered by axial shortening rate

Simulation	Amplitude	Frequency	Axial Pressure	Shear Stress τ	Axial Shortening rate v
#26	1.50 mm	20.0 Hz	125 MPa	60.7 MPa	$2.15\,\text{mm·s}^{-1}$
#28	2.00 mm	30.0 Hz	40.0 MPa	39.0 MPa	$2.62\,\text{mm·s}^{-1}$
#29	2.70 mm	50.0 Hz	40.0 MPa	34.9 MPa	$4.39\,\text{mm·s}^{-1}$
#27	2.70 mm	50.0 Hz	125 MPa	51.8 MPa	$5.93\,\text{mm·s}^{-1}$

Turner *et al.* (2011) have shown a linear relationship between the heat input at the weld line and the axial shortening rate (Figure 1.6b). Figure 3.3 depicts a linear relationship between the computed heat input ($\propto af\tau$) and the axial shortening rate (v) which agrees with Turner *et al.* (2011) findings. At low heat input the simulation results tend to match the results obtained by Turner *et al.* (2011) but diverge as the heat input increases. The numerical simulation slope is lower than the experimental measurements one which may come from the material properties used in the numerical model. The regression predicts an axial shortening rate with no heat input which is impossible as no LFW takes place. However the mathematical analyses made on the results produce a linear axial shortening rate with respect to the heat input. Further analyses and investigations could be carried out to better understand the regression offset.
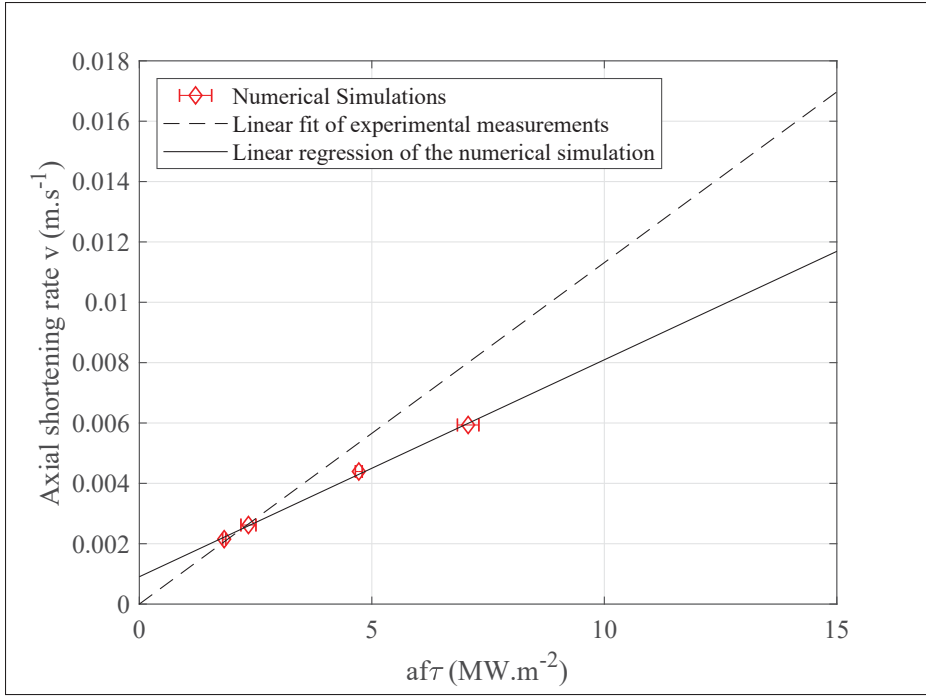
Figure 3.3   Linear regression between the heat input and the axial
shortening rate: experimental measurements from Turner *et al.*
(2011) (dashed line) vs computed axial shortening rate (solid line)

The Friction phase is subsequent to Phase I, and so, it is crucial that the latter stop at the right time. Figure 3.4 shows an early transition between Phases I and II. The beginning of the simulation ($t \in [0, 0.12]$) is still in Phase I as the axial shortening is still at zero. But the mathematical analysis renders a transition time (t_r) at 0.008 s and a bad correlation to the model established previously ($R^2 = 0.7666$). For this reason, the mathematical analysis used previously fails to identify correctly the phase characteristics: axial shortening rate, its evolution during Phase II, and the transition time. Thus, an inaccurate phase transition can bias the analysis and make the phase identification difficult.
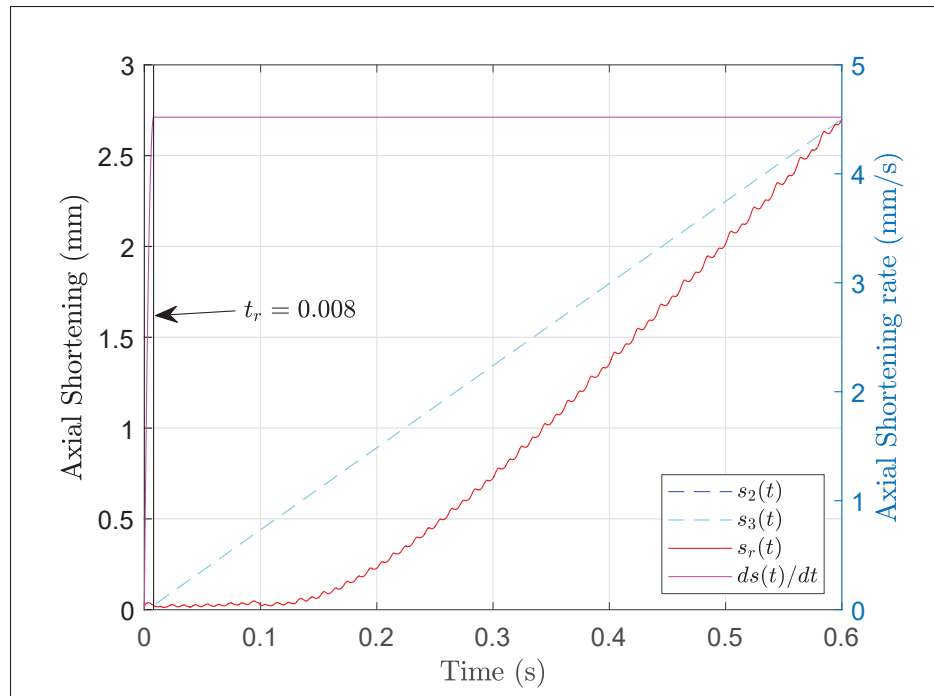
Figure 3.4   Failed axial shortening analysis during the Friction
phase with inaccurate transition between the Phase I and the
Phase II

3.1.3   Partial Conclusion

End phase criteria have allowed to discretize each process phase and provided clear mathematical definitions for numerical implementation:

- The numerical simulation of Phase I should be stopped when:
    - The thermo-mechanical (Equation 2.1) threshold is reached at the edges for a TMA approach.
    - The thermal threshold (Equation 2.4) is reached at the edges for a HTA approach.

- Phase II and Phase III can be gathered into the Friction phase and a mathematical analysis can identify both transient and steady state of the axial shortening.

Finally, it has been shown that an inaccurate phase transition alters the axial shortening evolution and make more difficult the identification of the phases characteristics.

3.2 Temperature Field Predicted by the Chained Simulations Model

The stationary TMA approach can be used to simulate Phase I in the chained numerical model. The temperature history and distribution are analyzed and compared to temperature measurements at different depths from the weld line from McAndrew *et al.* (2015a) study with the parameter set of the simulation #26 (Table 3.1). In addition, the temperature field obtained by the stationary TMA approach is compared to the one obtained by the TMA model to support their equivalence. The Friction phase characteristics such as the transition time between the phases II and III are used in the analysis of the temperature evolution.

3.2.1 Temperature during Phase I

3.2.1.1 Temperature History Predicted by the Thermal Model

For the Phase I, the process parameters from McAndrew *et al.* (2015b) study was used and the results were compared to the published thermocouple measurements. Figure 3.5 shows the thermocouple positions with the nearest numerical nodes from the TM simulation used for the comparison. The origin of the figure represents the center of the assembly i.e. the weld line center. (Z_{th}, Z_{node}) are the distance from the weld line to a thermocouple and a node, respectively. Four regions are present (from A to D in Figure 3.5) and used to analyze the temperature history.

Figure 3.5   Temperature distribution computed by TM with the thermocouples position (red diamonds) and reference nodes used (black crosses) for comparison: the regions of interest (A to D) are outlined in black

Region A is the closest to the weld line at 0.30 mm. Figure 3.6 shows that the temperature predicted for this region (solid lines) is overestimated compared to the thermocouple measurement (dashed lines) during Phase I. This over prediction is due to the penalty friction law (Figure 2.7) used to model the interaction between the two pieces and the limitation to calculate accurately the true contact pressure during Phase I. However, the temperature slope is similar to the measured one and the temperature at the end of the phase is close to the measured temperature. Despite that noticeable temperature overestimation near the weld line, the predicted temperature converges to the thermocouple temperature with an error of 4.35 % at the end of the phase (Table 3.2).

Table 3.2   Temperature predicted by the TM
simulation near the thermocouple A
($Z_{th} = 0.30\,\text{mm}$) at the end of Phase I with a
measured temperature of 929.16 °C

Z_{node}	Temperature Predicted	Error (%)
0.21 mm	982.52 °C	5.74 %
0.32 mm	969.62 °C	4.35 %
0.45 mm	955.72 °C	2.86 %
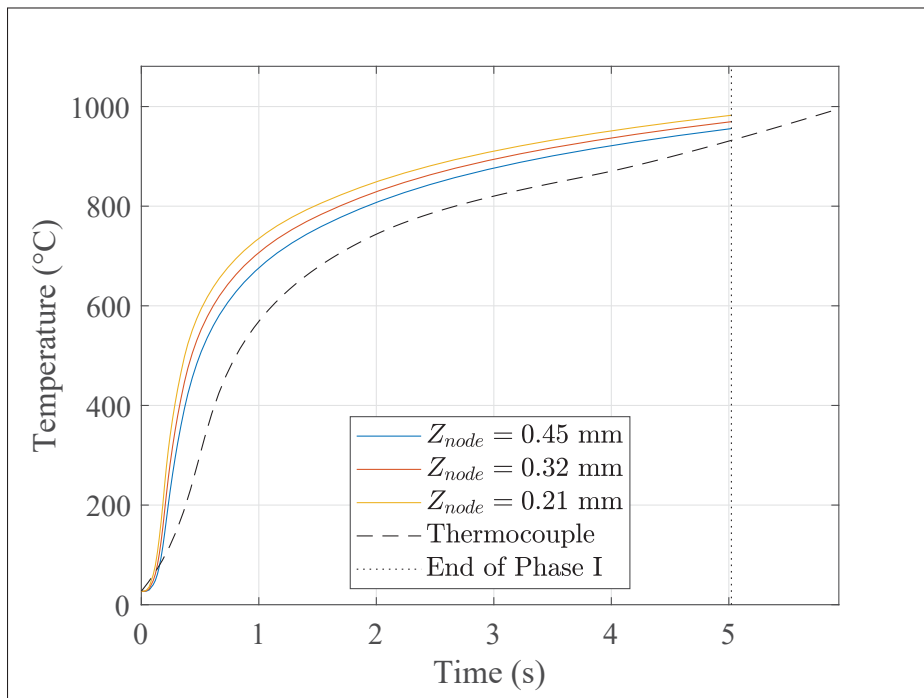
Figure 3.6   Temperature history in region A computed by TM
simulation compared to the thermocouple measurement at
different depths

Region B is located at 1 mm from the weld line. The measured temperature (dashed lines) is bounded by the temperature predicted at 0.87 mm and at 1.40 mm from the weld line during Phase I (Figure 3.7). That range of 0.57 mm (between 0.87 mm to 1.40 mm) can be due to the uncertainty of the thermocouple positioning: the epoxy used to hold the thermocouple could have offset it, generated that uncertainty.

However, the predicted temperature of this region shows good agreement with the measured one: the temperature slope is in good agreement with the measured one and the predicted temperature at the end of the phase has an error of 1.01 % (Table 3.3).

Table 3.3   Temperature predicted by the TM simulation near the thermocouple B ($Z_{th} = 1.00\,\text{mm}$) at the end of Phase I with a measured temperature of 879.69 °C

Z_{node}	Temperature Predicted	Error (%)
0.87 mm	907.22 °C	3.13 %
1.03 mm	888.60 °C	1.01 %
1.21 mm	868.54 °C	−1.27 %
1.40 mm	846.90 °C	−3.73 %
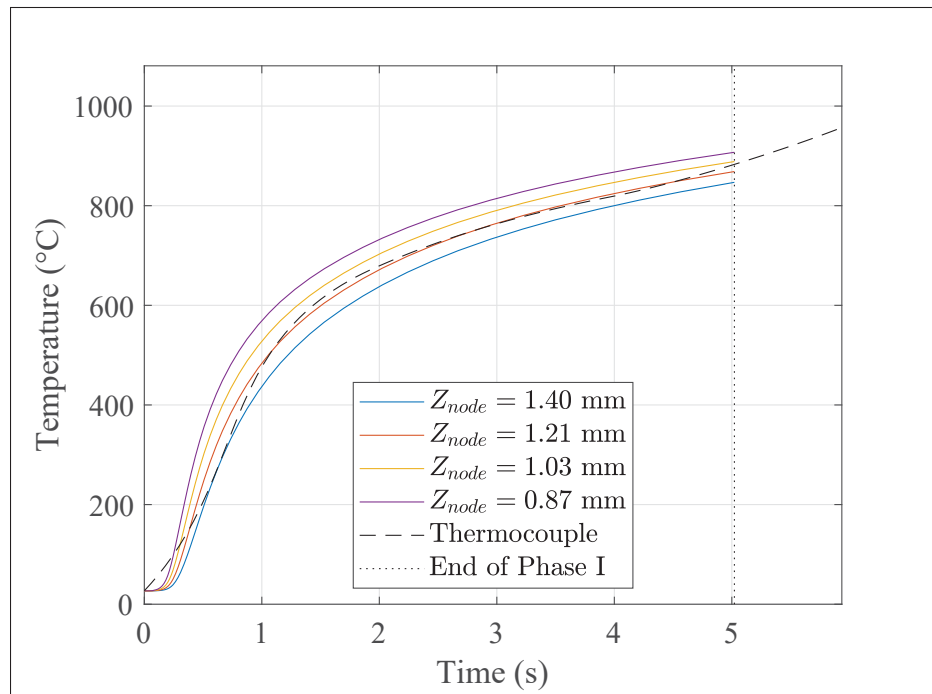
Figure 3.7   Temperature history in region B computed by TM simulation compared to the thermocouple measurement at different depths

Region C is located at 2.5 mm from the weld line. Predicted temperature at nodes 2.42 mm and 2.70 mm circumscribe the thermocouple temperature during Phase I (Figure 3.8) In addition, the predicted temperature slope is equivalent to the one measured by McAndrew *et al.* (2015b). At the end of Phase I the temperature is estimated with an error of $-0.04\,\%$ (Table 3.4). It corroborates that the numerical model predicts with a significant accuracy the temperature evolution in the sample during that phase.

Table 3.4 Temperature predicted by the TM
simulation near the thermocouple C
$(Z_{th} = 2.50\,\text{mm})$ at the end of Phase I with a
measured temperature of $710.78\,°\text{C}$

Z_{node}	Temperature Predicted	Error (%)
2.42 mm	726.27 °C	2.18 %
2.56 mm	710.49 °C	−0.04 %
2.70 mm	693.51 °C	−2.43 %

Figure 3.8   Temperature history in region C computed by TM
simulation compared to the thermocouple measurement at
different depths

Region D is located at 4.5 mm from the weld line (Figure 3.9). As for the region B and C, the

temperature predicted is consistent with the measured temperature. At the end of Phase I, it is

slightly over-predicted (Table 3.5) and the measured temperature is circumscribed by a larger

interval (0.64 mm) than those in region B and C. This discrepancy could be due to the influence

of the dies on the thermal diffusion in the sample. However, the temperature predicted in this

region is in agreement with the measured temperature in the sample with a good accuracy.

Table 3.5　Temperature predicted by the TM simulation near the thermocouple D ($Z_{th} = 4.50\,\text{mm}$) at the end of Phase I with a measured temperature of $457.53\,°\text{C}$

Z_{node}	Temperature Predicted	Error (%)
4.40 mm	490.82 °C	7.28 %
4.61 mm	467.10 °C	2.09 %
4.82 mm	442.26 °C	−3.34 %
5.04 mm	417.38 °C	−8.78 %
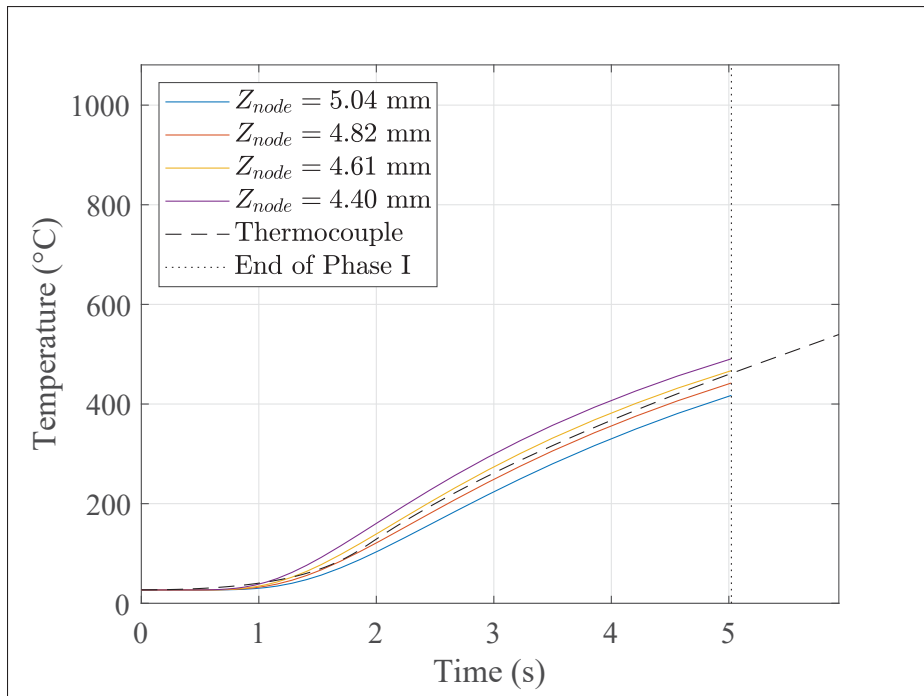
Figure 3.9　Temperature history in region D computed by TM simulation compared to the thermocouple measurement at different depths

3.2.1.2　Temperature History Predicted by the Oscillation Model

The TM simulation showed significant agreement with the temperature evolution measured by the thermocouples (McAndrew *et al.* (2015a)). The same process parameters were used in the OM simulation to support the equivalence between the TMA and the stationary TMA ap-

proaches. The same regions of interest are considered for each thermocouple but the reference nodes used, have changed from TM simulation as the mesh is different (Figure 3.10).
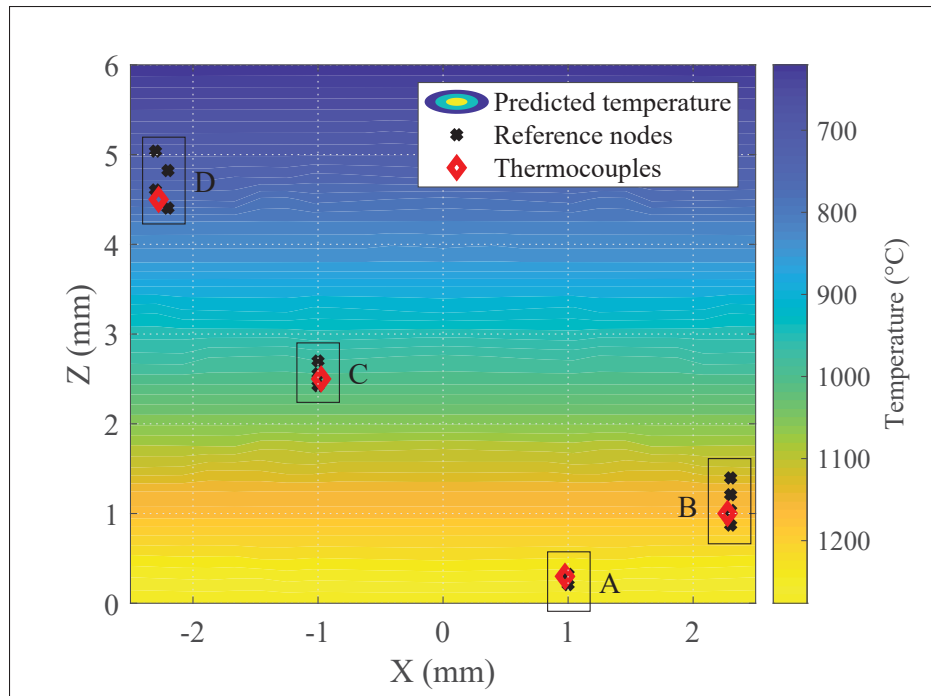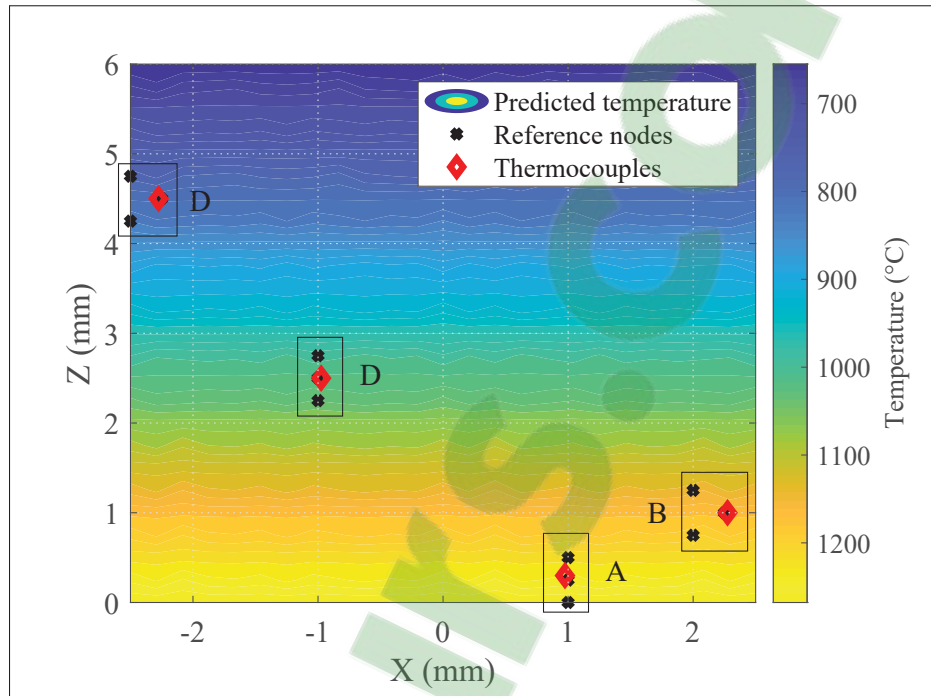

Figure 3.10   Temperature distribution computed by OM with the thermocouples position (red diamonds) and reference nodes used (black crosses) for comparison: the regions of interest (A to D) are outlined in black

As per the TM simulation, the temperature in the region A is over predicted compared to the temperature measured by the thermocouple at $Z_{th} = 0.3$ mm (Figure 3.11). The overestimation could also due to the friction model used in the simulation. However, the temperature slope is in agreement with the measured one and the computed temperature at the end of Phase I is within an error range of 0.66 % and 3.26 % (Table 3.6).

Table 3.6   Temperature predicted by the OM
simulation near the thermocouple A ($Z_{th} = 0.3\,$mm)
at the end of Phase I with a measured temperature
of 929.16 °C

| Z_{node}	Temperature Predicted	Error (%)
0.00 mm	983.97 °C	5.90 %
0.25 mm	959.61 °C	3.26 %
0.50 mm	935.26 °C	0.66 %
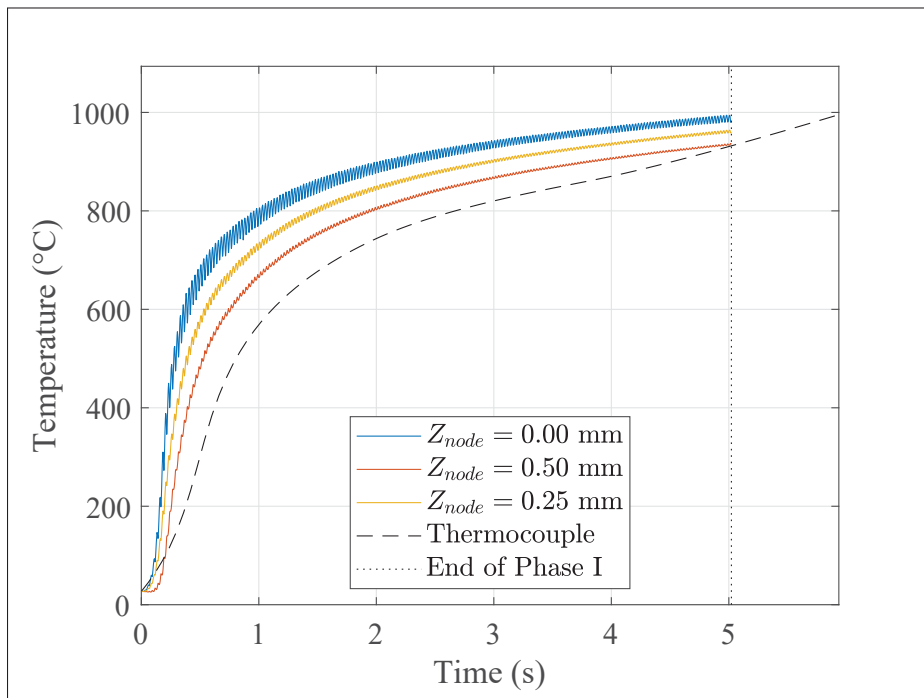
Figure 3.11   Temperature history in region A computed by OM
simulation compared to the thermocouple measurement at
different depths

At the end of Phase I, the temperature computed at the thermocouple location is accurate with
the measured one with an error of 0.1 % (Table 3.7). However, the temperature predicted at
1.25 mm is following the thermocouple temperature history (Figure 3.12). But, the evolution
of the temperature is respected and the thermal diffusion is well simulated.

Table 3.7 Temperature predicted by the OM simulation
near the thermocouple B ($Z_{th} = 1.0$ mm) at the end of
Phase I with a measured temperature of 879.68 °C

| Z_{node}	Temperature Predicted	Error (%)
0.75 mm	907.75 °C	3.19 %
1.00 mm	880.59 °C	0.10 %
1.25 mm	853.03 °C	−3.03 %
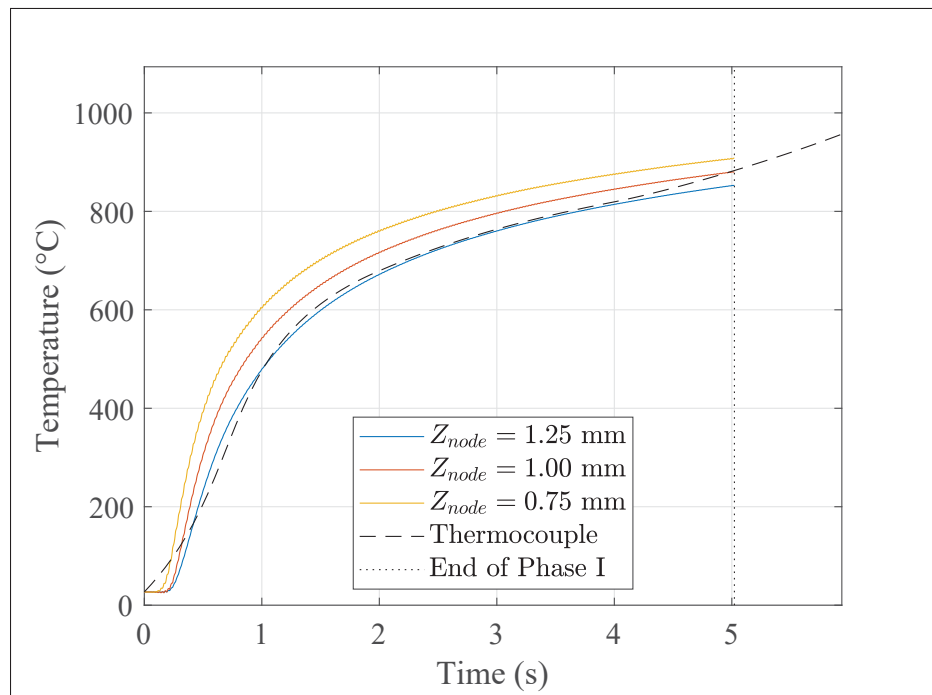
Figure 3.12 Temperature history in region B computed by OM
simulation compared to the thermocouple measurement at
different depths

Region C is as well predicted as the region B. The temperature at 2.75 mm from the weld line is following the thermocouple temperature at 2.5 mm (Figure 3.13). The 0.25 mm discrepancy can be explained by the setting and measuring uncertainty and the thermal diffusivity of the titanium alloy used for the test. At the end of Phase I, the temperature is predicted with an accuracy of 99.74 % (Table 3.8).

Table 3.8   Temperature predicted by the OM simulation near the thermocouple C ($Z_{th} = 2.5\,\text{mm}$) at the end of Phase I with a measured temperature of 710.78 °C

Z_{node}	Temperature Predicted	Error (%)
2.25 mm	741.18 °C	4.28 %
2.50 mm	712.61 °C	0.26 %
2.75 mm	683.76 °C	−3.80 %
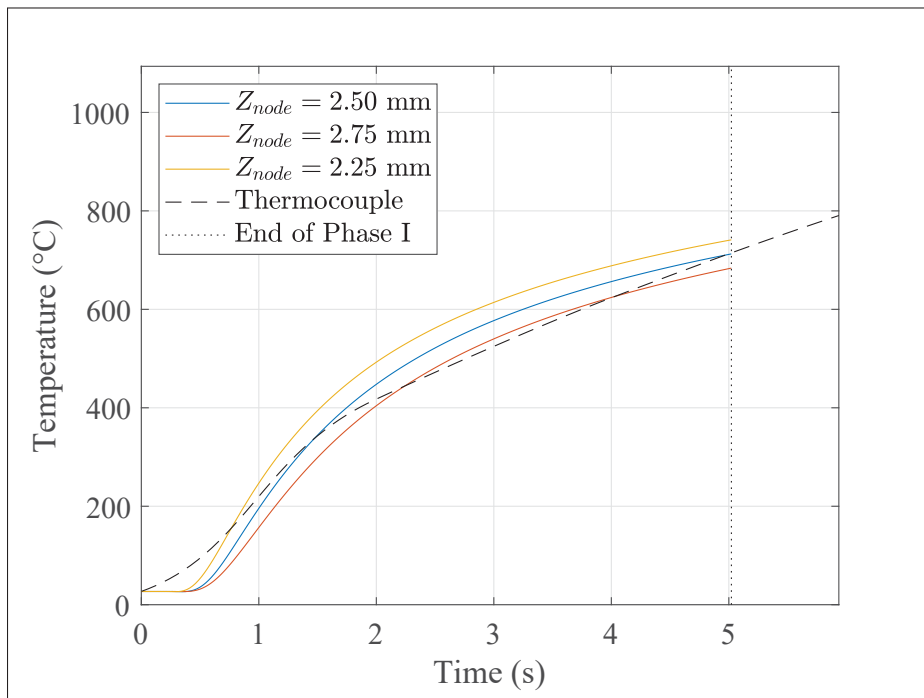
Figure 3.13   Temperature history in region C computed by OM simulation compared to the thermocouple measurement at different depths

The temperature predicted in region D follows the evolution of the temperature of the thermocouple (Figure 3.14). However the temperature at the end of Phase I is slightly over predicted by 4.93 % (Table 3.9). But, the numerical model can be still considered as reliable.

Table 3.9   Temperature predicted by the OM simulation near the thermocouple D ($Z_{th} = 4.5\,\text{mm}$) at the end of Phase I with a measured temperature of $457.53\,°\text{C}$

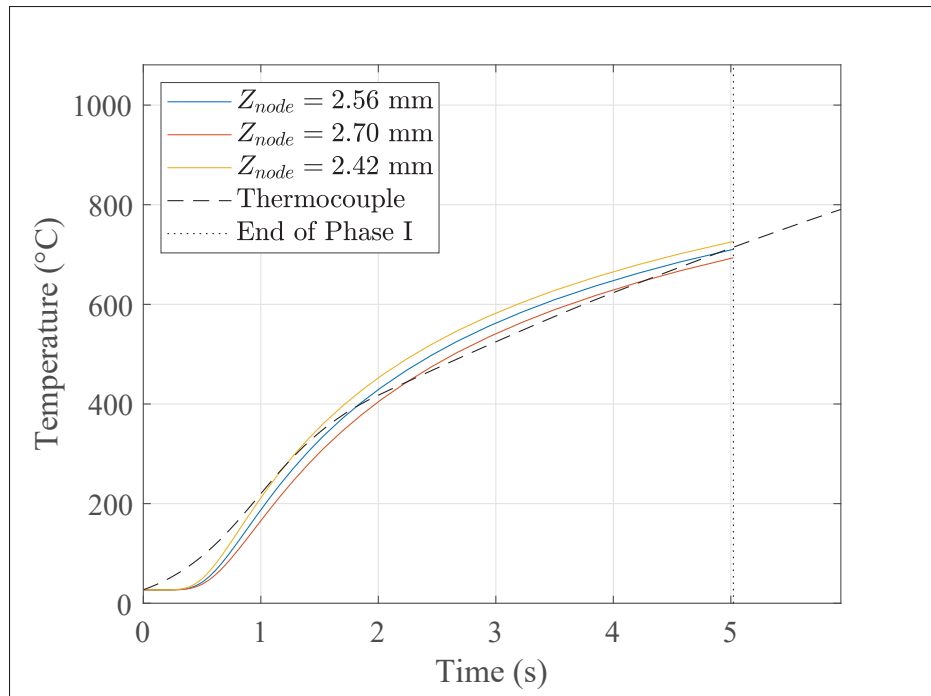| Z_{node}	Temperature Predicted	Error (%)
4.25 mm	508.81 °C	11.2 %
4.50 mm	480.09 °C	4.93 %
4.75 mm	451.32 °C	$-1.36\,\%$
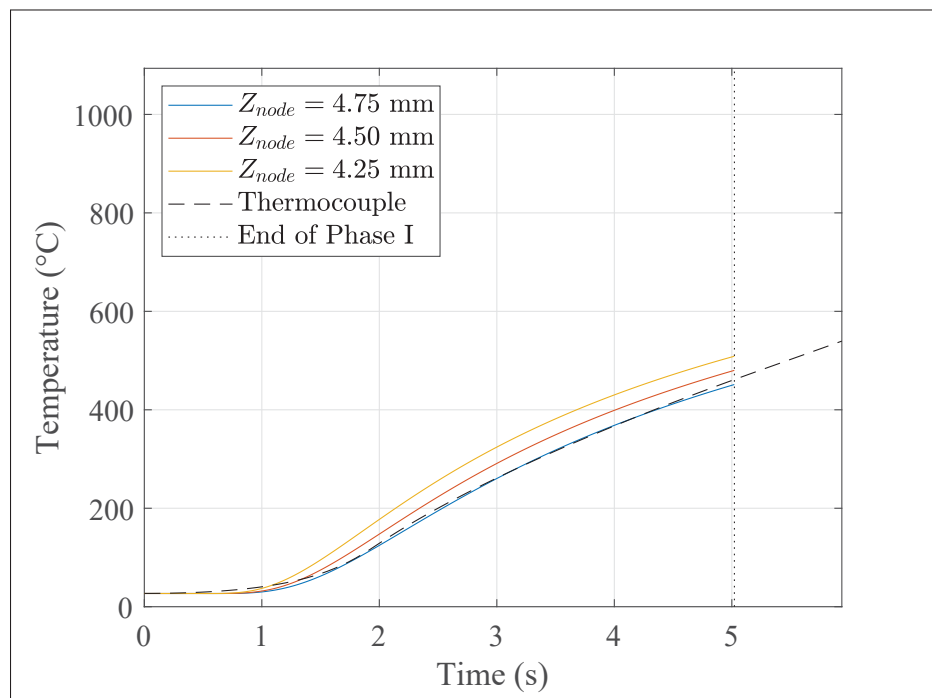
Figure 3.14   Temperature history in region D computed by OM simulation compared to the thermocouple measurement at different depths

Both TM and OM simulations have shown significant agreement with thermocouple measurements. The actual discrepancy present can be due to setting uncertainties and the specific material properties of the alloy used for the experiments. Figure 3.15 displays the relative error made by the TM on the temperature prediction compared to the OM simulation, taken as a reference. It can be noted that the TM simulation over predicts the temperature near the weld line and under predicts the temperature farther away for the weld line. But, as reported in

Table 3.9, the OM over predicted the temperature father away from the weld line whereas the TM is closer to the measured temperature (Table 3.5). The asymmetry in Figure 3.15 is due to the oscillations of the OM simulations and the field interpolation between the OM and the TM results. The error between the two simulations is between $-7\,\%$ and $2\,\%$, supporting the equivalence between the TMA and the stationary TMA approach.
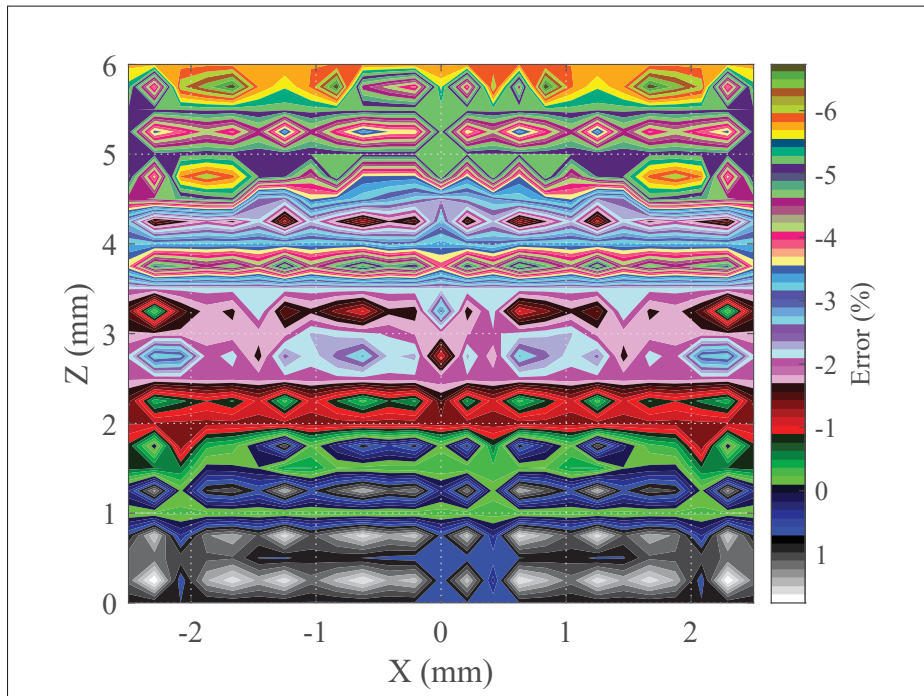
Figure 3.15   Error committed by the TM simulation to predict the temperature compared to the OM predictions at the end of Phase I

3.2.1.3 Temperature Distribution

In addition, three other simulations were carried out according to Table 3.1 from McAndrew *et al.* (2014) to study the impact of the process parameters on the temperature distribution at the end of Phase I.

Figure 3.16 depicts the temperature distribution across the workpiece center at the end of Phase I. The temperature gradient is influenced by the heat input as more heat is provided

to the weld line, the latter reaches more rapidly the thermal threshold and the heat does not diffuse into the workpiece (Table 3.10). As a consequence the width of the HAZ (w_{HAZ}) at 750 °C is smaller and the Phase I duration is shorter. Figure 3.17 presents the 2D temperature distributions obtained for each simulation at the end of Phase I which are used for their initial temperature respectively.

Table 3.10   Process characteristics for the different
simulations ordered by Phase I duration

Simulation	Heat Input	w_{HAZ} @ 750 °C	Phase I duration
#27	40.5 MW·m^{-2}	0.855 mm	0.581 s
#29	13.0 MW·m^{-2}	2.03 mm	3.35 s
#26	9.00 MW·m^{-2}	2.23 mm	5.02 s
#28	5.76 MW·m^{-2}	3.36 mm	11.8 s
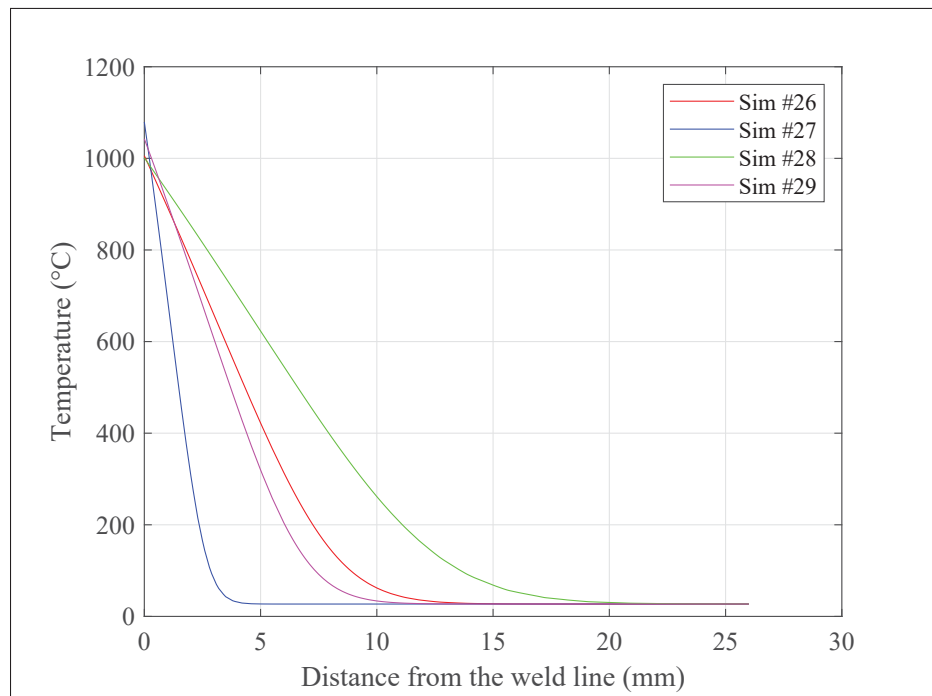
Figure 3.16   Temperature distribution perpendicularly to the
oscillations direction at the center of the workpiece at the end of
the Phase I
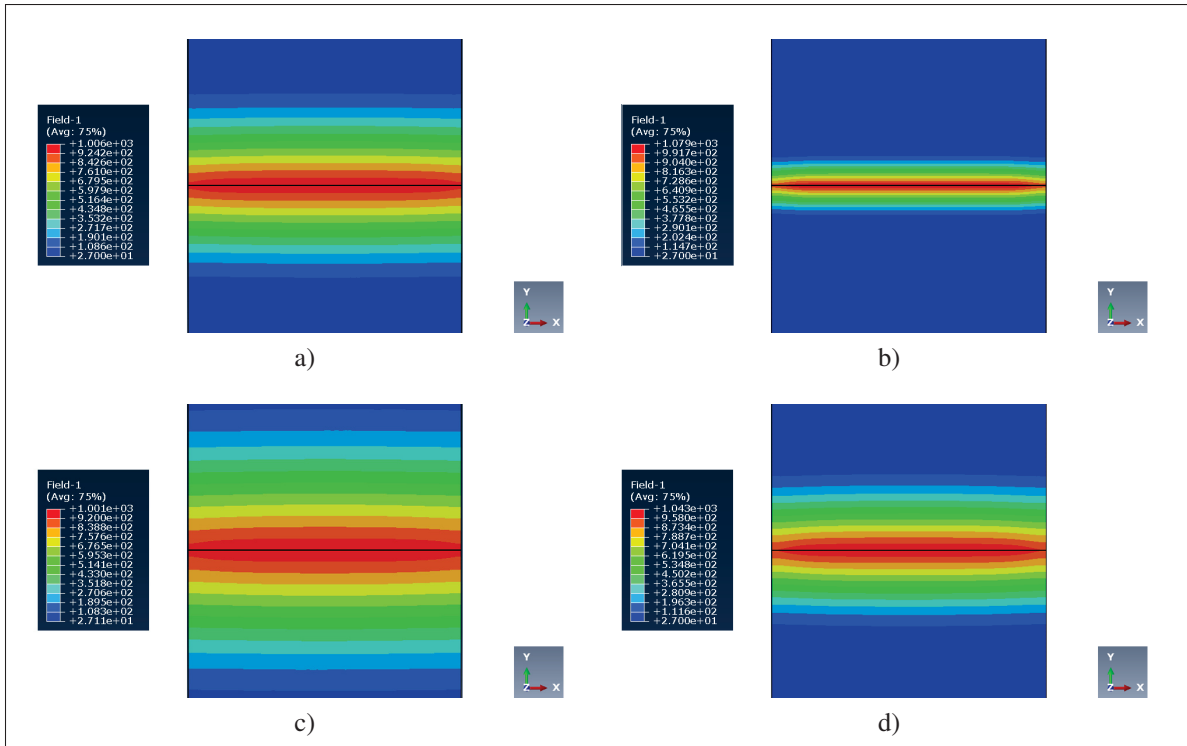
Figure 3.17   2D temperature distribution at the end of Phase I for: a) simulation #26, b) simulation #27, c) simulation #28, and d) simulation #29

3.2.2   Temperature During the Friction Phase

3.2.2.1   Temperature History

After processing the raw data, it was found that Phase II lasted 0.15 s (Equation 2.9). Figure 3.18 depicts the temperature evolution during the Friction phase. The model predicts the temperature quasi-steady state of 1034 °C at 0.50 mm during Phase III. For nodes entering in the WCZ during this phase (nodes at1.00 mm) the same working temperature is reached. The temperature in the WCZ is characterized by small variations of the temperature (Vairis & Frost (1998); McAndrew *et al.* (2015a)): between 1032 °C and 1051 °C due to the self-regulating characteristic of the LFW (Figure 1.4). Nodes farther away from the weld line (e.g, nodes at 2.5 mm and 4.5 mm) are moving toward the WCZ due to the axial shortening and so their temperature are increasing to reach the working temperature of the process. The Phase II end is

based on the axial shortening but it also brings the nodes close to the weld line to their working temperature.
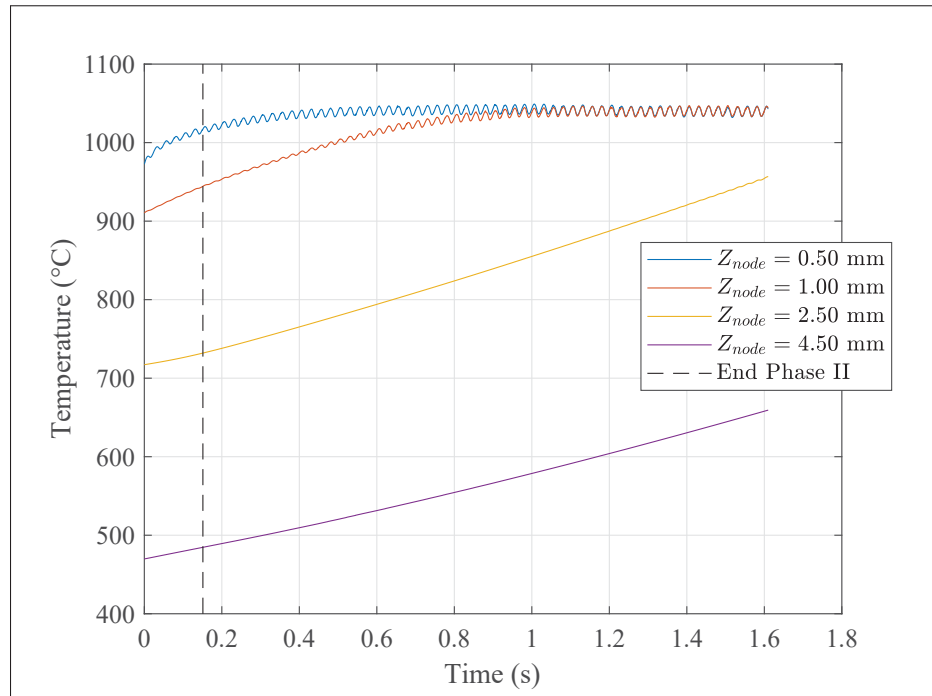
Figure 3.18   Temperature evolution during the Friction phase

3.2.2.2   Temperature Distribution

The Friction phase can also be seen as the forming phase as the visco-plastic layer is extruded, forming the joint. Complex correlations between all the process parameters occur during the extrusion of the flash.

For a given axial pressure, the rubbing velocity influences the material removal. A high rubbing velocity is prone to material removal as more material is expelled which creates a thin flash whereas a low rubbing motion produces a thicker flash (Table 3.11). In addition, as less material is removed, the heat generated by the visco-plastic deformation (Hosford & Caddell (2007)) is kept in the WCZ and diffusing in the workpiece. As a consequence, a low rubbing velocity produces a larger HAZ (Figure 3.19a) than a high-rubbing velocity (Table 3.11 -

Figure 3.19b). However, as the rubbing motion contributes to the heat generation, a high-rubbing velocity produces a higher maximum temperature in the WCZ.

For a given rubbing velocity, the axial pressure impacts both the material extrusion and the temperature distribution. With an elevated axial pressure (simulation #27), the material is squeezed at the weld line and due to its visco-plastic behavior, it is ejected faster from the weld line than with a lower axial pressure (Figure 3.19d). Also, the axial pressure has a direct impact on the heat generation, and so, the maximum temperature and the HAZ are directly impacted (Table 3.11).

However, the temperature distribution in Phases II-III is a competition between the heat diffusion in the workpiece and the flash extrusion which increases the contact surfaces with the environment, increasing the losses. In addition, the axial shortening is bringing new material to the weld line which slows down the heat diffusion. The simulation #27 has the optimum process parameters to limit the heat diffusion to the WCZ, and so, presents a small HAZ (Figure 3.19b).

Table 3.11   Flash thickness according to the rubbing velocity and
the axial pressure for each simulation ordered by flash thickness

Simulation	Rubbing Velocity	Axial Pressure	Flash Thickness	Maximum Temperature	w_{HAZ} @ 750 °C
#27	540 mm·s^{-1}	125 MPa	2.64 mm	1226 °C	1.46 mm
#26	120 mm·s^{-1}	125 MPa	3.33 mm	1043 °C	3.66 mm
#29	540 mm·s^{-1}	40 MPa	4.01 mm	1333 °C	4.66 mm
#28	240 mm·s^{-1}	40 MPa	4.32 mm	1208 °C	6.46 mm
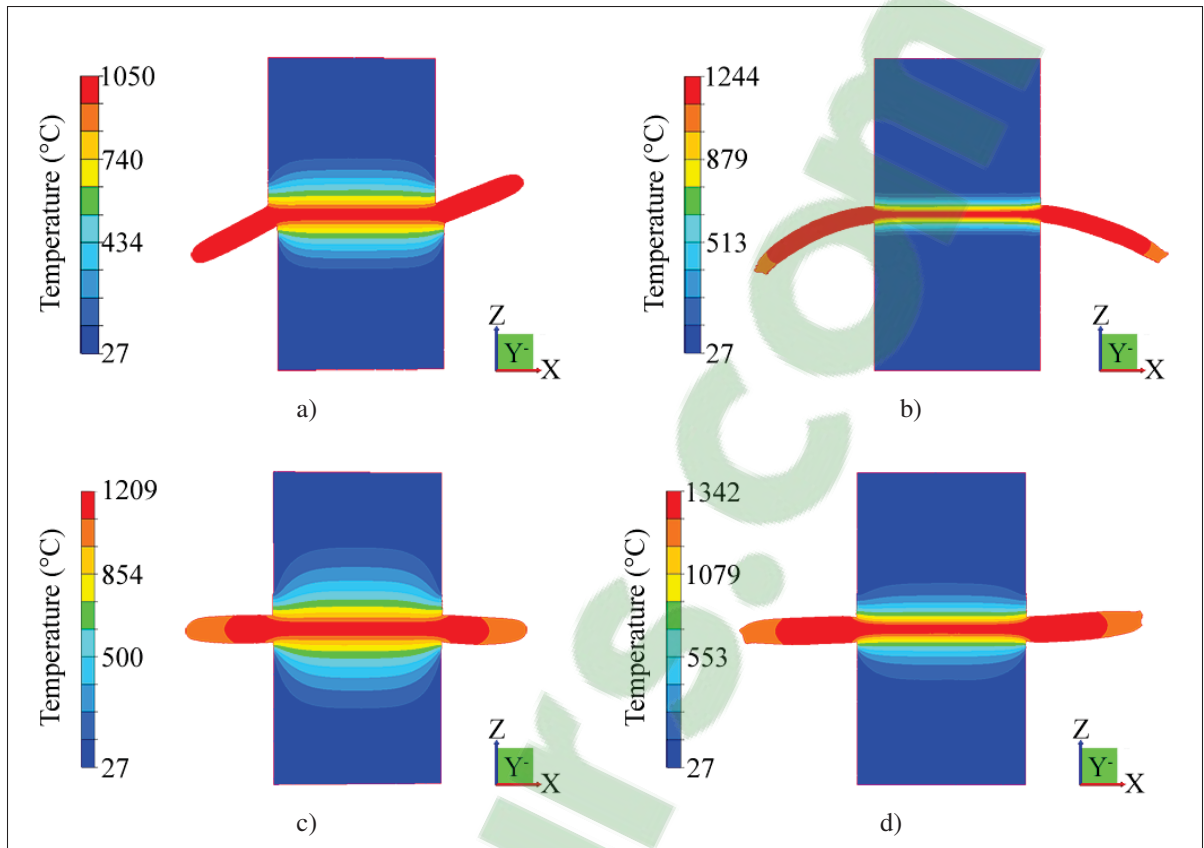
Figure 3.19   2D temperature distribution at the end of Phase III for: a) simulation #26, b) simulation #27, c) simulation #28, and d) simulation #29

Figure 3.20 supports that the HAZ width is influenced by the material removal. Simulation #27 with high capacity to expel the visco-plastic layer has a small HAZ (Figure 3.20b) compared to the simulation #28 which has lower value for the process parameters. It also shows the correlation between the rubbing velocity and the axial pressure in the extrusion mechanism. Specifically, Figures 3.20a and 3.20d depict a similar HAZ width, where one has low rubbing velocity, high axial pressure whereas the other one has high rubbing velocity, and low axial pressure. Table 3.12 highlights that the high axial pressure limits the heat diffusion during Phases II-III. The HAZ width has increased of 66 % during Phases II-III for simulations #26 and #27 with high axial pressure whereas the simulations #28 and #29 reveal a HAZ width increase of more than 100 %. Under high axial pressure, more material is removed as it was

observed with the flash thickness (Table 3.11), but with low axial pressure, the heat diffusion seems to be predominant over the material removal.

Table 3.12 HAZ width evolution between Phases I and III ends

Simulation	Phase I end	Phase III end	Evolution Phase I to III
#26	2.23 mm	3.66 mm	+64 %
#27	0.855 mm	1.46 mm	+71 %
#28	3.36 mm	6.46 mm	+92 %
#29	2.03 mm	4.66 mm	+129 %

3.2.2.3 Weld Line Displacement

The axial shortening is usually calculated from the top surface displacement as it is easily measured by a LVDT during joining. The weld line displacement is also liked with the axial shortening and virtually separates the upper and lower parts. The weld line displacement can be followed by the temperature maximum and it provides information on the material removal. Table 3.13 and Figure 3.20 report that the weld line displacement is equal to the half of the axial shortening with an error of 0.76 %. It attests that the material is expelled equally from both the lower and upper parts as the numerical model simulates similar material joining. As both parts have the same material properties, both should contribute for 50 % of the flash formation. It can be noted that, the weld line displacement in simulation #27 is more than half of the axial shortening by 1.9 % ($u_{wl} = 1.59$ mm $\geq \frac{s}{2} = 1.56$ mm). It corroborates that the process parameters used for this simulation are in favor of material removal and seems to be prone to remove more material from the lower part than the upper part.

Table 3.13   Weld line displacement and Axial
shortening for each simulation

Simulation	Weld line Displacement	Axial Shortening
#27	1.68 mm	3.38 mm
#26	1.59 mm	3.12 mm
#29	1.88 mm	3.73 mm
#28	1.97 mm	3.93 mm
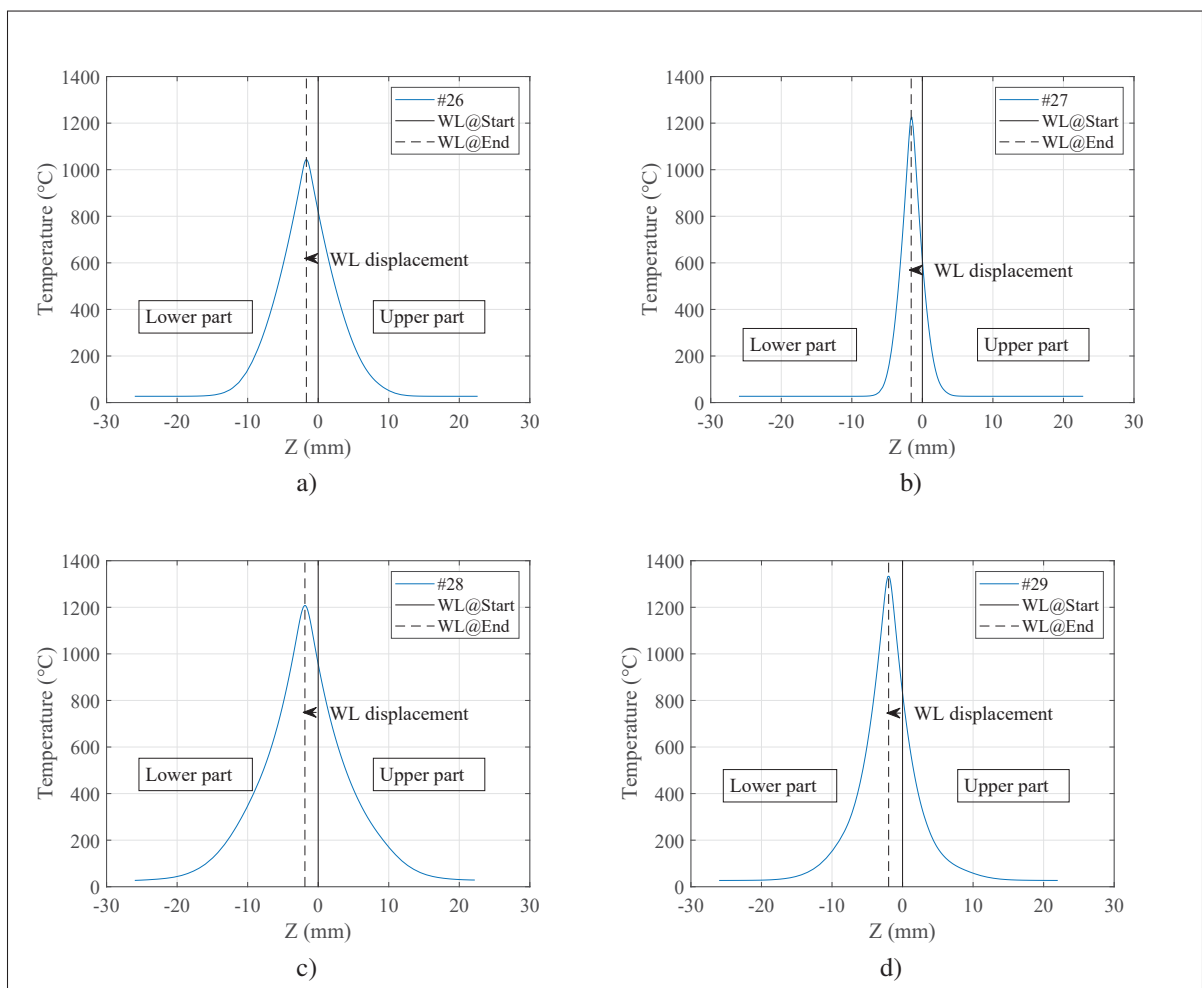
Figure 3.20   Temperature cross section at the workpiece center and the weld line
position at the end of Phases II-III for: a) simulation #26, b) simulation #27, c)
simulation #28, and d) simulation #29

3.2.2.4 Inaccurate Initial Conditions

Phases II-III are dependent on the initial conditions provided by Phase I simulation. Therefore, an inaccurate transition between Phases I and II may lead to inaccurate simulations.

Figure 3.21 highlights the consequences of an inaccurate transition between Phases I and III. The simulation #27 was obtained with an inaccurate transition criterion between Phase I and Phase II. The criterion considered was that Phase I shall stop when the center reaches $960\,°C$ whereas the correct criterion given by Equation 2.4) is considering at the workpiece's edges. Figure 3.21b reports that Phases II-III started when the edge temperature was below $900\,°C$. According to the Figure 3.1a, the weld line center is already visco-plastic, but the edge has still enough strength to support the process loading. As a result, the material extrusion does not follow the expected behavior for a Ti-6Al-4V alloy joint (Figures 3.21a and 1.17), creating a blob flash. Henceforth, it is important to implement the accurate phase definition with the right numerical model in chained simulation.
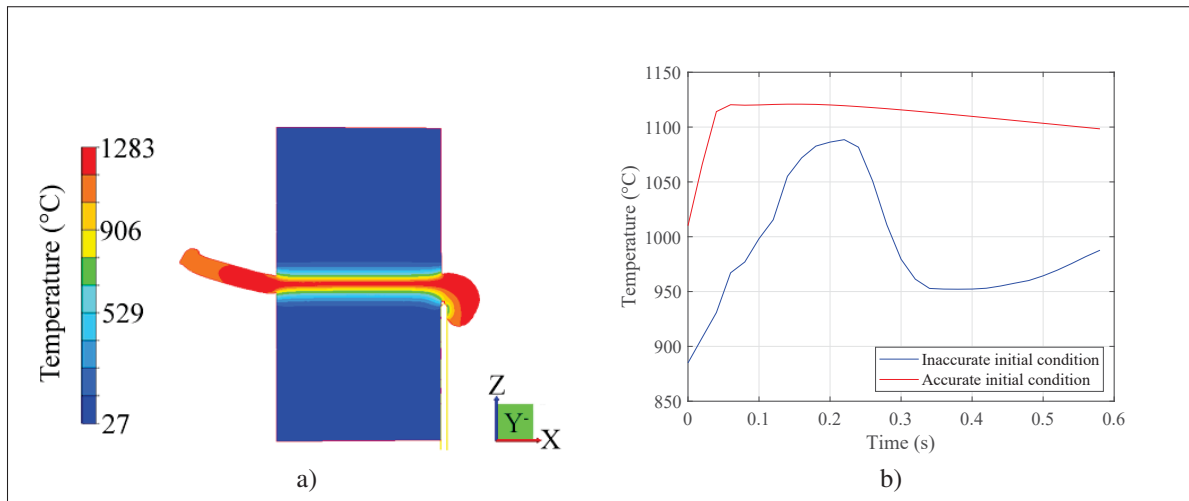
Figure 3.21   Consequence on the Friction phase when an inaccurate transition between Phases I and II: a) Temperature distribution at the end of Phase III, b) Temperature history at the weld line edge

3.2.3 Computational Efficiency

The efficiency of the thermal model approach was also confirmed by employing simulation #26. The time to complete the simulation will increase as the time step increment decreases (Table 3.14). The simulation #26 with the OM took 6454 s whereas it lasted 39 s with the TM. It must be noted that, even though the TM does not consider the oscillations, the heat flux at the interface generated by the subroutine agrees with the heat flux generated by the OM. Furthermore, the temperature profile generated by the TM is close to the profile generated by the OM (Figure 3.15). Finally, employing the average heat input (calculated from Equation 2.11) which can be applied by a subroutine in the thermal model reduced the computational time up to 99% with respect to the oscillating model.

Table 3.14   Computational cost analysis for the
Simulation #26

	Oscillatory Model	Thermal Model
Total of Increments	3381	30
Av time step per inc	1.39 ms	162 ms
Computational time	6454 s	39 s

3.2.4 Partial Conclusion

The chained numerical model combined two numerical models tailored for their associated phases:

-   Phase I was simulated by a stationary TMA approach which allowed to reduce the computational time up to 99 % with respect to the oscillating model. A comparison between TM and OM models were made to support the equivalence between the two models. It has been shown that TM is over predicting the temperature near the weld line but shown significant agreement with the measured temperature farther away from the weld line. Therefore, it models with a good agreement the temperature diffusion in the workpiece.

-   The SB model was able to provide a temperature map at the end of the Phase III. It allowed studying the temperature distribution as a function of the process parameters. The

results showed that high values for process parameters are prone for material removal and highlighted the complex correlation between the process parameters and the phase characteristics such as the axial shortening rate, the flash thickness, or the heat input.

Part of this work was presented in the 17th International Conference on Metal Forming in Toyohashi, Japan (Metal Forming 2018, September 16th-19th, 2018) and published in the journal "Procedia Manufacturing", September 2018 (Bertrand *et al.* (2018) - see Appendix II).

3.3 Microstructure Evolution

The microstructural transformation during the LFW impacts the joint mechanical properties and is crucial to predict from a design point of view. The chained numerical model has shown substantial agreement with measured temperature from thermocouples. Henceforth, the microstructural model established was included in the Friction phase model to provide a first approach of the microstructure evolution during Phase II and III of the LFW process.

3.3.1 Strain Rate in the Weld Center Zone

As mentioned in the literature (Wanjara & Jahazi (2005)), it is during the Phase III that the workpiece experiences most of its deformation due to the flash formation. Figure 3.22 reports the maximum strain rate that the WCZ experienced during Phases II-III. High strain rate of $10^2\,\text{s}^{-1}$ and $10^3\,\text{s}^{-1}$ were determined for simulations #26 and #27 respectively. The rubbing motion acts like the stirring tool in the Stir Friction Welding (SFW) to bond the workpieces, therefore, higher is the rubbing velocity, stronger will be the deformation. As the weld line is moving due to the axial shortening, points near the weld line center experience an increase in deformation up to the maximum deformation. There is no consensus in the literature regarding the expected strain rate range. On the one hand, Vairis & Frost (1998) provided an analytical estimation of the stain rate by Equation 3.1 which predicts $\dot{\varepsilon} = 1.15\,\text{s}^{-1} << 10^2\,\text{s}^{-1}$ for the simulation #26 and $\dot{\varepsilon} = 5.19\,\text{s}^{-1} << 10^3\,\text{s}^{-1}$ for the simulation #27. In addition, Geng *et al.* (2019a) published for GH4169 nickel-based superalloys, strain rates that agree

with Vairis & Frost (1998) analytic models. However, Turner *et al.* (2011); McAndrew *et al.* (2015a) predicted strain rate up to $2500\,\mathrm{s}^{-1}$ for Ti-6Al-4V alloy in their studies. Besides this controversy, the literature agrees that due to the strong deformation and the high temperature at the WCZ, microstructural changes occur during Phases II-III such as dynamic recrystallization.
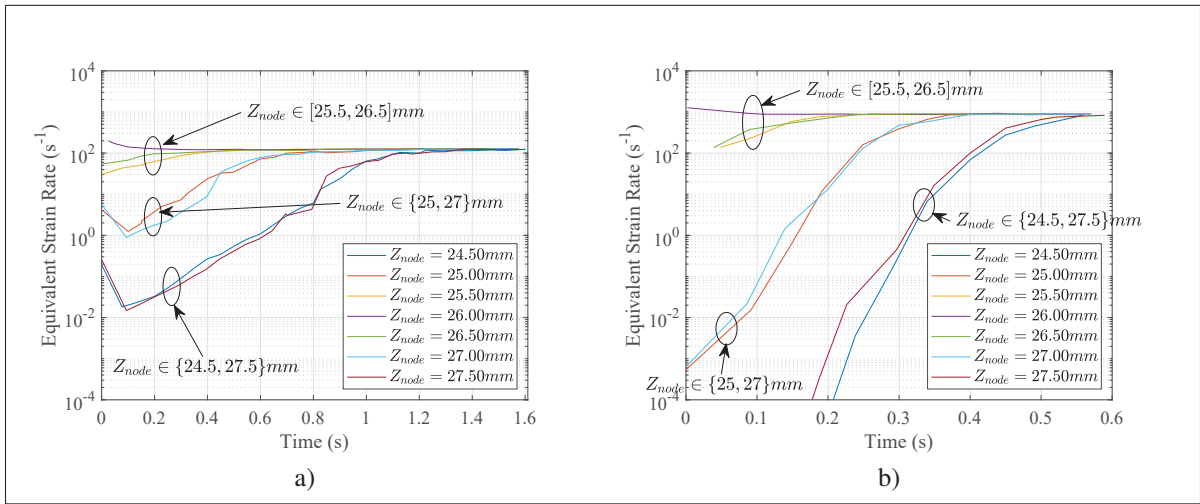
Figure 3.22   Strain rate evolution during the Phases II-III for: a) simulation #26, b) simulation #27

3.3.2   Microstructural Changes Indicator

The DRX cycle indicator introduced in this study quantifies the likelihood that a region has undergone microstructural transformations according to the JMAK equation (Equation 2.12). At the end of Phase III, as shown in Figure 3.23, the regions located at the junction of the flash and the billet are most likely those with the significant microstructural changes. This is due to the high strain rate applied at the edge of the billet while the flash is being extruded (McAndrew *et al.* (2015a)). Furthermore, the width of the transformed region at the weld line center is coherent with the width of the grain refinement seen in metallography; around 0.5 mm and 1 mm, depending on the process parameters (Wanjara & Jahazi (2005); Dalgaard (2011); McAndrew *et al.* (2017)). However, the DRX cycle indicator quantifies only the number of successive transformations according to the JMAK Equation 2.12 (Montheillet & Jonas (2009)).

The recrystallization process enfolds various competitive processes such as nucleation, grain growth, misorientation. For instance, the weld line center undergoes 48 DRX cycles, meaning there is a high probability for strong recrystallization resulting in significant grain refinement. However, it cannot be said that the grain size would continue to decrease indefinitely with the number of cycles. It is reasonable to assume that the grains will recrystallize to a given point and then an equilibrium should be found between the grain size and the other microstructural processes. Secondly, it must be noted that, the DRX cycle indicator uses the JMAK law which is out of scope for the LFW conditions.
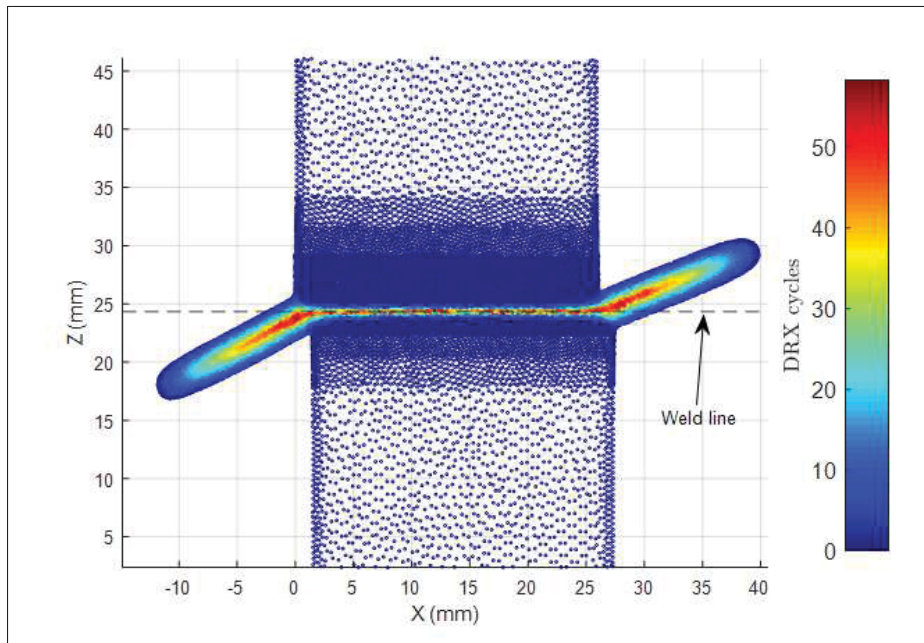
Figure 3.23   DRX extent at the end of Phase III for the
simulation #26

3.3.3   Comparison between the Predicted Microstructural Changes and Experimental Metallography

As mentioned, the grain refinement observed in LFW is part of the recrystallization process. The regions with a high microstructural changes indicator match the regions observed experimentally where grain refinement was identified (Wanjara & Jahazi (2005); Dalgaard (2011)).

Figure 3.24 shows on the metallography of the weld line center of the simulation #27 overlaid by its microstructural transformation prediction. The WCZ in the metallography matches with the high DRX cycles zone: between 55 cycles and 78 cycles. It indicates that grain refinement and grain reorganization are expected to occur in that zone because the process keeps deforming the region and introduces dislocations in the microstructure. Thanks to the high temperature and the small grain size, the dislocation can more easily move and reorganize the grain structure without further grain refinement.
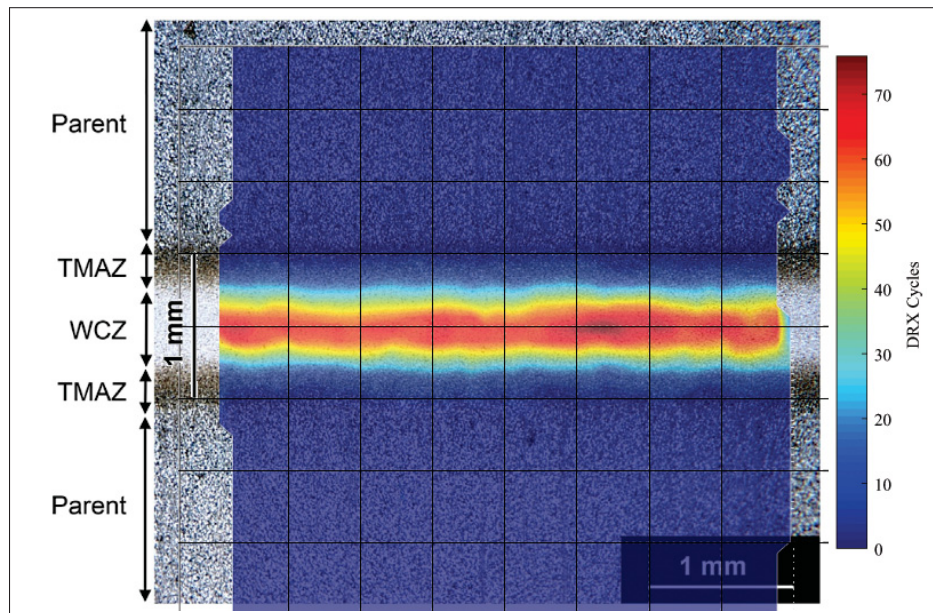
Figure 3.24   McAndrew *et al.* (2014) weld 6 - 50 Hz, 2.7 mm,
100 kN, 2 mm (simulation #27) overlaid with numerical
simulation of the microstructure evolution at the weld line

Figure 3.25 compares the metallography and the numerical prediction at the flash junction. The funnel extrusion shape present in Figure 3.25a is also present in Figure 3.25b. Visible transformed zones are present in the flash core at the junction with the workpiece and can be explained because of the severe deformation imposed by the oscillations and the material flow.
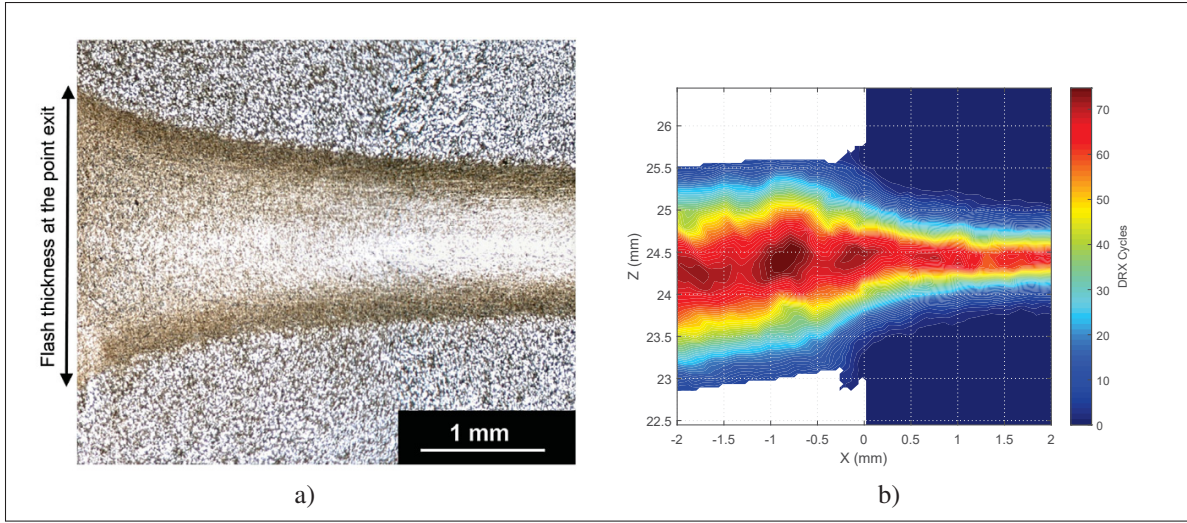
Figure 3.25   Comparison between metallography from McAndrew *et al.* (2015b) (a) and predicted microstructural transformed regions at the flash junction (b)

3.3.4   Partial Conclusion

Despite the JMAK equation extrapolation, the DRX cycle indicator has identified the regions where microstructural changes are most likely to occur. Those regions are in agreement with observations made on experimental metallography. However, to go further in the microstructural evolution prediction, it would be necessary to implement mesoscale simulation using dislocation density theory to model dynamic recrystallization. To this end, various methodologies such as polycrystal models (Anahid *et al.* (2011)) or cellular automaton (Zhao *et al.* (2008)) have been proposed. Further work is required to adapt those methods to the LFW process simulation.

Part of this work was presented in the 13th International Conference on Numerical Methods in Industrial Forming Processes in Portsmouth, NH, USA (Numiform 2019, June 23rd-27th, 2019)(see Appendix III).

CONCLUSION AND RECOMMENDATIONS

In this study, a literature review focused on the LFW process characteristics for numerical simulation was conducted. The process parameters which influence the LFW characteristics were studied. In addition, LFW challenges were illustrated by experimental and numerical publications. On the basis of the gaps identified in the literature, this study addressed the following points:

- The phase transitions are not accurately defined to be implemented in a chained numerical simulation. Therefore, this study suggested numerical transitions from one phase to the next by providing end phase criteria for both TMA and HTA approaches.

- The literature review showed that LFW simulations are still costly in terms of computational resources. Recent publications have shown that tailored model may be more efficient than general end-to-end model. This study has established a chained numerical model of the LFW process which allows the use of phase tailored model for both Phase I and Phases II-III. To improve the computational efficiency of the Phase I, a new stationary TMA approach was introduced by combining existing methods.

- Finally, this study introduced the first numerical model to study the microstructure evolution during Phases II-III. It is a first step to address the challenges related to the microstructure transformation occurring during the LFW.

The significant contributions of this research are:

- Establish end phase criteria to discretize the process phases for accurate numerical implementation. Phase I shall be stopped when the edges reach their thermal or thermo-mechanical threshold depending on the approach used to simulate the phase. Phase II and Phase III are identified by mathematical analysis of the axial shortening evolution. Axial shortening rate is calculated and characterizes whether the process is in favor of material removal.

- The stationary TMA approach was defined and combines the DOF of the TMA approach

but the workpieces are stationary as in the HTA approach. It was shown that OM and TM models are equivalent to simulate the Phase I. Despite an overpredicted temperature near the weld line, the simulations show significant agreement with thermocouple measurements.

- TM model reduces the computational run time by 99 % compared to the OM model. Henceforth, TM models may be privileged to simulate the Phase I and to obtain the temperature distribution at the end.

- Phases II-III simulations have shown a quasi-steady temperature during the Phase III as expected from the literature review. An analysis of the flash thickness has shown the ability of the process parameter to remove the visco-plastic layer. This study agrees with the analysis made on the axial shortening rate ability to influence material removal. In addition, it has been shown that inaccurate phase transition results in inaccurate process characteristic and in an inaccurate flash extrusion.

- A first microstructure model using JMAK equation was investigated to model the microstructural transformation during Phases II-III. A DRX cycle indicator was implemented in the numerical model to identify the region with high probability of microstructural transformation. The predicted results agreed with McAndrew *et al.* (2015a) metallography.

- Chained numerical model is suited for multi-physic simulations and each model used can be tailored to simulate specific output.

The recommendation of this study are:

- Phase I models can be further studied to include advanced contact interactions between the two workpieces and their consequences on the heat generation. A end phase criterion can also be examined for dissimilar material and experimental measurements can be conducted to support the numerical simulations.

- The Friction Phase gathered Phases II and III in one numerical model. The influence of the process parameter on the size of the HAZ, the flash thickness, the working temperature, and the weld line displacement can be studied for both similar and dissimilar alloys. Experimental studies can be conducted in parallel to support the simulations.

- Further investigations can be done to provide tailored individual model for Phases II-III. The latter can be approached with a fluid dynamic analysis to establish the relationship between the flash extrusion process and the process parameters.

- Further investigations are required to obtain accurate microstructural prediction such as grain refinement, nucleation, grain growth using dislocation density, polycrystals or cellular automaton models. In addition, experimental observations of metallograhy are needed to support such model.

APPENDIX I

FIELD MAPPING

This study uses two FEM software ABAQUS software and Forge software to simulate the Initial and the Friction phases respectively. As the Friction phase requires the temperature distribution at the end of the Initial phase, the temperature field must be extracted from ABAQUS software, mapped on the Friction phase mesh and imported in Forge software (Figure I-1).
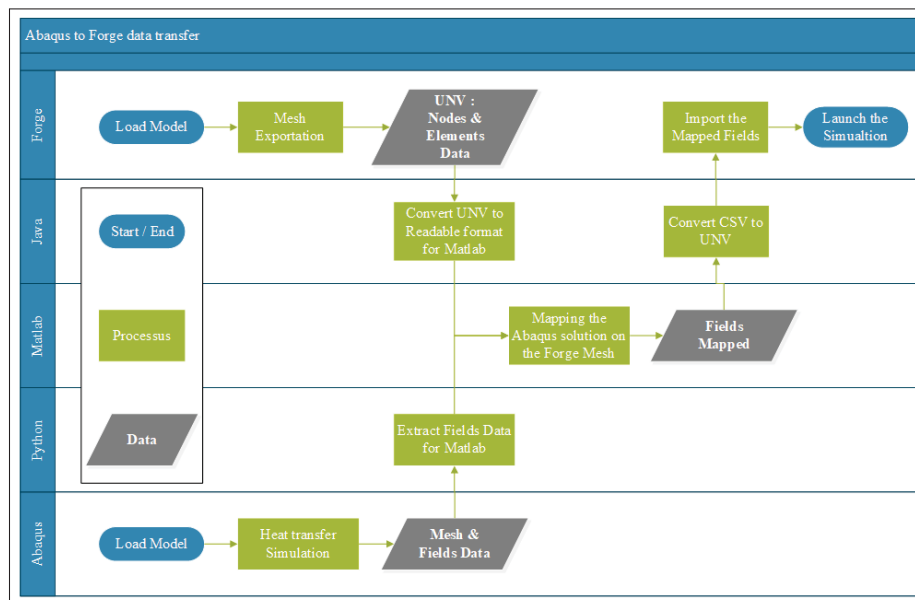
Figure-A I-1   Abaqus to Forge data transfer

A python script was written to extract from Abaqus ODB resutls the temperature field from the last frame. The node coordinate and the temperature at those nodes were written in a csv file for MatLab. In the meantime, on Forge software the Friction phase mesh is generated and exported in UNV format detailed in SDRL website[1]. A Java script was designed to read the UNV file and extract the nodes coordinates and connectivity table. Both were converted into a CSV format file for MatLab.

---

[1]   http://sdrl.uc.edu/sdrl/referenceinfo/universalfileformats/file-format-storehouse/universal-file-datasets-summary

In MatLab, both node coordinates are loaded in their respective set:

$$
\begin{aligned}
\Omega_{ABAQUS} &= \left\{ \forall i \in [0, N_a], \underline{X}_{a,i} = (x_{a,i}, y_{a,i}) \in \left[-\tfrac{w}{2}, \tfrac{w}{2} \right] \times [-h, h] \right\} \\
\Omega_{FORGE} &= \left\{ \forall j \in [0, N_f], \underline{X}_{f,i} = (x_{f,j}, y_{f,j}) \in [0, w] \times [0, 2h] \right\}
\end{aligned}
\tag{A I-1}
$$

with N_a, N_f the number of nodes, $(x_{a,i}, y_{a,i}), (x_{f,i}, y_{f,i})$ the node i coordinates for Abaqus and Forge respectively, and w the width and h the height of the workpieces (upper and lower). In addition, a temperature set Θ_{ABAQUS} is created from Abaqus temperature field such as :

$$
\forall i \in [0, N_a], \left\{
\begin{aligned}
& T : \Omega_{ABAQUS} \to \Theta_{ABAQUS} \\
& (x_{a,i}, y_{a,i}) \mapsto T_{a,i}
\end{aligned}
\right.
\tag{A I-2}
$$

The node coordinate set from Forge is translated to match Abaqus set. Then for each node $\underline{X}_{f,i}$ from Forge mesh, a region of interest $\Omega_{ROI} \subset \Omega_{ABAQUS}$ from Abaqus mesh is defined. This region of interest is triangulated by MatLab *delaunayTriangulation* function, returning triangular elements. The Abaqus element of interest $E_{a,EOI}$ containing $\underline{X}_{f,i}$ is then identified. That element is composed of three nodes:

$$
\exists (k, l, m) \in [0, N_a], E_{a,EOI} = \left(\underline{X}_{a,k}, \underline{X}_{a,l}, \underline{X}_{a,m} \right)
\tag{A I-3}
$$

Then, linear shape functions are applied on that element to obtain the temperature $T_{f,i}$ at the coordinates $\underline{X}_{f,i}$, knowing the temperature $(T_{a,l}, T_{a,k}, T_{a,m})$ at each Abaqus node. Therefore, by the finite element theory, the temperature $T_{f,i}$ is given by:

$$
T_{f,i} = \left(\begin{bmatrix} x_{a,l} & x_{a,k} & x_{a,m} \\ y_{a,l} & y_{a,k} & y_{a,m} \\ 1 & 1 & 1 \end{bmatrix}^{-1} \begin{bmatrix} x_{f,i} \\ y_{f,i} \\ 1 \end{bmatrix} \right)^{T} \begin{bmatrix} T_{a,l} \\ T_{a,k} \\ T_{a,m} \end{bmatrix}
\tag{A I-4}
$$

Finally, once the temperature at each node of the Forge mesh has been determined, MatLab exports it in a CSV file. The latter is then loaded by the Java script which creates the adequate UNV temperature block to import on Forge software.

LINEAR FRICTION WELDING PROCESS SIMULATION OF TI-6AL-4V ALLOY: A HEAT TRANSFER ANALYSIS OF THE CONDITIONING PHASE

Samuel Bertrand[1], Davood Shahriari[1], Mohamad Jahazi[1], Henri Champliaud[1]

[1]École de Technologie Supérieure, Département de Génie Mécanique, Montréal, H3C 1K3, Canada

Abstract

Linear Friction Welding is an emerging solid-state joining process used for complex geometries. The process is composed of four distinct phases: conditioning (also called initial), transition, friction, and forging. This paper proposes a new numerical approach to simulate the initial phase (phase 1) while reducing the computational time. An implicit fully coupled thermomechanical 2D analysis scheme in ABAQUS was employed to compare the proposed thermal model and the conventional oscillation model. Physical and mechanical temperature dependent properties of Ti-6Al-4V were implemented in the two models. An excellent agreement was obtained with the experimental temperature profiles published in the literature. The new thermal model reduces the computational time significantly: up to 99% with respect to an oscillating model.

1. Introduction

Linear Friction Welding (LFW) is a developing solid-state joining process that is being adopted for the manufacturing and repair of complex components, such as blade integrated disks (blisks) in turbines or aircraft engines. The transport and energy industries have a growing interest in this technology for its rapidity and its cost savings. The process is fast, conducted in few seconds [1], and it does neither require filling element nor gas shield protection compared to traditional welding methods. As a result, the manufacturing costs are reduced [1, 2]. The LFW process can be decomposed into four phases: initial, transition, friction, and forging phase. The temperature increases rapidly in the initial phase due to the solid-friction between the two workpieces. It leads to the thermo-mechanical threshold temperature in which the material at the interface is softened and can no longer sustain the contact pressure. Consequently, the material is expelled, and flashes are formed. Then the temperature and the extrusion rate reach a steady state. Finally, the oscillations are stopped, and the forging pressure is preserved or increased to consolidate the joint [2, 3, 4].

Numerical models allow to study and optimize the LFW processing parameters. Different numerical approaches have been already used [5]. Implicit and explicit solution schemes have been employed to carry out LFW simulation but the calculation time varies from hours to days [3]. In this paper, the initial phase (phase 1) is simulated and analyzed. During this phase, the two workpieces have a reciprocal motion which generates frictional heat. A sufficient heat-input is a prerequisite for plasticizing the material at the weld line which is a crucial parameter to have a sound joint. The axial shortening and the deformation are considered to be negligible in this phase compared to those occurring in the other phases. This study proposes a new method to reduce the computation time, and its efficiency is compared with the conventional oscillation models as well as experimental results.

2. Assumptions

The initial phase of LFW process is a critical phase because it produces the essential thermal energy to soften the material at the interface, which allows for preliminary joining of the interface. If the temperature at the weld interface does not reach the *threshold point*, the two workpieces will not be appropriately joined, resulting in a weak weld. The initial phase aims to reach the thermo-mechanical limit of the material close to the interface.

2.1 Ti-6Al-4V properties

The LFW model used a Ti-6Al-4V titanium alloy grade which is selected for blisks. For the modeling purposes, the material is considered to be homogeneous and isotropic. Additionally, temperature-dependent properties, physical and mechanical, were implemented in the model. These properties such as density, thermal conductivity (Figure-A II-1a), specific heat (Figure-A II-1b), Young's modulus, and the peak flow stress were obtained from both literature and Transvalor FORGE® NxT software's [6] library and implemented in ABAQUS. The flow stress in Ti-6Al-4V during hot deformation depends on temperature, strain, and strain rate. During LFW, temperature and strain rate continually increase, leading to changes in the flow stress. Therefore, it is essential to implement a material constitutive model to predict flow stress during the process. The Johnson-Cook model takes into account the effects of strain, strain rate hardening and also thermal softening. So, the flow stress at each simulation step can be quickly computed. This model for various materials has been already employed to simulate LFW process [7-11]. According to the Johnson-Cook model, the flow stress (σ_y) of material could be expressed by Equation A II-1, and its constants are summarized in Table-A II-1.

$$\sigma_y = \left[A + B \left(\overline{\varepsilon}^{\mathrm{pl}} \right)^n \right] \left[1 + C \log \left(\frac{\dot{\overline{\varepsilon}}^{\mathrm{pl}}}{\dot{\overline{\varepsilon}}_0^{\mathrm{pl}}} \right) \right] \left[1 - \left(\frac{T - T_0}{T_M - T_0} \right) \right] \qquad \text{(A II-1)}$$

Table-A II-1 Johnson-Cook material model
parameters for Ti-6Al-4V [7]

Parameter	Symbol	Units	Value
Reference strength	A	MPa	418.4
Strain-hardening parameter	B	MPa	394.4
Strain-hardening exponent	n	N/A	0.47
Strain rate coefficient	C	N/A	0.035
Room temperature	T_0	°C	25
Melting Temperature	T_M	°C	1660
Temperature exponent	m	N/A	1
Strain rate of reference	$\dot{\varepsilon}_0^{pl}$	s⁻¹	1

Ti-6Al-4V is an alpha-beta titanium alloy. The key to a successful hot deformation of this alloy is the beta transus temperature which is approximately $995°C$. The peak flow stress (Figure-A II-2) for Ti-6Al-4V alloy drops steeply from 750°C to 960°C and then shows steady-state behavior after beta transus temperature. That reduction indicates the material has reached its thermo-mechanical threshold and it is relatively soft to allow the bonding between the two parts, under the friction pressure. On this basis, in this study, it was assumed that the initial phase was completed when the interface temperature reached the beta transus temperature of 960°C ($\sim 0.6 T_M$).
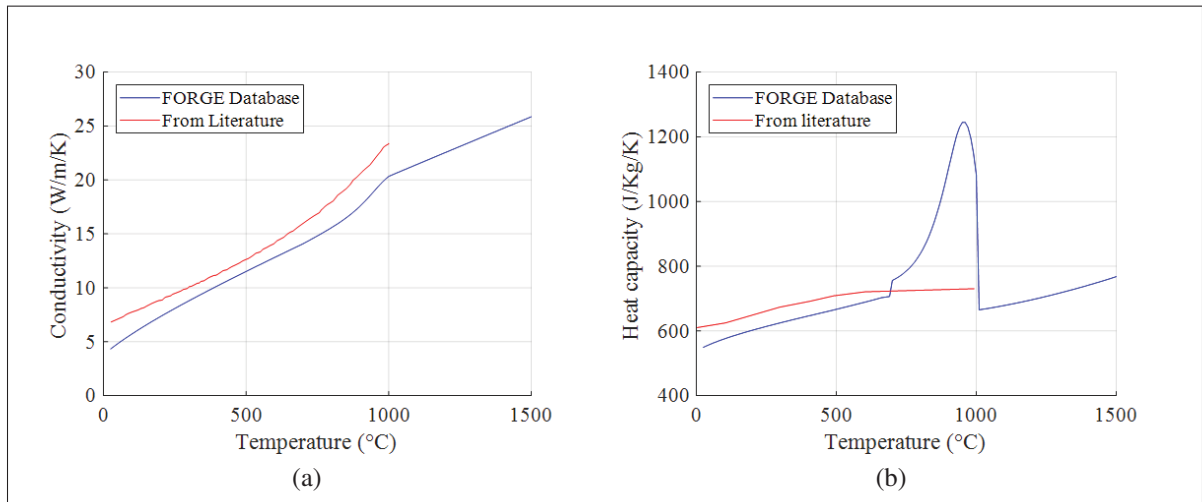
Figure-A II-1   (a) Thermal conductivity of Ti-6Al-4V reproduced from FORGE®
library (in blue) and literature [8] (in red), and (b) Heat capacity for Ti-6Al-4V
reproduced from FORGE® library (in blue) and literature [9] (in red).
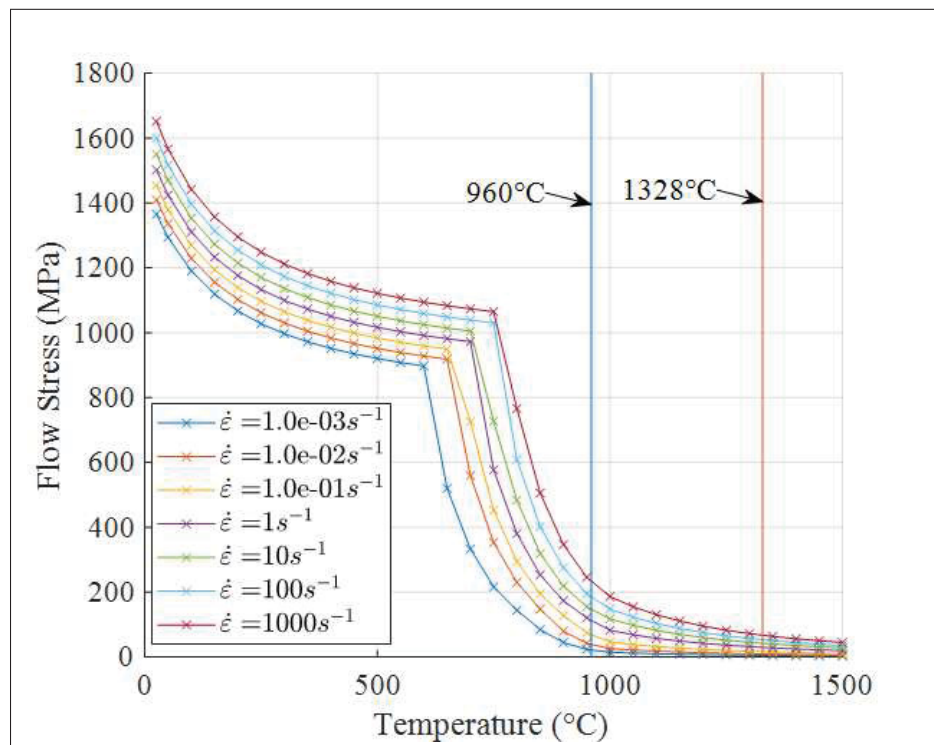
Figure-A II-2   The peak flow stress of Ti-6Al-4V depends
on the strain rate and temperature reproduced from
FORGE® library

2.2 Frictional Heat

Based on previous studies [2, 8, 12-14] the frictional heat during LFW process is generated between the two contact surfaces (rubbing surfaces) in reciprocal motion under friction pressure. Also, the heat loss on the generated thermal energy due to radiation and convection is neglected. The average frictional heat (HI) can be expressed as:

$$HI = 4\mu A f p_n \, \text{W/m}^2 \qquad\qquad \text{(A II-2)}$$

where μ is the Coulomb's friction coefficient, A, f and p_n are respectively the amplitude, oscillation frequency and contact pressure. The friction coefficient is a function of several factors such as interface temperature, contact pressure, surface topology, etc. In this study, the Coulomb's friction coefficient is assumed to be affected by the rubbing surfaces and the temperature (Figure-A II-3). This study suggests calculating the average frictional heat according to the process parameters and to apply it directly on the rubbing surfaces. It differs from the oscillating method where the frictional heat is determined at each time step according to the shear stress at the interface and the relative velocity of the two parts.
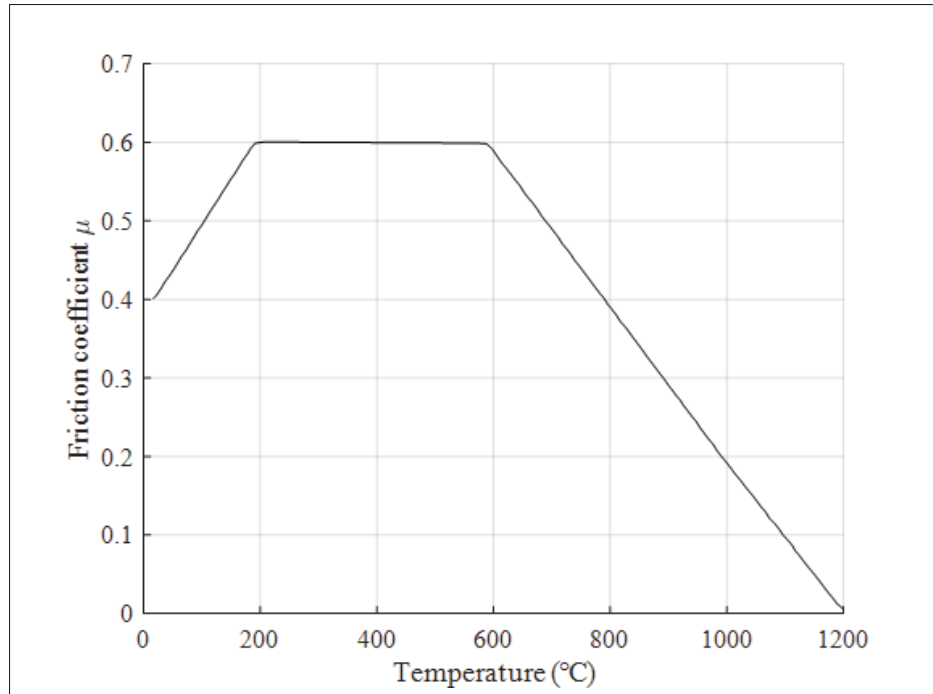
Figure-A II-3   Temperature-dependent friction coefficient,
$\mu\,(T)$, for Ti-6Al-4V [8].

3.   Numerical models

A 2D model was implemented in ABAQUS/STANDARD software. As shown in Figure-A II-4, the model is divided into two parts: lower and upper part. Each of them is a deformable body and has a length of 26mm, a width of 13mm, and a height of 26mm. They are divided into three zones: the Heat Affected Zone (HAZ), the Thermo-Mechanically Affected Zone (TMAZ), and the parent material. The first two zones start at the welding line and spread up to 8mm [2] then reach the parent material where no plastic deformation occurs throughout the LFW process. An element size of 0.5mm was taken in the TMAZ and HAZ in agreement with [7], and the remainder of the workpiece was meshed to an element size of 2.5mm.

Simulations were conducted using a transient coupled time displacement and fully coupled thermomechanical analysis. The latter needs the use of elements with both temperature and displacement degrees of freedom (DOF). Thus, in this work, CPS8RT (8-node biquadratic displacement, bilinear temperature, reduced integration) quad elements were employed from

the ABAQUS library. Each part has 3945 nodes and 1352 elements. The initial temperature for both parts was predefined in ABAQUS at 27°C representing room temperature.

The Oscillation Model (OM) has been used to simulate the four phases of the LFW process by several authors [4, 8, 7]. However, this approach is very time-consuming. A solution is to simulate each phase separately. The proposed Thermal Model (TM) focuses only on the heat generated by the friction in the initial phase. It replaces the dynamic thermal-structural simulation of the heat, generated by the oscillation, by an equivalent heat input (eq. 2) and analyses the heat diffusion through the workpiece. Since 3D model requires significant computational resources, a 2D configuration was considered to assess the proposed methodology throughout the initial phase. In this way, the 2D model in-plane-stress condition represents a slice at the center of a 3D model. The upper workpiece was constrained in x-displacement along the side faces of the parent material. In addition, the contact pressure was applied at the top of this part, and the gravity was not considered in both models. Moreover, the bottom face of the lower part was fixed in y-displacement. The heat flux coefficient at the edges surface of the HAZ and the TMAZ was set to $-10W.m^{-2}$ as proposed by [2, 11]. Its negative sign represents the heat loss by the heat exchange between the HAZ and the ambient atmosphere.
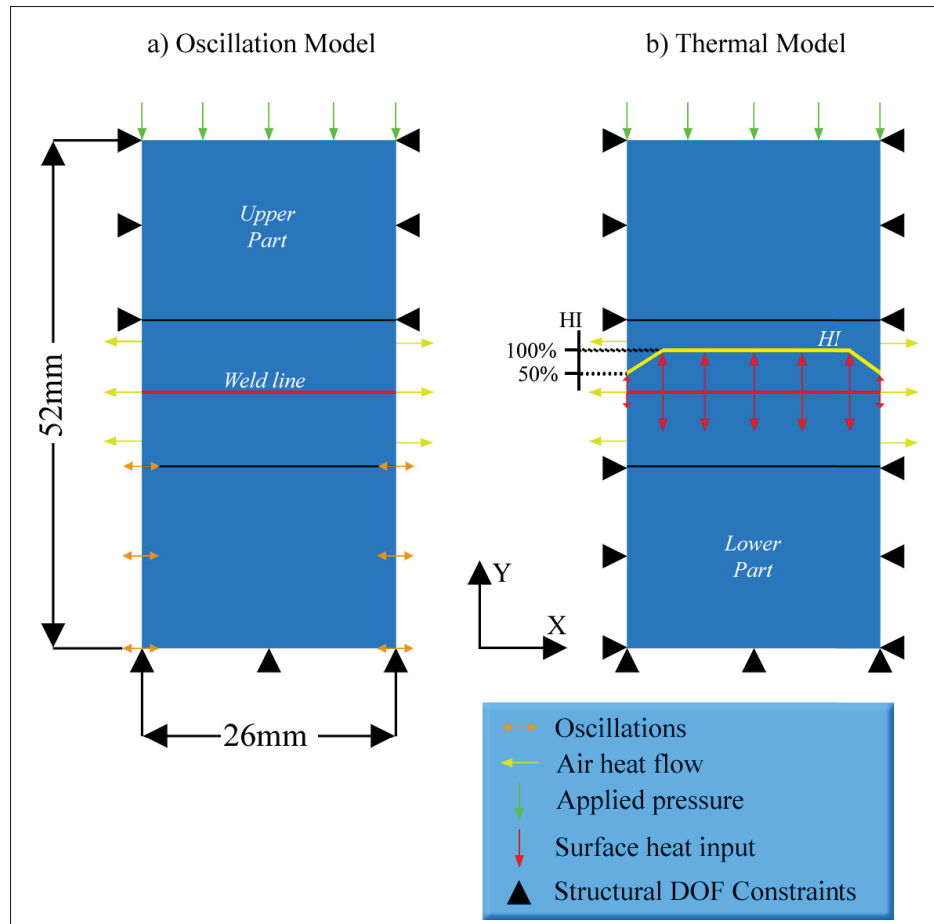
Figure-A II-4   Numerical model: a) oscillating model, b) heat
transfer model

3.1   Oscillating model

The four phases of the LFW process can be simulated when reciprocating motion is imposed. However, considering the oscillating movement of the workpiece increases the calculation time [3], the thermo-mechanical interactions are interdependent. Specifically, the temperature depends on the heat diffusion which depends on the heat flux at the weld interface. The latter depends on the friction work converted into heat which is a function of the temperature at the interface.

In the present study, a time-dependent displacement was defined as a sinusoidal function $u(x)$ on the lower part along the two side faces of the parent material in the x-direction (Figure-A II-4.a):

$$u(x) = A \sin(2\pi \text{ft}) \qquad \text{(A II-3)}$$

Furthermore, the interface properties define a temperature-dependent friction coefficient (Figure-A II-3) according to the Coulomb's law. "Inelastic Heat Fraction" for the material and "Gap Heat Generation" are also defined, considering that 90% of the friction energy [10] was converted to heat and used as a heat source: 50% of the frictional heat was assigned to each deformable part (i.e. equal heat distribution).

3.2   Thermal model

In the proposed model, the heat input replaces the friction interaction thereby simplifying the simulation: the heat released by the friction is instantaneously calculated and imposed. The simulation focuses on the heat diffusion and its conduction through the workpieces. The average heat input was determined using Figure-A II-3, in which the friction coefficient is temperature-dependent and then the calculated heat input at each time step was assigned at the interface using a user-defined subroutine (ABAQUS/DEFLUX). Non-Uniform heat flux was applied along the weld interface to compensate reciprocation movement of the lower part relative to the upper one in the thermal model. Indeed, the oscillating motion causes a portion of the lower and upper part (in an amplitude length) to experience more heat transfer with the environment thereby resulting in a slight decrease in temperature [2, 10, 11]. Therefore, it may be assumed that the heat flux distribution is linearly reduced from 100% to 50% along the weld interface over a length A (amplitude) from each side of the lower and upper parts, as shown in Figure-A II-4.b.

4. Results and discussion

In order to compare the proposed numerical methodology with the oscillation model, two processing parameters with LFW of the investigated alloy were used from the literature [12, 10]. Since LFW experiments had been performed by these parameters, the measured temperatures under these conditions were used to compare and validate the computed temperature results obtained from the two numerical methods. Furthermore, during the experiments, temperature evolution was recorded by thermocouples at various depths from the weld line. Interpolations were made to analyze the simulated temperature at the same location the thermocouples measured the temperature during the experiments. The values of the parameters (Simulation Parameters #1 & #2) used for the thermal and oscillation model simulations are listed in Table-A II-2.

Table-A II-2   LFW processing parameters obtained from Bühr et al. study [12]
(Simulation Parameters #1) and McAndrew et al. study [10] (Simulation
Parameters #2)

Welding Parameters	Simulation Parameters #1	Simulation Parameters #2
Frequency	50Hz	20Hz
Amplitude	2.7mm	1.5mm
Pressure	90MPa	125MPa

4.1 Temperature analysis

As can be seen in Figures-A II-5 and II-6, the predicted temperatures of the thermal and oscillation models agree with experiments provided by Bühr et al. and McAndrew et al. studies [13, 15]. By using simulation parameters #1, the initial phase was completed in 0.82s for both thermal and oscillation models. The temperature at 0.3mm away from the weld line is 887°C according to Bühr et al. [12]. The simulated temperature at the same point is 886°C and 867°C for TM and OM, respectively.

The efficiency of the thermal model approach was also confirmed by employing simulation

parameter #2. In this condition, the primary phase of LFW process lasted 4.7s. It can be seen that the temperature at 0.3mm away from the interface at the end of phase 1 for TM and OM simulations is 920°C and 897°C, respectively, for a measured temperature of 912°C. These results are also in good agreement with the simulation results obtained with the simulation parameter #1.

The time required to complete the process decreases as the average surface heat input increases [2]. Considering the heat input Equation A II-2 and the friction coefficient average value form Figure-A II-3, $\mu = 0.43$, the average heat input is 20.9W.mm^{-2} and 6.45W.mm^{-2} for simulation #1 and simulation #2, respectively. The findings correlate well with simulation #2 for which the initial phase takes 4.7s while it takes 0.82s for simulation #1.

A comparison between the predicted and measured temperatures for the thermal and oscillation models by using simulation parameters #1 and #2 as well as their computational time are shown in Table-A II-3 and Table-A II-4. Thermal model results show a better agreement with the experimental values than that the oscillation one. The average absolute between the calculated and experimental temperatures along the TMAZ and HAZ in both thermal and oscillation models is 0.83% and 5.19%, respectively. Therefore, the proposed thermal model with the lowest average error is a suitable approach to simulate the initial phase of LFW process to optimise their processing parameters in phase 1.

Table-A II-3   Error between the predicted and measured temperatures [12] for both thermal & oscillation models by using simulation parameters #1

Model	Thermal model	Oscillating model
0.3mm	- 0.0640%	- 2.22%
2.7mm	- 0.736%	-12,5%

Table-A II-4   Error between the predicted and measured temperatures [10] for both thermal & oscillation models by using simulation parameters #2

Model	Thermal model	Oscillating model
0.3mm	- 0.864%	- 1.75%
1.0mm	- 2.25%	-4.54%
2.5mm	-0.663%	-2.76%

Figure-A II-5   Temperature history profile obtained under simulation parameters #1 at different distances from weld interface: (a) thermal model simulation (TM) results and (b) oscillation simulation (OM) results. The simulation results compared with experiments (exp) retrieved from Bühr et al. study [12]
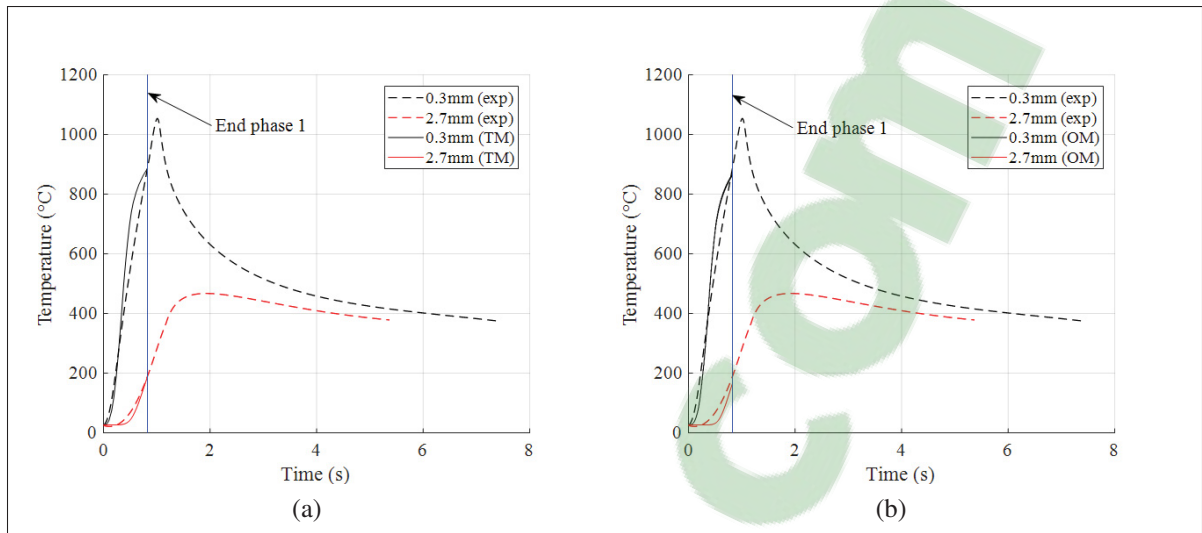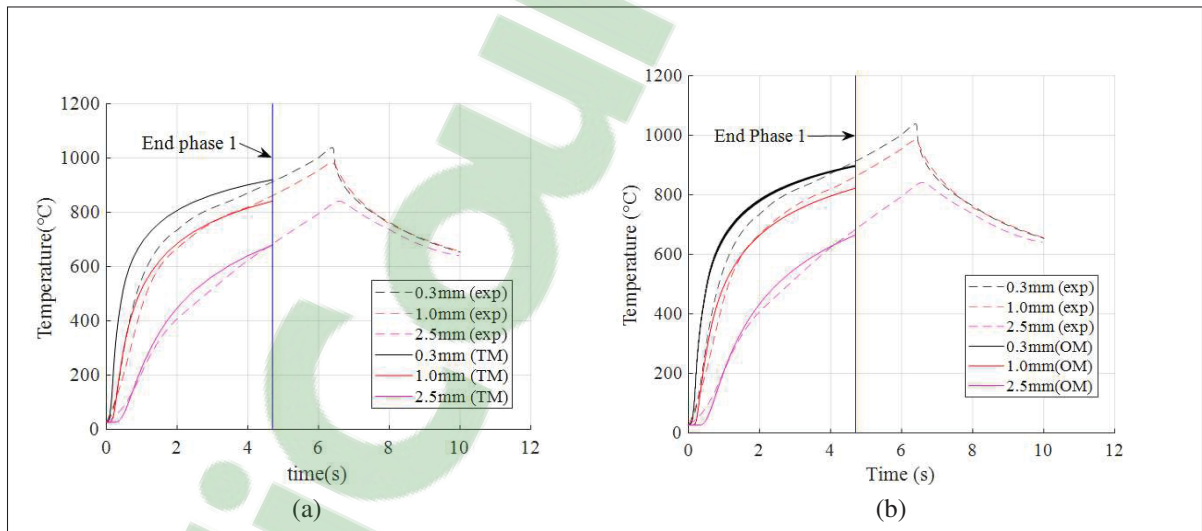

Figure-A II-6   Temperature history profile obtained under simulation parameters #2 at different distances from weld interface: (a) thermal model simulation (TM) results and (b) oscillation model simulation (OM) results. The simulation results compared with experiments (exp) retrieved from McAndrew et al. study [10].

4.2   Computational time analysis

The Oscillation Model simulates the reciprocal motion and high plastic deformation. It requires appropriate time step increments to accurately calculate output variables, such as the heat generated by friction. Therefore, this model has a high computational cost and might lead to convergence issues (e.g. a tiny time-step increment can lead to numerical instability). Understanding heat input during LFW process initial phase is the key variable.

The heat flux occurring at the interface is calculated by the OM according to the reciprocal motion and the interface properties. Thus, the heat flux depends on the user-defined displacement function (Equation A II-3): it is a continuously variable function (e.g. sinusoidal), and the oscillation frequency defines the time step increments (i.e. higher is the frequency, smaller are the time step increments). The Thermal Model instead, uses a user-subroutine to calculate the heat flux. This subroutine defines a linear piecewise function which varies less than a sinusoidal function. Therefore, the time step increment for the TM can be longer than the one for the OM.

As a result, the time to complete the simulation will increase as the time step increment decreases (Table-A II-5). The simulation #1 with the OM took 43min12s whereas it was 33s with the TM. The calculation time is much higher for simulation #2 as it took 1h47min to complete the simulation with the OM while it took only 39s to run it with the TM. It must be noted that, even though the TM does not consider the oscillation, the heat flux at the interface generated by the subroutine agrees with the heat flux generated by the OM. Furthermore, the temperature profile generated by the TM is close to the profile generated by the OM but with better accuracy, as previously mentioned. Finally, employing the average heat input (calculated from (Equation A II-2)) which can be applied by a subroutine in the thermal model reduced the computational time up to 99% with respect to the oscillating model.

Table-A II-5   Computational cost analysis

Simulation Parameters	#1	#2
Total Inc. (TM)	24	30
Total Inc. (OM)	1166	3381
Average time step inc.(TM)	36ms±40ms	162ms±385ms
Average time step inc.(OM)	0.71ms±1.5ms	1.39ms±2.36ms
Computational time (TM)	33s	39s
Computational time (OM)	2592s	6454s
Process time simulated	0.82s	4.7s
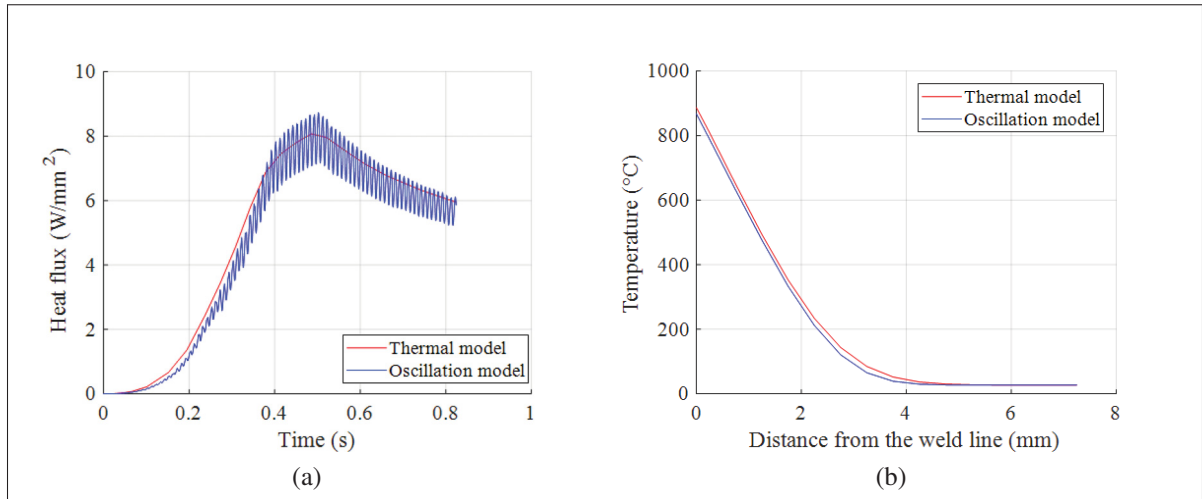
Figure-A II-7   Comparation between the two models: (a) Simulated heat flux and (b) Temperature profile at the mid-length of the workpiece at the end of the initial phase by using simulation parameter #1.

5.   Conclusions

This study provided a new numerical approach to simulate and optimize the initial phase parameters during LFW process. The following conclusions could be made:

- The computational time in the thermal model simulation is less than 99% the time used for the oscillation model simulation.

- The comparison between the published measured and calculated temperature profiles during phase 1 confirmed the accuracy of the proposed thermal model.

References

[1] F. Schroeder, R. M. Ward, R. P. Turner, M. M. Attallah, J. Gebelin and R. C. Reed, Linear friction welding of titanium alloys for aeroengine applications: modelling and validation, *9th International Conference on Trends in Welding Research, (*2012) 886-892.

[2] A. R. McAndrew, P. A. Colegrove, A. C. Addison, B. Flipo and M. J. Russell, Energy and Force Analysis of Ti-6Al-4V Linear Friction Welds for Computational Modeling Input and Validation Data, *Metallurgical and Materials Transactions A: Physical Metallurgy and Materials Science,* 45 (2014) 6118-6128.

[3] A. Vairis and M. Frost, "Modelling the linear friction welding of titanium blocks, *Materials Science and Engineering A,* 292 (2000) 8-17.

[4] L. Fratini and D. La Spisa, Numerical simulation of linear friction welding (LFW) processes, *AIP Conference ConferenceProceedings,* 1353 (2011) 1284-1289.

[5] G. Buffa and L. Fratini, Strategies for numerical simulation of linear friction welding of metals: a review, *Production Engineering,* 11 (2017) 1-15.

[6] Transvalor, FORGE NxT - Présentation, [Online]. Available: https://www.transvalor.com/fr/cmspages/forge-nxt.32.html. [Accessed 2 3 2018].

[7] W.-Y. Li, T. Ma and J. Li, Numerical simulation of linear friction welding of titanium alloy: Effects of processing parameters, *Materials & Design,* 31 (2010) 1497-1507.

[8] M. Grujicic, G. Arakere, B. Pandurangan, C. F. Yen and B. A. Cheeseman, Process modeling of Ti-6Al-4V linear friction welding (LFW), *Journal of Materials Engineering and Performance,* 21 (2012) 2011-2023.

[9] L. Maio, F. Franco, A. Squillace and L. Lecce, A simplified approach to numerical simulation of LFW process of Ti6Al4V alloy: investigation on friction and temperature, *International Journal of Advanced Manufacturing Technology,* 86 (2016) 3217-3228.

[10] A. R. McAndrew, P. A. Colegrove, A. C. Addison, B. Flipo and M. J. Russell, Modelling the influence of the process inputs on the removal of surface contaminants from Ti-6Al-4V linear friction welds, *Materials and Design,* 66 (2015) 183-195.

[11] A. R. McAndrew, P. A. Colegrove, B. Flipo and C. Bühr, 3D modelling of Ti-6Al-4V linear friction welds, *Science and Technology of Welding and Joining,* 1718 (2016) 1-9.

[12] C. Buhr, P. A. Colegrove and A. R. McAndrew, A computationally efficient thermal modelling approach of the linear friction welding process, *Journal of Materials Processing Technology, (*2017).

[13] R. Turner, J. C. Gebelin, R. M. Ward and R. C. Reed, Linear friction welding of Ti-6Al-4V: Modelling and validation, *Acta Materialia,* 59 (2011) 3792-3803.

[14] R. Turner, F. Schroeder, R. M. Ward and J. W. Brooks, The importance of materials data and modelling parameters in an FE simulation of linear friction welding, *Advances in Materials Science and Engineering,* 2014 (2014) 1-9.

[15] W. Li, F. Wang, S. Shi, T. Ma, J. Li and A. Vairis, 3D Finite Element Analysis of the Effect of Process Parameters on Linear Friction Welding of Mild Steel, *Journal of Materials Engineering and Performance,* 23 (2014) 4010-4018.

APPENDIX III

NUMERICAL MODELING OF MICROSTRUCTURE EVOLUTION IN TI-6AL-4V ALLOY DURING FRICTION PHASE OF LINEAR FRICTION WELDING PROCESS

Samuel Bertrand[1], Davood Shahriari[1], Henri Champliaud[1], Mohamad Jahazi[1]

[1]École de Technologie Supérieure, Département de Génie Mécanique, Montréal, H3C 1K3, Canada

Abstract

Linear Friction Welding (LFW) is a solid-state joining process used to manufacture complex components. This process is decomposed into conditioning, friction, and forging phases. During friction, the microstructure undergoes severe deformation that results in significant grain refinement by dynamic recrystallization (DRX). A numerical model is presented for DRX of a titanium alloy during the friction phase. Simulations were carried out using Transvalor FORGE NxT® 1.1 software. The DRX kinetic was modeled using Johnson, Mehl, Avrami, Kolmogorov equation. The temperature distribution and axial shortening as well as DRX regions and their volume fraction were computed. The obtained results show the occurrence of up to 48 DRX cycles across the weld line. The results also revealed DRX zones in regions close to the weld line and in the flash. A good agreement was observed with data published in the literature.

1. Introduction

Linear Friction Welding (LFW) is a *solid-state joining process* used in the aeronautic industry to manufacture blade integrated disk (Blisk) for aircraft engines. It is based on the reciprocal movement of the faces to be welded together accompanied with the application of an axial

pressure. The LFW process has three major phases [1-3]: at the beginning, the conditioning provides the thermal energy to soften the weld line. Then, the friction phase occurs when the oscillations expel the viscoplastic layer at the weld line; called flash. As a result of flash formation an axial shortening occurs. Once the target axial shortening is reached, the oscillations are stopped and the contact pressure can be increased to secure the bound until the latter cools down.

During the friction phase, the microstructure undergoes severe deformation at elevated temperature and high strain rate induced by shearing and compressive stresses [2]. This deformation impacts the joint mechanical properties such as tensile, creep and fatigue strength [2]. These properties depend directly on microstructural features such as phase proportions, precipitates, and grain size. Therefore, controlling and quantifying microstructural changes during different phases of LFW process would be a critical tool for the design of microstructure based LFW processes [4,5]. However, due to the highly dynamic nature of the process, experimental assessment of microstructure evolution as a function of LFW process parameters and particularly its evolution during each phase is a major challenge. Therefore, numerical simulation could be used as an efficient mean to study the microstructural changes occurring during each phase of the LFW process. Microstructure examinations have shown the occurrence of significant grain refinement, mainly due to DRX at the weld interface [4,5].

In this paper, the evolution of the dynamic recrystallization during the friction phase of the LFW of a Ti-6Al-4V alloy is simulated and analyzed using Transvalor FORGE NxT® 1.1 finite elements code. The numerical results of temperature evolution were compared to those obtained from literature. The results are also discussed and correlated with the extent of the DRXed zones, and DRX volume fraction.

2. Assumptions

The friction phase starts when the viscoplastic layer at the weld line can no longer sustain its normal stress and begins to flow, initiating the flash. At that point, full contact is established between the two welding surfaces thereby forming a single workpiece.

2.1 Material

A Ti-6Al-4V titanium alloy grade used for Blisk manufacturing was used for the study. In the simulation, the workpiece is considered homogeneous and isotropic. Temperature dependent physical (e.g. thermal conductivity, specific heat, thermal expansion, density) and mechanical properties (e.g. flow stress, Young's modulus, Poisson's ratio) were obtained from the Transvalor FORGE NxT® 1.1 database.

2.2 Initial Temperature Profile at the Start of the Friction Phase

The conditioning phase provides the thermal energy needed to soften the weld line and allows the joining of the two interfaces. As this phase is not simulated in this study, an initial temperature profile is required for the temperature at the end of the conditioning phase. In a recent publication the authors proposed a thermal model for analyzing the conditioning phase using ABAQUS 6.14 software, [6]. The methodology included a stop condition at 960°C to avoid any large deformation. If the simulation stop at 960°C at the center, then there is still mechanical strength to support the normal load at the edges as they are colder due to the oscillation. Consequently, the conditioning phase is not complete as all the weld line has not become viscoplastic. Therefore, this study has applied the stop condition at the edges of the weld line. In addition, as reported by Sorina-Müller, the Coulomb law used to model the friction during LFW is not reliable at high temperature [7,15]. Considering the limitations to simulate the conditioning phase, the methodology was adjusted to generate to impose the temperature distribution at the start of the friction phase.

2.3 Initial Microstructure at the Start of the Friction Phase

Experimental studies published in the literature on microstructure evolution during the LFW process have been based on comparing samples before and after welding where major microstructural changes have been observed [2,4,5]. However, very little or no data is available on the impact of deformation parameters (strain, strain rate, and temperature) on the microstructure [2]. In the present work, it is assumed that there is no dynamic recrystallization and hence, no grain refinement occurs during the conditioning phase. This assumption is based on the estimated temperature and strain rate during this phase: both parameters are too low to produce DRX [4]. Therefore, no DRXed grains are present at the start of the friction phase. Furthermore, based on the alpha-beta transition temperature, it is assumed that the weld line is only composed of β phase at the beginning of the friction phase [3].

3. Numerical Model

According to the literature [2], a single body approach is recommended in order to simulate the flash during the friction phase. Furthermore, this approach assumes that the two parts are already sticking together, requiring no friction model at the weld line. In this paper, the two workpieces are modeled by one billet of 26 mm width, 52 mm height, 1 mm thick. A 2D model was implemented in Transvalor FORGE® NxT 1.1 with a plain strain assumption. The oscillations are provided to the billet lower end by the lower dies. The upper end is guided by the upper dies, perpendicular to the oscillations. No friction is assumed between the upper dies and the billet in order to allow the axial shortening. The element size is 0.2 mm length at the weld line to account for the severe deformation occurring and coarsen further away to 1 mm length [2].

3.1 DRX Model

The microstructure examinations of linear friction welded samples have shown the occurrence of significant grain refinement, mainly due to DRX at the weld interface [4, 5]. This grain

refinement impacts significantly the joint mechanical properties [2]. Thus, it is crucial to predict the evolution of the microstructure during the LFW process, and especially dynamic recrystallization from a mechanical design point of view. Recrystallization kinetics being dependent on temperature and deformation, both of which are related to the LFW process parameters such as frequency, amplitude, and applied pressure [16]; therefore, the kinetics of dynamic recrystallization need to be determined. The application of the Johnson, Mehl, Avrami, Kolmogorov (JMAK) equation provides a first approximation of the evaluation of the recrystallization kinetics during LFW and the obtained results could be correlated with the grain size.

Many authors have used JMAK to model DRX during hot compression [8,9]. However, the strain and strain rates encountered during LFW [14] are expected to be much higher than those in hot compression and therefore it could be expected that kinetics of microstructure evolution would be different. However, considering the lack of numerical models on deformation parameters during LFW, using JMAK approach could be a starting step. The JMAK equation is defined as:

$$X_{\mathrm{drx}} = 1 - \exp\left(-\kappa\left(\frac{\overline{\varepsilon} - \varepsilon_c}{\varepsilon_{.5}}\right)^{\beta}\right) \tag{A III-1}$$

In the above equation with X_{drx} represents the recrystallized volume fraction, $\overline{\varepsilon}, \varepsilon_c, \varepsilon_{.5}$ respectively the equivalent, critical, and half-recrystallized strain, and κ and β dimensionless parameters. Due to the phenomenological nature of the JMAK equation, it is highly material dependent. Furthermore, the values of the variables depend on the testing temperature and strain rate ranges. In the present work, the data reported by Quan on hot compression of Ti-6Al-4V [10] were used in Equation A III-1. The latter can be further studied in terms of grain size [16] (not studied in this paper). A subroutine was developed to implement it in Transvalor FORGE NxT® 1.1 FEM code. This subroutine considers that if the recrystallized volume fraction reaches a threshold of 99%, then the material is considered as fully recrystallized and the X_{drx} is reset to 0, thereby creating a cycle. These cycles are then counted to quantify how

many times a region has undergone microscopic transformations. A new subroutine was added, called DRX cycles, to store the number of cycles.

4.   Results and discussion

4.1   Temperature history

The temperature near the weld line is the only recordable parameter if the thermocouple stays in place and is not crushed during the process [5,11]. Figure-A III-1 depicts the transition and equilibrium of the friction phase. The equilibrium phase is characterized by few variations of the temperature: between 1032°C and 1051°C. The transition phase shows an increase of temperature from 1019°C to the maximum working temperature of 1050°C. It is important to note that the model predicts small variations during the equilibrium phase as also reported by Vairis [1] and McAndrew et al. [11]. As mentioned above, the conditioning phase depends on the friction law used to characterize the interaction between the two parts. The discrepancy shown is due to the weakness of the Coulomb law to correctly model the friction during the conditioning phase. However, temperature slopes predicted using simulations and those recorded by thermocouples are very similar.
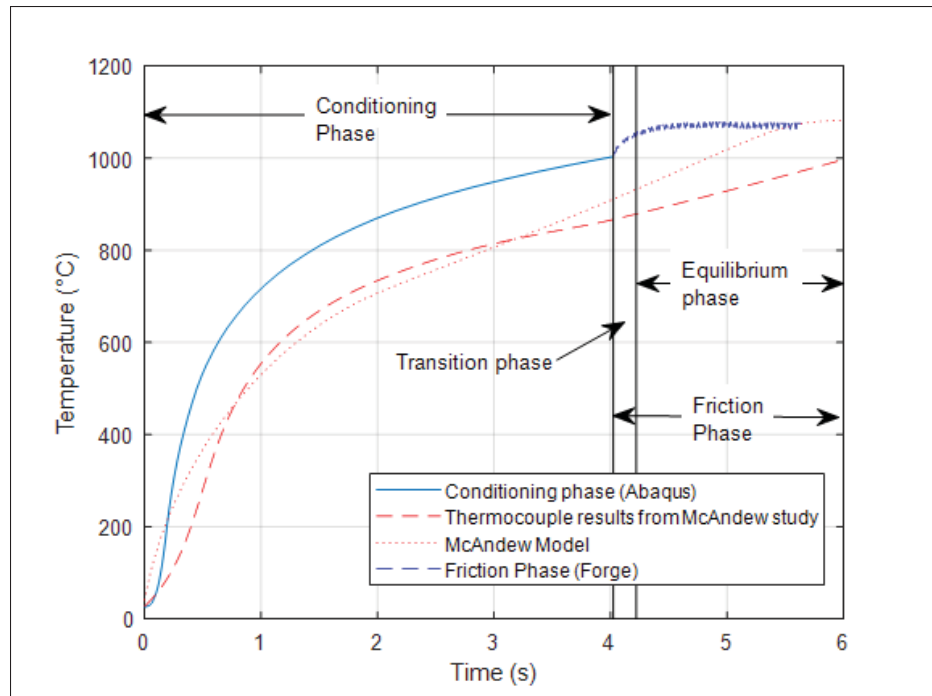
Figure-A III-1   Temperature history

4.2   DRX extent

The DRX cycles parameter introduced in this study measures mathematically how many times a region has been recrystallized according to the JMAK equation (Equation A III-1). At the end of the friction phase, as shown in Figure-A III-2, the most recrystallized regions are located at the junction of the flash and the billet. This is due to the high strain rate applied at the edge of the billet while the flash is being extruded [14]. As mentioned, the grain refinement observed in LFW is a part of the recrystallization process. These highly recrystallized regions match to the grain refinement regions seen in micrographs from the literature [4,5]. Furthermore, the width of the recrystallized region at the weld line center is coherent with the width of the grain refinement seen in the micrographs; around 0.5mm and 1 mm, depending on the process parameters [2,4,5]. However, the DRX cycles parameters quantifies only the number of successive transformations according to the JMAK equation (Equation A III-1) [16]. The recrystallization process enfolds various competitive processes such as nucleation, grain growth, mis-orientation. For instance, the weld line center undergoes 48 DRX cycles,

meaning there is a strong recrystallization resulting in significant grain refinement. However, it cannot be said that the grain size would continue to decrease indefinitely with the number of recrystallized cycles. It is reasonable to assume that the grains will recrystallize to a given point and then an equilibrium should be found between the grain size and the other microstructural processes. Secondly, it must be noted that, the DRX cycles parameter uses the JMAK law which as mentioned above is a phenomenological law used to study low strain and strain rate conditions compared to LFW Therefore, in order to further study microstructure evolution it would be necessary to implement mesoscale simulation using dislocation density theory to model dynamic recrystallization. To this end, various methodologies such as polycrystal model [13] or cellular automate [12] have been proposed. However, these methods must be adapted to the LFW process.
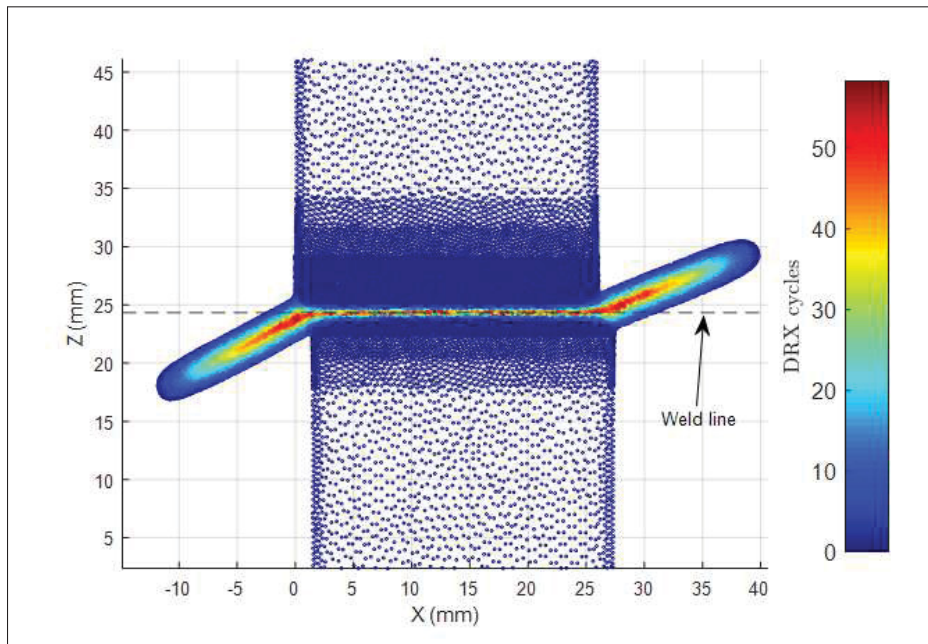

Figure-A III-2   Dynamic recrystallization extent

5. Conclusion

A model predicting microstructure evolution during the friction phase of the LFW process of a Ti-6Al-4V alloys is proposed. The model uses JMAK equation to predict the occurrence and the number of recrystallization cycles in each location of the joint and at the junction of the specimen and the flash. However, the JMAK model cannot be used to predict grain size as it is highly material and process variable dependent. Mesoscale models need to be used to quantify the microstructural changes as they occur during the process.

References

[1] A. Vairis and M. Frost, High frequency linear friction welding of a titanium alloy, *Wear*, 217 (1998) 117–131.

[2] A. R. McAndrew, P. A. Colegrove, C. Bühr, B. C. D. D. Flipo, and A. Vairis, A Literature Review of Ti-6Al-4V Linear Friction Welding, *Prog. Mater. Sci.*, 92 (2017) 225–257.

[3] M. Grujicic, G. Arakere, B. Pandurangan, C. F. Yen, and B. A. Cheeseman, Process modeling of Ti-6Al-4V linear friction welding (LFW), *J. Mater. Eng. Perform.*, 21, (2012) 2011–2023

[4] P. Wanjara and M. Jahazi, Linear Friction Welding of Ti-6Al-4V : Processing , Microstructure , and Mechanical-Property Inter-Relationships, *Metall. Mater. Trans. A Phys. Metall. Mater. Sci,* 36 (2005) 2149–2164

[5] E. C. Dalgaard, Evolution of Microstructure, Microtexture and Mechanical Properties in Linear Friction Welded Titanium Alloys, McGill University, 2011.

[6] S. Bertrand, D. Shahriari, M. Jahazi, and H. Champliaud, Linear friction welding process simulation of Ti-6Al-4V alloy : a heat transfer analysis of the conditioning phase, *Procedia Manuf.*, 15C (2018) 1382–1390.

[7] J. Sorina-Müller, M. Rettenmayr, D. Schneefeld, O. Roder, and W. Fried, FEM simulation of the linear friction welding of titanium alloys, *Comput. Mater. Sci.*, 48 (2010) 749–758

[8] S. Tamirisakandala, B. V. Vedam, and R. B. Bhat, Recent advances in the deformation processing of titanium alloys, *J. Mater. Eng. Perform.*, 12 (2003) 661–673.

[9] P. Honarmandi and M. Aghaie-Khafri, Hot Deformation Behavior of Ti-6Al-4V Alloy in beta Phase Field and Low Strain Rate, *Metallogr. Microstruct. Anal.*, 2 (2013) 13–20.

[10] G. Quan, G. Luo, J. Liang, D. Wu, A. Mao, and Q. Liu, Modelling for the dynamic recrystallization evolution of Ti-6Al-4V alloy in two-phase temperature range and a wide strain rate range, *Comput. Mater. Sci.*, 97 (2015) 136–147

[11] A. R. McAndrew, P. A. Colegrove, A. C. Addison, B. C. D. D. Flipo, and M. J. Russell, Modelling the influence of the process inputs on the removal of surface contaminants from Ti-6Al-4V linear friction welds, *Mater. Des.*, 66 (2015) 183–195

[12] J. W. Zhao, H. Ding, W. J. Zhao, F. R. Cao, H. L. Hou, and Z. Q. Li, Modeling of dynamic recrystallization of Ti6Al4V alloy using a cellular automaton approach, *Acta Metall. Sin.* 21 (2008) 260–268

[13] M. Anahid, M. K. Samal, and S. Ghosh, Dwell fatigue crack nucleation model based on crystal plasticity finite element simulations of polycrystalline titanium alloys, *J. Mech. Phys. Solids*, 59 (2011) 2157–2176

[14] A. R. McAndrew, P. A. Colegrove, A. C. Addison, B. C. D. Flipo, M. J. Russell, and L. A. Lee, Modelling of the workpiece geometry effects on Ti-6Al-4V linear friction welds, Mater. Des., 87 (2015) 1087–1099.

[15] M. Maalekian, E. Kozeschnik, H. P. P. Brantner, and H. Cerjak, Comparative analysis of heat generation in friction welding of steel bars, Acta Mater., 56 (2008) 2843–2855.

[16] F. Montheillet and J. J. Jonas, Models of Recrystallization, ASM Handb., 22 (2009) 220–231.

BIBLIOGRAPHY

Anahid, M., Samal, M. K. & Ghosh, S. (2011). Dwell fatigue crack nucleation model based on crystal plasticity finite element simulations of polycrystalline titanium alloys. *J. Mech. Phys. Solids*, 59(10), 2157–2176. doi: 10.1016/J.JMPS.2011.05.003.

Basak, D., Overfelt, R. A. & Wang, D. (2003). Measurement of specific heat capacity and electrical resistivity of industrial alloys using pulse heating techniques. *Int. J. Thermophys.*, 24(6), 1721–1733. doi: 10.1023/B:IJOT.0000004101.88449.86.

Bertrand, S., Shahriari, D., Jahazi, M. & Champliaud, H. (2018). Linear friction welding process simulation of Ti-6Al-4V alloy : a heat transfer analysis of the conditioning phase. *Procedia Manuf.*, 15C(September), 1382–1390.

Bhamji, I., Preuss, M., Threadgill, P. L. & Addison, A. C. (2011). Solid state joining of metals by linear friction welding: a literature review. *Mater. Sci. Technol.*, 27(1), 2–12. doi: 10.1179/026708310X520510.

Bikmeyev, A. T., Gazizov, R. K., Vairis, A. & Yamileva, A. M. (2013). MODELING THE TEMPERATURE DISTRIBUTION IN THE CONTACT AREA OF A MOVING OBJECT IN THE CASE OF LINEAR FRICTION WELDING. *ASME 2013 Int. Mech. Eng. Congr. Expo.*, 1–8.

Boivineau, M., Cagran, C., Doytier, D., Eyraud, V., Nadal, M., Wilthan, B. & Pottlacher, G. (2006). Thermophysical Properties of Solid and Liquid Ti-6Al-4V (TA6V) Alloy. *Int. J. Thermophys.*, 27(2), 507–529. doi: 10.1007/s10765-005-0001-6.

Buffa, G. & Fratini, L. (2017). Strategies for numerical simulation of linear friction welding of metals: a review. *Prod. Eng.*, 11(3), 1–15. doi: 10.1007/s11740-017-0726-7.

Bühr, C., Colegrove, P. A. & McAndrew, A. R. (2017). A computationally efficient thermal modelling approach of the linear friction welding process. *J. Mater. Process. Technol.*, 252, 849–858. doi: 10.1016/j.jmatprotec.2017.09.013.

Carslaw, H. S. & Jaeger, J. C. (1959). *Conduction of heat in solids*.

Ceretti, E., Fratini, L., Giardini, C., Spisa, D. L. & La Spisa, D. (2010). Numerical Modelling of the Linear Friction Welding Process. *Int J Mater Forum*, 3(S1), 1015–1018. doi: 10.1007/s12289-010-0942-6.

Dalgaard, E. C. (2011). *Evolution of Microstructure, Microtexture and Mechanical Properties in Linear Friction Welded Titanium Alloys*. (Ph.D. thesis, McGill University).

Ducato, A., Fratini, L., La Cascia, M. & Mazzola, G. (2013). Computer analysis of images and patterns. *J. Math. Imaging Vis.*, 47(1-2), 1–2. doi: 10.1007/s10851-013-0451-6.

Fratini, L. & La Spisa, D. (2011). Numerical simulation of linear fiction welding (LFW) processes. *AIP Conf. Proc.*, 1353, 1284–1289. doi: 10.1063/1.3589693.

Fratini, L., Buffa, G., Campanella, D. & La Spisa, D. (2012). Investigations on the linear friction welding process through numerical simulations and experiments. *Mater. Des.*, 40, 285–291. doi: 10.1016/j.matdes.2012.03.058.

Geng, P., Qin, G., Chen, L., Zhou, J. & Zou, Z. (2019a). Simulation of plastic flow driven by periodically alternating pressure and related deformation mechanism in linear friction welding. *Mater. Des.*, 178, 107863. doi: 10.1016/J.MATDES.2019.107863.

Geng, P., Qin, G., Zhou, J. & Zou, Z. (2019b). Finite element models of friction behaviour in linear friction welding of a Ni-based superalloy. *Int. J. Mech. Sci.*, 152, 420–431. doi: 10.1016/J.IJMECSCI.2019.01.014.

Grujicic, M., Arakere, G., Pandurangan, B., Yen, C. F. & Cheeseman, B. A. (2012). Process modeling of Ti-6Al-4V linear friction welding (LFW). *J. Mater. Eng. Perform.*, 21(10), 2011–2023. doi: 10.1007/s11665-011-0097-8.

Honarmandi, P. & Aghaie-Khafri, M. (2013). Hot Deformation Behavior of Ti-6Al-4V Alloy in beta Phase Field and Low Strain Rate. *Metallogr. Microstruct. Anal.*, 2(1), 13–20. doi: 10.1007/s13632-012-0052-6.

Hosford, W. F. & Caddell, R. M. (2007). *Metal forming: mechanics and metallurgy* (ed. 3). Cambridge University Press. Consulted at www.cambridge.org/9780521881210.

Jedrasiak, P., Shercliff, H. R., McAndrew, A. R. & Colegrove, P. A. (2018). Thermal modelling of linear friction welding. *Mater. Des.*, 156, 362–369. doi: 10.1016/j.matdes.2018.06.043.

Karadge, M., Preuss, M., Lovell, C., Withers, P. & Bray, S. (2007). Texture development in Ti–6Al–4V linear friction welds. *Mater. Sci. Eng. A*, 459(1-2), 182–191. doi: 10.1016/J.MSEA.2006.12.095.

Li, W.-Y., Ma, T., Yang, S., Xu, Q., Zhang, Y., Li, J. & Liao, H. (2008). Effect of friction time on flash shape and axial shortening of linear friction welded 45 steel. *Mater. Lett.*, 62(2), 293–296. doi: 10.1016/J.MATLET.2007.05.037.

Li, W.-Y., Ma, T. & Li, J. (2010). Numerical simulation of linear friction welding of titanium alloy: Effects of processing parameters. *Mater. Des.*, 31(3), 1497–1507. doi: 10.1016/j.matdes.2009.08.023.

Li, W., Wang, F., Shi, S. & Ma, T. (2014). Numerical simulation of linear friction welding based on ABAQUS environment: Challenges and perspectives. *J. Mater. Eng. Perform.*, 23(2), 384–390. doi: 10.1007/s11665-013-0776-8.

Maalekian, M., Kozeschnik, E., Brantner, H. P. & Cerjak, H. (2008). Comparative analysis of heat generation in friction welding of steel bars. *Acta Mater.*, 56(12), 2843–2855. doi: 10.1016/j.actamat.2008.02.016.

Maio, L., Franco, F., Squillace, A. & Lecce, L. (2016). A simplified approach to numerical simulation of LFW process of Ti6Al4V alloy: investigation on friction and temperature. *Int. J. Adv. Manuf. Technol.*, 86(9-12), 3217–3228. doi: 10.1007/s00170-016-8447-1.

McAndrew, A. R., Colegrove, P. A., Addison, A. C., Flipo, B. C. D. & Russell, M. J. (2014). Energy and Force Analysis of Ti-6Al-4V Linear Friction Welds for Computational Modeling Input and Validation Data. *Metall. Mater. Trans. A Phys. Metall. Mater. Sci.*, 45(13), 6118–6128. doi: 10.1007/s11661-014-2575-8.

McAndrew, A. R., Colegrove, P. A., Addison, A. C., Flipo, B. C., Russell, M. J. & Lee, L. A. (2015a). Modelling of the workpiece geometry effects on Ti-6Al-4V linear friction welds. *Mater. Des.*, 87, 1087–1099. doi: 10.1016/j.matdes.2015.09.080.

McAndrew, A. R., Colegrove, P. A., Addison, A. C., Flipo, B. C. D. & Russell, M. J. (2015b). Modelling the influence of the process inputs on the removal of surface contaminants from Ti-6Al-4V linear friction welds. *Mater. Des.*, 66(PA), 183–195. doi: 10.1016/j.matdes.2014.10.058.

McAndrew, A. R., Colegrove, P. A., Flipo, B. C. D. & Bühr, C. (2016). 3D modelling of Ti-6Al-4V linear friction welds. *Sci. Technol. Weld. Join.*, 1718(May), 1–9. doi: 10.1080/13621718.2016.1263439.

McAndrew, A. R., Colegrove, P. A., Bühr, C., Flipo, B. C. D. & Vairis, A. (2017). A Literature Review of Ti-6Al-4V Linear Friction Welding. *Prog. Mater. Sci.*, 92, 225–257. doi: 10.1016/j.pmatsci.2017.10.003.

Montheillet, F. & Jonas, J. J. (2009). Models of Recrystallization. *ASM Handb.*, 22(A), 220–231. doi: 10.31399/asm.hb.v22a.a0005403.

Potet, A., Mocellin, K. & Fourment, L. (2017). Numerical Simulation of Linear Friction Welding of Aeronautical alloys. *Esaform*, 110007, 4–9. doi: 10.1063/1.5008134.

Quan, G.-z., Luo, G.-c., Liang, J.-t., Wu, D.-s., Mao, A. & Liu, Q. (2015). Modelling for the dynamic recrystallization evolution of Ti-6Al-4V alloy in two-phase temperature range and a wide strain rate range. *Comput. Mater. Sci.*, 97, 136–147. doi: 10.1016/J.COMMATSCI.2014.10.009.

Schröder, F., Ward, R. M., Walpole, A. R., Turner, R. P., Attallah, M. M., Gebelin, J.-C. & Reed, R. C. (2015). Linear friction welding of Ti6Al4V: experiments and modelling. *Mater. Sci. Technol.*, 31(3), 372–384. doi: 10.1179/1743284714Y.0000000575.

Schroeder, F., Ward, R. M., Turner, R. P., Attallah, M. M., Gebelin, J. & Reed, R. C. (2012). Linear friction welding of titanium alloys for aeroengine applications: modelling and validation. *9th Int. Conf. Trends Weld. Res.*, (January), 886 – 892.

Sorina-Müller, J., Rettenmayr, M., Schneefeld, D., Roder, O. & Fried, W. (2010). FEM simulation of the linear friction welding of titanium alloys. *Comput. Mater. Sci.*, 48(4), 749–758. doi: 10.1016/j.commatsci.2010.03.026.

Tamirisakandala, S., Vedam, B. V. & Bhat, R. B. (2003). Recent advances in the deformation processing of titanium alloys. *J. Mater. Eng. Perform.*, 12(6), 661–673. doi: 10.1361/105994903322692466.

Transvalor. (2016). Reference Document - Part 8 - Metallurgy.

Turner, R., Gebelin, J. C., Ward, R. M. & Reed, R. C. (2011). Linear friction welding of Ti-6Al-4V: Modelling and validation. *Acta Mater.*, 59(10), 3792–3803. doi: 10.1016/j.actamat.2011.02.028.

Turner, R., Ward, R. M., March, R. & Reed, R. C. (2012). The Magnitude and Origin of Residual Stress in Ti-6Al-4V Linear Friction Welds: An Investigation by Validated Numerical Modeling. *Metall. Mater. Trans. B*, 43(1), 186–197. doi: 10.1007/s11663-011-9563-9.

Turner, R., Schroeder, F., Ward, R. M. & Brooks, J. W. (2014). The importance of materials data and modelling parameters in an FE simulation of linear friction welding. *Adv. Mater. Sci. Eng.*, 2014, 1–9. doi: 10.1155/2014/521937.

TWI, T. W. I. (2018). Linear Firction Welding. Accessed: 2018-04-18.

Vairis, A. & Frost, M. (1998). High frequency linear friction welding of a titanium alloy. *Wear*, 217(1), 117–131. doi: 10.1016/S0043-1648(98)00145-8.

Vairis, A. & Frost, M. (2000). Modelling the linear friction welding of titanium blocks. *Mater. Sci. Eng. A*, 292(1), 8–17. doi: 10.1016/S0921-5093(00)01036-4.

Vairis, A. & Christakis, N. (2007). The development of a continuum framework for friction welding processes with the aid of micro-mechanical parameterisations. *Int. J. Model. Identif. Control*, 2(4), 347. doi: 10.1504/ijmic.2007.016417.

Wanjara, P. & Jahazi, M. (2005). Linear Friction Welding of Ti-6Al-4V : Processing , Microstructure , and Mechanical-Property Inter-Relationships. *Metall. Mater. Trans. A Phys. Metall. Mater. Sci.*, 36(August), 2149–2164. doi: 10.1007/s11661-005-0335-5.

Yang, X., Li, W., Li, J., Xiao, B., Ma, T., Huang, Z. & Guo, J. (2015). Finite element modeling of the linear friction welding of GH4169 superalloy. *Mater. Des.*, 87, 215–230. doi: 10.1016/j.matdes.2015.08.036.

Zhao, J., Ding, H., Zhao, W., Cao, F., Hou, H. & Li, Z. (2008). Modeling of dynamic recrystallization of Ti6Al4V alloy using a cellular automaton approach. *Acta Metall. Sin. (English Lett.*, 21(4), 260–268. doi: 10.1016/S1006-7191(08)60047-2.

Zhao, P., Fu, L. & Zhong, D. (2014). Numerical simulation of transient temperature and axial deformation during linear friction welding between TC11 and TC17 titanium alloys. *Comput. Mater. Sci.*, 92, 325–333. doi: 10.1016/j.commatsci.2014.05.062.